EXPERIMENTAL INVESTIGATIONS OF OPTICAL PROPAGATION IN ATMOSPHERIC TURBULENCE

by Michael W. Fitzmaurice

Goddard Space Flight Center
Greenbelt, Md. 20771

NATIONAL AERONAUTICS AND SPACE ADMINISTRATION • WASHINGTON, D. C. • AUGUST 1971

1. Report No.	2. Government Accession No.	3. Recipient's Catalog No.
NASA TR R-370		

4. Title and Subtitle	5. Report Date
Experimental Investigations of Optical Propagation In Atmospheric Turbulence	August 1971
	6. Performing Organization Code

7. Author(s)	8. Performing Organization Report No.
Michael W. Fitzmaurice	G-1004

9. Performing Organization Name and Address	10. Work Unit No.
Goddard Space Flight Center Greenbelt, Maryland 20771	11. Contract or Grant No.
	13. Type of Report and Period Covered
12. Sponsoring Agency Name and Address	Technical Report
National Aeronautics and Space Administration Washington, D.C. 20546	14. Sponsoring Agency Code

15. Supplementary Notes
Dissertation submitted to the faculty of the graduate school of the University of Maryland in partial fulfillment of the requirements for the degree of Doctor of Philosophy, 1970.

16. Abstract
The pertinent theoretical background and the results of a group of experiments conducted over 0.4- and 1.17-km near-ground horizontal ranges are presented. (1) The log-amplitude variances for HeNe (0.633 μm) and CO_2 (10.6 μm) laser beams were found to have a ratio of 26.8, which is in close agreement with the predictions of Rytov-based spherical-wave theory. (2) Published measurements of the saturation level of the log-amplitude variance are reviewed and several inconsistencies noted. (3) The spatial correlation function of the irradiance field was measured and found to agree with theory. The degree of correlation between different frequency beams which had traversed the same optical path was also measured and compared to theory. The data exhibited an unacceptably large scatter and did not show the wavelength dependence. (4) The log-normal, Rayleigh, and Rice probability distributions are discussed in terms of their applicability to irradiance statistics. Relatively weak 10.6 μm irradiance fluctuations were found to be equally well described by the log-normal and Rice distributions; strong fluctuations obtained at 0.488 μm were clearly best described by the log-normal distribution.

17. Key Words Suggested by Author	18. Distribution Statement
Optical Propagation Turbulence Effects	Unclassified-Unlimited

19. Security Classif. (of this report)	20. Security Classif. (of this page)	21. No. of Pages	22. Price
Unclassified	Unclassified	183	$3.00

*For sale by the National Technical Information Service, Springfield, Virginia 22151

CONTENTS

EXPERIMENTAL INVESTIGATIONS OF OPTICAL PROPAGATION IN ATMOSPHERIC TURBULENCE*

by

Michael Williams Fitzmaurice

Goddard Space Flight Center

INTRODUCTION

The study of optical propagation in random media has been renewed with increased vigor in the past two decades. The works of Chernov[1] and Tatarski[2] in the Soviet Union during the 1950's rekindled interest and advanced the state of knowledge so that many previously unsolved problems became rigorously amenable. It appears that these efforts were motivated primarily by a desire to fill theoretical voids in the classical treatment of certain problems in electromagnetic theory and acoustics. Following the initial realizations of the laser, however, these studies gained an increased utility. It became immediately apparent that attainment of the exciting goals forecast for the laser would require that it retain it's spatial coherence, temporal coherence, and high energy density over the propagation path. Clearly, transmission through the earth's atmosphere would introduce a randomness to each of these factors and thereby impose certain limits on performance capabilities. During the same time-period, increased emphasis on aerial photography from aircraft as well as satellite platforms

*Dissertation submitted to the faculty of the graduate school of the University of Maryland in partial fulfillment of the requirements for the degree of Doctor of Philosophy, 1970.

generated a need for an understanding of resolution limitations imposed by a turbulent atmosphere. In addition, the field of optical astronomy has traditionally been hampered by the earth's atmosphere; thus, considerable effort has been expended to understand the causes and effects of the turbulent atmosphere upon earth-based measurements.[3-6] For all these reasons, the monographs of Chernov and Tatarski aroused considerable interest and have served as a starting point for much theoretical and experimental work on the optical propagation problem in the decade of the 1960's. In this dissertation we shall —

(1) Review the causal mechanism for the optical propagation problem (i.e., the random refractive index field).

(2) Summarize the more important theoretical and experimental results now available.

(3) Present the results of a group of new experiments which, it is hoped, will clarify certain aspects of the propagation problem.

The material is organized such that Chapter 1 deals with items 1 and 2, and Chapter 2 presents the new experimental work, item 3.

CHAPTER I

THEORETICAL CONSIDERATIONS

I.1 Optical Propagation Through Turbulence: Problem Definition

In general, a propagating electromagnetic wave can be perturbed by many different mechanisms. Different types of perturbation are treated analytically by very distinct techniques which are sometimes exact but often approximate. We now review four types of propagation problems so as to define precisely the problem with which we are concerned in this paper.

The first type is the free space propagation problem. Here a wave is launched into an evacuated medium and progresses in accordance with the classical wave results obtainable from Maxwell's equations. In regions near obstacles, diffraction theory with suitable boundary conditions is employed. Usually, Kirchhoff diffraction theory[7,8] is employed, although it is well known that it is an approximate technique and, in fact, has some internal contradictions.[9,10] Other approaches such as the Rayleigh-Summerfeld theory[9,11,12] are available and are sometimes employed.

In the second type of problem we consider a material medium which is characterized by constant properties. That is, the medium has a constant composition, temperature, pressure, and permittivity. No particles with sizes greater than the molecular scale are present. In this case, one finds that the molecular

matter is excited into oscillation by the incident wave and behaves as a collection of classical Hertzian dipoles with radiated fields which are calculable from well-known formulas.[13,14] This type of scattering was initially treated by Lord Rayleigh[15,16] and is widely known as Rayleigh scattering.

In the third type of problem, we consider a medium where the dominant perturbations to a propagating wave are caused by particulate matter with scale sizes which are equal to or greater than the wavelength of the incident radiation. A problem of this type has been solved by Mie[17] for the case of a plane wave incident on a spherical particle of arbitrary size and permittivity. The scattered energy is expressed in terms of an infinite series of terms representing products of associated Legendre polynomials and spherical Bessel functions.[18] Exact series and useful and approximate solutions are available.[19] In practice the usefulness of either result is limited by the knowledge available on particle size distribution, density, and composition throughout the propagation medium. A great deal of information is available in these areas for particular cases.[20-23]

A fourth type of propagation problem is the subject of this thesis. Here the medium is devoid of particulate matter and is characterized by zero conductivity and certain other average properties (composition, temperature, pressure, permittivity, etc.) which may be slowly varying functions of position. We also allow the point-by-point values of the medium properties to exhibit small deviations from the average.

Physically, this propagation problem may be interpreted as follows: when a wave (e.g., plane wave) is launched into the turbulent medium, the small deviations in medium properties which result in correspondingly small refractive index

fluctuations cause the wavefront to quickly become non-planar. For relatively short distances into the medium, the amplitude along constant phase surfaces remains essentially constant, although the wavefront distortion grows progressively larger. It should be clear that, for long enough propagation paths, the warping of the equi-phase surfaces will result in a shaping of the amplitude distribution across the wave. So, in general, one must solve for the complex-valued field quantity u which satisfies the linear stochastic differential equation*

$$\nabla^2 u + k^2 n^2 u = 0, \tag{1}$$

where the wave number $k = 2\pi/\lambda = \omega/c$ and n is the refractive index.

The field u depends on position and time, i.e., $n = n(\bar{r}, t)$. However, we account for the time dependence of n by letting each $n(\bar{r}, t_i)$, for $i = 1, 2, \ldots$, be considered a particular realization of the stochastic process $\{n(\bar{r})\}$. This assumption is clearly valid, since the time constant associated with changing spatial distributions of n ($\approx 10^{-3}$ seconds) is much greater than typical wave transit times through the turbulence and the wave period.[24-26]

In principle, one could solve the problem (Eq. 1) for each realization $n_i(\bar{r})$, catalogue the results, and by monitoring the behavior of $n(\bar{r})$ over the propagation path extract the precise time behavior of the field u. This, of course, is not practical, since the number of realizations is infinite [$n(\bar{r}_i, t)$ is continuous] and the instrumentation required for obtaining instantaneous values of n over the entire path is never available. Instead, we approach the

*The justification for using this equation as the starting point is given in Section 1.3.

problem from a statistical standpoint and attempt to evaluate certain statistics of u (mean, variance, etc.) in terms of the statistics of the refractive index field $n(\bar{r})$ over the propagation path. Clearly then, we must inspect the index of refraction fluctuations which occur in the atmosphere, their parameter dependence, and their statistical form. This is carried out in the next section.

1.2 Refractive Index Statistics in the Turbulent Atmosphere

The index of refraction of air is expressible in terms of the properties of the air through the relations[27]

$$n = 1.0 + \frac{77.6\,P}{T}\left(1 + \frac{0.0075}{\lambda^2}\right)10^{-6}, \qquad \text{at optical frequencies,} \quad (2)$$

and

$$n = 1.0 + \frac{77.6\,P}{T} \times 10^{-6} + \frac{3.8}{T^2}\,(1 - 0.0195\,z)^6, \quad \text{at radio frequencies,} \quad (3)$$

where P is atmospheric pressure in millibars, T is absolute temperature in Kelvin degrees, λ is wavelength in microns, z is altitude above sea level in thousands of feet, and a standard atmosphere[28] is assumed. We restrict our attention to the optical case, Eq. 2. In turbulent flow, the pressure fluctuations have been shown to be negligible* and it can therefore immediately be concluded that deviations in the optical index are caused by microthermal fluctuations. Our goal, then, is to determine the statistical nature of the thermal fluctuations.

*This point is discussed in detail in Ref. 24, pp. 208-210.

The approach used by Tatarski (which he states was initially formulated by Obukhov[29] and Kolmogorov[30]) first investigates the velocity fluctuations in a highly developed turbulent flow. Highly developed turbulent flow means simply that the Reynolds number which characterizes the flow is much greater than the Reynolds number at which the transition from laminar to turbulent flow takes place. The results are most conveniently expressed in terms of the structure function $D_{ik}(\bar{r})$ of the velocity field defined as

$$D_{ik}(\bar{r}) = \overline{(V_i - V_i')(V_k - V_k')}, \text{ for } i, k = 1, 2, 3, \tag{4}$$

where the V_i are the components of the velocity vector in the x, y, z directions at the point $\bar{r}_1$, and the V_i' are the same quantities at the point $\bar{r}_1 + \bar{r}$. So, in general, $D_{ik}(\bar{r})$ is a set of nine functions which describes the intensity of the velocity fluctuations of spatial extent r or less. Assuming local isotropy, express $D_{ik}(\bar{r})$ as a linear combination of $D_{rr}(r)$ and $D_{tt}(r)$, where

$$D_{rr}(r) = \overline{(V_r - V_r')^2}$$

and

$$D_{tt}(r) = \overline{(V_t - V_t')^2},$$

and where V_r is the component of the velocity field at $\bar{r}_1$ in the direction $\bar{r}$, and V_r' is the same quantity at the other measurement point $\bar{r}_1 + \bar{r}$. Similarly V_t is the component of the velocity vector at $\bar{r}_1$ in a direction perpendicular to $\bar{r}$, and V_t' is the corresponding quantity at the point $\bar{r}_1 + \bar{r}$. Assuming incompressible flow, Tatarski shows through dimensional analysis that both $D_{rr}(r)$ and $D_{tt}(r)$ grow as $r^{2/3}$ for spacings r much greater than the inner scale of turbulence and much less than the outer scale.

We carry out the analysis of temperature fluctuations by considering temperature to be a conservative passive additive to the highly developed turbulent flow. The problem of determining the statistics of the resulting microthermal field was solved by Obukhov[31] and Yaglom[32] and yielded results for the structure function of the temperature field:

$$D_T(r) = a^2 \frac{\bar{N}}{\epsilon^{1/3}} r^{2/3}, \text{ for } \ell_o << r << L_o,$$

and

$$D_T(r) = \frac{1}{3} \frac{\bar{N}}{D} r^2, \text{ for } r << \ell_o, \tag{5}$$

where a is a numerical constant, $\bar{N}$ is the dissipation rate of temperature fluctuations due to molecular diffusion, ϵ is the corresponding dissipation rate caused by fluid viscosity, and D is the molecular diffusion coefficient. As before, the "2/3 law" is seen to hold for separations between the inner (ℓ_o) and outer (L_o) scales. The spatial range defined by ℓ_o and L_o is called the inertial subrange and is considered to denote the limits over which temperature (and, therefore, refractive index) fluctuations may be considered isotropic. Proportionality constants are usually defined over the inertial subrange as follows:

$$D_T(r) = \overline{\left[T(\bar{r}_1) - T(\bar{r}_1 + \bar{r})\right]^2} = C_T^2 r^{2/3}$$

and

$$D_n(r) = \overline{\left[n(\bar{r}_1) - n(\bar{r}_1 + \bar{r})\right]^2} = C_n^2 r^{2/3}, \tag{6}$$

where C_T^2 is called the temperature structure constant and C_n^2 is called the refractive index structure constant. The notational change from $D(\bar{r})$ to $D(r)$ results

from the assumption of isotropy. In general, at visible wavelengths and moderate average temperatures,

$$C_n^2 \approx 10^{-12} C_T^2 .$$

There are several points worthy of discussion as regards the Obukhov - Kolmogorov turbulence model. First, and perhaps most important, there is considerable experimental evidence both in the Soviet Union[33,34] and the United States,[35,36] that the model closely agrees with observations in most cases. Because of the model itself having a firm basis in statistical turbulence theory, it would seem to be very risky to use any significantly different model in propagation calculations if agreement between theory and experiment is to be expected.

It must be noted, however, that this model says little about the form of $D_n(r)$ for r values near the inner and outer scales. In many problems, the exact behavior of $D_n(r)$ near $r = L_o$ does not appear to be very important.[37,38] However, the form of $D_n(r)$ near $r = \ell_o$ may be quite significant[39] and could appreciably effect some calculations. Also, the mathematical form of the Obukhov - Kolmogorov model appreciably complicates calculations, and solutions are obtainable only through computer-processed numerical integrations.[40]

In an attempt to avoid or alleviate certain of these problems, various theoreticians[1,41] have employed a gaussian model for the covariance function of the index of refraction. For example, Beckmann[42] used the following covariance

model:

$$C(r) = \overline{\mu^2} \exp\left[-\left(\frac{x}{X}\right)^2 - \left(\frac{y}{Y}\right)^2 - \left(\frac{z}{Z}\right)^2\right], \tag{7}$$

where $\overline{\mu^2}$ is the variance of refractive index field; x, y, and z are the rectangular components of r; and X, Y, and Z are the correlation distances in the respective directions. Clearly, such a model eases the mathematical complexity in making calculations and, in addition, has the decided advantage of permitting anisotropy in the refractive index field. However, the model has no basis in turbulence theory and has only one scale length per direction. In this sense, the gaussian model is far less acceptable than the Kolmogorov model.

In conclusion, it seems that if one desires to make meaningful comparisons between experiment and theory, the observations must be compared with theoretical results calculated through "2/3 law" turbulence models. Any agreement of experiment with gaussian-based theory can probably be regarded as fortuitous. In the remainder of this paper, we emphasize only those results from propagation theory which are based on the Obukhov-Kolmogorov Turbulence Theory.

1.3 Theoretical Approaches to the Optical Propagation Problem

Solutions to the general problem of propagation through random media have been sought by many theoreticians using very different approaches. We make no attempt to review all existent techniques, but rather restrict ourselves to those which are most widely used. Each will be reviewed from first principles

and its limitations noted. Specifically, we concern ourselves with Geometrical Optics, Born Theory, and Rytov Theory.

A common starting point exists for each technique. We consider a non-conducting medium without sources which is characterized by a position-dependent scalar permittivity, $\epsilon = \epsilon(x, y, z)$, and a constant scalar permeability, $\mu = \mu_0$. Then Maxwell's equations can be written in MKS units as

$$\text{a.}\quad \nabla \cdot \bar{D} = 0, \qquad \text{c.}\quad \nabla \cdot \bar{B} = 0,$$

$$\text{b.}\quad \nabla \times \bar{E} = -\frac{\partial \bar{B}}{\partial t}, \qquad \text{d.}\quad \nabla \times \bar{H} = \frac{\partial \bar{D}}{\partial t}, \tag{8}$$

with the constitutive relations

$$\text{e.}\quad \bar{D} = \epsilon \bar{E}$$

$$\text{f.}\quad \bar{B} = \mu \bar{H} .$$

Using the vector identity $\nabla \times \nabla \times \bar{A} = \nabla(\nabla \cdot \bar{A}) - \nabla^2 \bar{A}$ and taking the curl of Eq. 8b, we obtain

$$\nabla(\nabla \cdot \bar{E}) - \nabla^2 \bar{E} = -\mu \nabla \times \left(\frac{\partial \bar{H}}{\partial t}\right). \tag{9}$$

Assuming harmonic time-dependence $\left(e^{-j\omega t}\right)$ for all field quantities, and putting 8d into the right-hand side of Eq. 9, we get

$$\nabla(\nabla \cdot \bar{E}) - \nabla^2 \bar{E} = j\omega\mu(-j\omega\epsilon\bar{E}) = \omega^2 \mu\epsilon \bar{E} . \tag{10}$$

Using the identity $\nabla \cdot (V\bar{A}) = V\nabla \cdot \bar{A} + \bar{A} \cdot \nabla V$ applied to Eq. 8a, we get

$$\nabla \cdot \epsilon\bar{E} = \epsilon\nabla \cdot \bar{E} + \bar{E} \cdot \nabla\epsilon \ .$$

Thus,

$$\nabla \cdot \bar{E} = \frac{\nabla \cdot \epsilon\bar{E} - \bar{E} \cdot \nabla\epsilon}{\epsilon} \ . \tag{11}$$

Substituting into Eq. 10, we write

$$\nabla^2 \bar{E} + \omega^2 \mu\epsilon\bar{E} = -\nabla\left(\frac{\bar{E} \cdot \nabla\epsilon}{\epsilon}\right) \ . \tag{12}$$

The index of refraction n for a medium is defined in terms of a phase velocity ratio as

$$n = \frac{c}{V} = \sqrt{\frac{\mu\epsilon}{\mu_0 \epsilon_0}} = \sqrt{\frac{\epsilon}{\epsilon_0}} \ ,$$

where μ_0, ϵ_0, and c are the free space values and we assume $\mu = \mu_0$. Setting the permeability equal to unity and introducing the free space wave number

$$k = \frac{\omega}{c} = \frac{2\pi}{\lambda} \ ,$$

we can write Eq. 12 as

$$\nabla^2 \bar{E} + k^2 n^2 \bar{E} = -2\nabla(\bar{E} \cdot \nabla \ln n) \ . \tag{13}$$

This is the general equation which must be solved for propagation in a medium characterized by a random-point function for the refractive index. Eq. 13 is a vector equation and hence is really three scalar equations. Consider the x component and expand the right-hand side. Then,

$$\nabla^2 E_x + k^2 n^2 E_x = E_x \frac{\partial^2}{\partial x^2} ln\, n + \frac{\partial E_x}{\partial x} \frac{\partial\, ln\, n}{\partial x} + E_y \frac{\partial^2}{\partial x \partial y} ln\, n$$

$$+ \frac{\partial E_y}{\partial x} \frac{\partial}{\partial y} ln\, n + E_z \frac{\partial^2}{\partial x \partial y} ln\, n + \frac{\partial E_z}{\partial x} \frac{\partial\, ln\, n}{\partial z} . \quad (14)$$

Clearly the term $\nabla(\bar{E} \cdot \nabla\, ln\, n)$ in Eq. 13 couples the various components of the field together and is responsible for polarization fluctuations. Usually this term is dropped, and polarization fluctuations are considered negligible on the basis of the following argument.[43] Since the deviations of n from its mean value are very small(typically, $n/\langle n \rangle \sim 10^{-6}$), then one can assume that the deviation of $\bar{E}$ from the value $\bar{E}_0$ it would assume in a turbulence-free region is also small. In this case, a perturbation-type solution can be sought for $\bar{E}$, i.e.,

$$\bar{E} = \bar{E}_0 + \bar{E}_1 ,$$

with (15)

$$n = \langle n \rangle + n_1 .$$

Substituting Eq. 15 into Eq. 13, expanding, simplifying, and dropping all terms greater than first order, we find that

$$\nabla^2 \bar{E}_1 + k^2 \bar{E}_1 + 2k^2 n_1 \bar{E}_0 + 2\nabla(\bar{E}_0 \cdot \nabla n_1) = 0 . \quad (16)$$

Comparing the third and fourth terms in Eq. 16, we find that the third divided by the fourth is approximately equal to ℓ_o/λ. Since the assumption $\ell_o \gg \lambda$ appears reasonable for all optical problems, the fourth term in Eq. 16 can be dropped. Since this term was generated by the right-hand side of Eq. 13, then $\nabla(\bar{E} \cdot \nabla \ln n)$ in Eq. 13 can be neglected. We conclude that the equation to be solved is

$$\nabla^2 \bar{E} + k^2 n^2 \bar{E} = 0 . \tag{17}$$

The solution of this equation using the three previously listed techniques is the subject of the following sections.

a. Geometrical Optics. We first note that Eq. 17 is equivalent to three identical scalar equations, and so we need only deal with

$$\nabla^2 E + k^2 n^2 E = 0 , \tag{18}$$

where E is any of the rectangular components of $\bar{E}$. Eq. 18 can be rewritten in the form[7]

$$\nabla^2 E + k^2 n^2 E = \frac{\nabla^2 E}{E} + k^2 n^2 = \nabla^2 \ln E + |\nabla \ln E|^2 + k^2 n^2 = 0, \tag{18A}$$

where the various forms are easily equated by direct expansion. Let

$$E(\bar{r}) = A(\bar{r}) \exp\left[i\, S(\bar{r})\right] .$$

Then we have

$$\nabla^2 \{\ln A + iS\} + |\nabla(\ln A + iS)|^2 + k^2 n^2 = 0 .$$

Separate the above equation into real and imaginary parts and equate both to zero. For the real part,

$$\nabla^2 \ln A + |\nabla \ln A|^2 - |\nabla S|^2 + k^2 n^2 = 0 .$$

For the imaginary part,

$$\nabla^2 S + 2\nabla \ln A \cdot \nabla S = 0 . \tag{19}$$

Noting the relationships used above, we can write

$$|\nabla S|^2 = k^2 n^2 + \frac{\nabla^2 A}{A} , \tag{20}$$

but, since the wave amplitude can be expected to change in space no faster than $1/\ell_o$, then

$$\frac{\nabla^2 A}{A} \sim \frac{1}{\ell_o^2} << k^2 n^2 \sim k^2 .$$

Therefore, Eq. 20 becomes

$$|\nabla S|^2 = k^2 n^2 , \tag{21}$$

which is the Eiconal equation. Eqs. 19 and Eq. 21 are the basis for the geometrical optics approach. The primary limitation of the approach is that amplitude changes near boundaries are not properly treated.[44] The neglect of the $\nabla^2 A/A$ term is tantamount to ignoring diffraction effects. The amplitude fluctuations which are predicted by geometrical optics for the turbulent wave propagation

problem are not in any sense due to diffraction effects but rather are caused by the lens effect of inhomogeneities along the path. That is, as one moves along the propagation path, the phase field has some curvature associated with it at every point. The integral of this curvature along the path results in a focusing or de-focusing of the on-axis ray bundle, and hence the on-axis energy density either increases or decreases. The predictions for phase fluctuations obtained through geometrical optics are in general considered to have a wider range of validity than those for amplitude statistics.[45] This aspect will be considered in more detail in later sections.

b. Born Theory. As before, we begin with the scalar version of Eq. 17, i.e.,

$$\nabla^2 E + k^2 n^2 E = 0 .$$

Since the refractive index deviations are assumed small (compared to the mean value), a perturbation-type solution of the form

$$E = E_0 + E_1$$

is sought, where E_0 is the field that would exist in the absence of turbulence. We let $n(\bar{r}) = 1 + n_1(\bar{r})$ and note that $\nabla^2 E_0 + k^2 E_0 = 0$. Eq. 18 can now be written as

$$\nabla^2 E_1 + 2k^2 n_1 E_0 + k^2 n_1^2 E_0 + k^2 E_1 + 2n_1 k^2 E_1 + k^2 n_1^2 E_1 = 0 .$$

Since $n_1 << 1$ and E_1 is of the order $n_1 |E_0|$, we can neglect higher-order terms with small error and write

$$\nabla^2 E_1 + k^2 E_1 = - 2k^2 n_1 E_0 .$$

This equation has the solution

$$E_1(\bar{r}) = \int_V 2k^2 n_1(\bar{r}') E_0(\bar{r}') G\left(|\bar{r} - \bar{r}'|\right) dv', \tag{22}$$

where $G\left(|\bar{r} - \bar{r}'|\right)$ is the free space Green's function defined as

$$G\left(|\bar{r} - \bar{r}'|\right) = \frac{1}{4\pi} \frac{\exp\left[ik|\bar{r} - \bar{r}'|\right]}{|\bar{r} - \bar{r}'|}$$

and the integral is over the scattering volume V. Eq. 22 is the basic result of single-scatter Born theory. Its usefulness is seriously compromised by the restriction that $|E_1| / |E_0| \ll 1$.* In fact, it is well known that at visible wavelengths this condition is violated for relatively short ranges through mild turbulence.[46]

A multiple scattering approach can be formulated from this theory by a series expansions of E in the form

$$E = E_0 + E_1 + E_2 + \cdots E_j, \tag{23}$$

where $|E_i| \sim n_1 |E_{i-1}|$. Substitute Eq. 23 into Eq. 18 with $n = 1 + n_1$, expand, and group terms of equal order of smallness. Then we obtain the systems of

* For phase calculations using Born theory it is required that $k^2 \langle n_1^2 \rangle \ell L \ll 1$, where ℓ is a characteristic scale for the turbulence and L is the path length.

equations

$$
\begin{aligned}
\left(\nabla^2 + k^2\right) E_0 &= 0 , \\
\left(\nabla^2 + k^2\right) E_1 &= -\, 2k^2 n_1 E_0 , \\
&\vdots \\
\left(\nabla^2 + k^2\right) E_j &= -\, 2k^2 n_1 E_{j-1} - k^2 n_1^2 E_{j-2} , \quad \text{for} \quad j \geq 2 .
\end{aligned}
\tag{24}
$$

This set of equations has the solution

$$
E_i(\bar{r}) = \int_V \left\{ k^2 n_1^2 + 2k^2 n_1 \frac{E_{i-1}(\bar{r}')}{E_{i-2}(\bar{r}')} \right\} E_{i-2}(\bar{r}')\, G\left(|\bar{r} - \bar{r}'|\right) dv' , \quad \text{for } i \geq 2 .
\tag{25}
$$

We now have a set of integral equations to solve, starting with $i = 1$. Clearly, the range of validity of the technique has been extended, but the mathematical complexity is increased so much that the possibility of making meaningful calculations is doubtful. The accuracy of the technique versus the number of terms in the series does not seem to be well established at this time.

c. Rytov Theory. This approach has been given wide exposure through the work of Chernov and Tatarski and continues to be the subject of much discussion. The derivation starts with the transformed version of Eq. 18, i.e.,

$$
\nabla^2 \ln E + |\nabla \ln E|^2 + k^2 n^2 = 0 .
\tag{18A}
$$

Let

$$
E(\bar{r}) = A(\bar{r}) \exp\left[i\, S(\bar{r})\right]
$$

and

$$
n(\bar{r}) = 1 + n_1(\bar{r}) ,
$$

and define the complex phase ψ as

$$E(\bar{r}) = \exp\left[\psi(\bar{r})\right] = \exp\left[ln\, A(\bar{r}) + i\, S(\bar{r})\right] .$$

Therefore,

$$ln\, E(\bar{r}) = ln\, A(\bar{r}) + i\, S(\bar{r}) = \psi(\bar{r}) . \tag{26}$$

Substituting this result into Eq. 18A, we can write

$$\nabla^2 \psi + |\nabla\psi|^2 + k^2 \left(1 + n_1\right)^2 = 0 . \tag{27}$$

We set

$$\psi = \psi_0 + \psi_1 .$$

Therefore,

$$E = \exp\left[\psi_0 + \psi_1\right] = E_0 \exp\left[\psi_1\right], \tag{28}$$

where E_0 is the unscattered wave which satisfies

$$\nabla^2 E_0 + k^2 E_0 = 0,$$

or

$$\nabla^2 ln\, E_0 + |\nabla\, ln\, E_0|^2 + k^2 = 0 .$$

This last equation can be written as

$$\nabla^2 \psi_0 + |\nabla \psi_0|^2 + k^2 = 0 . \tag{29}$$

Substituting the first of Eqs. 28 into Eq. 27 and subtracting Eq. 29 from the result, we obtain

$$\nabla^2 \psi_1 + |\nabla \psi_1|^2 + 2\nabla \psi_0 \cdot \nabla \psi_1 + k^2 \left(2n_1 + n_1^2\right) = 0, \tag{30}$$

which is the nonlinear Ricatti equation. Since $n_1 \ll 1$, $k^2 n_1^2$ is much less than $2k^2 n_1$ and can be dropped. Similarly, since $|\nabla \psi_1| \ll |\nabla \psi_0| \sim k$, then $|\nabla \psi_1|^2 \ll 2\nabla \psi_0 \cdot \nabla \psi_1$ and we also neglect the $|\nabla \psi_1|^2$ term. Therefore, Eq. 30 can be written

$$\nabla^2 \psi_1 + 2\nabla \psi_0 \cdot \nabla \psi_1 + 2k^2 n_1 = 0 . \tag{31}$$

Eq. 31 is the linearized form of Eq. 30 and is the fundamental equation of Rytov theory. The dropping of the term $|\nabla \psi_1|^2$ in Eq. 30 is called the "Rytov Approximation." We now define W in terms of complex phase quantities as

$$W = \psi_1 e^{\psi_0} . \tag{32}$$

Substituting for ψ_1 in Eq. 31 using Eq. 32 and after expanding and simplifying, we have

$$\nabla^2 W + k^2 W = - 2k^2 n_1 E_0 , \tag{33}$$

which has the solution

$$W(\bar{r}) = \int_V 2k^2 n_1(\bar{r}') E_0(\bar{r}') G(|\bar{r} - \bar{r}'|)\, dv', \tag{34}$$

and therefore,

$$\psi_1(\bar{r}) = \frac{1}{E_0(\bar{r})} \int_V 2k^2 n_1(\bar{r}') E_0(\bar{r}) G(|\bar{r} - \bar{r}'|)\, dv' \quad . \tag{35}$$

It is noteworthy that exactly the same calculation is needed to obtain $W(\bar{r})$ as was needed to find the first term in the Born series. It is tempting to conjecture that the realms of validity are therefore equal. However, this reasoning can be quickly dismissed when one realizes that the nature of the correction term in each case is quite different. In Born theory, the correction term is summed with the unscattered field to get the total field, while in Rytov theory the correction to complex phase (i.e. ψ_1) appears in the total field in a multiplicative fashion. Clearly, the range of validity of the two approaches need not be the same.

The derivation of Rytov theory just completed contains only one noteworthy assumption, namely that $|\nabla\psi_1| << |\nabla\psi_0| \sim k$. This is equivalent to saying that the change in the correction to complex phase over distances of a wavelength is much less than 2π radians. If we recall that $\lambda << \ell_o$, this condition would seem very tolerable and we would conclude that Rytov theory has an extremely large range of validity. Actually, this does not seem to be the case. Present thinking on the relative merits of the three preceding approaches is discussed in the following section.

1.4 Comparison of Theoretical Approaches: Relative Range of Validity

Considering geometrical optics first, we noted earlier that this approach neglected diffraction effects. In addition, refractive effects on off-axis ray bundles will result in caustics and cause a "spill over" of energy into the on-axis ray bundle. This mechanism is also neglected. The usual sufficiency condition applied for a geometrical optics approach to be valid is that the path length L be much less than ℓ_o^2/λ. For typical near-ground propagation, this results in an L value of a few meters. Taylor[47,48] has questioned the validity of this criterion (i.e., $L << \ell_o^2/\lambda$) and raises the possibility that the ray optics technique may be valid out to several hundred meters. A complicating factor in the discussion is that one must define the statistic of interest before assigning a range of validity to a technique.[49] It is clear that phase fluctuations are handled in a more adequate fashion than amplitude fluctuations by ray optics. This follows since the answer one gets for the phase structure function through ray optics is the same as the answer obtained through wave optics.[50]

Perhaps the most straightforward experimental method for finding the geometrical optic limit for amplitude analysis would be to transmit two widely spaced (e.g., $\Delta\lambda \sim 1$ micrometer) optical beams over a variable-length path. Since geometrical optics is the high-frequency approximation to the propagation phenomena, it has no wave-number dependence in the calculation of amplitude fluctuations; the appearance of a statistical difference in the amplitude fluctuations of the two beams could be interpreted as the break-down point of the ray optic amplitude calculation. This type of experiment has not to the author's

knowledge been carried out, and we are without any definitive experimental investigation of the problem. However, it can be noted on the basis of the results presented in Section 2.2 of this report that over a near-ground horizontal path under weak turbulence conditions (i.e., at night) the valid range for amplitude calculations is much less than 1.17 KM. The problem is not as perplexing as it might seem, since the geometrical optics approach can be shown to be a special case of the more general wave treatment;[51,52] therefore, any needed result can be obtained using wave optics (assuming the mathematics are tractable).

Single-scatter Born theory is seriously hampered by the restriction $|E_1/E_0| \ll 1$. To gain some insight into the magnitude of the problem, we consider Protheroe's[53] measurements of stellar irradiance fluctuations as a function of zenith angle. Under the weakest scintillation conditions, (i.e. the star is at zenith and chromatic averaging is allowed), the normalized irradiance fluctuation (standard deviation divided by mean) is about 36%. So clearly, even this rather mildly turbulent path is beyond the scope of single-scatter Born theory. Typical near-ground paths exceeding a few hundred meters in length induce visible amplitude fluctuations which are larger than stellar scintillation and are also not amenable to this technique. It is possible, however, that for infrared sources the magnitude of the wave fluctuations in many cases may be sufficiently small so that single-scatter theory is applicable for these ranges.

Rytov theory contains only one notable assumption; namely, that the correction term to the complex phase changes little over distances of a wavelength. As noted earlier, this is not a significant restriction for most problems; therefore, one is tempted to conclude that the range of validity is great. However, the method

has been questioned both in the Soviet Union[54-56] (as reported by Strohbehn) and in the United States.[57] DeWolf[52] argued that the method included geometrical optics and single-scatter Born theory and had a range of validity much greater than either. Brown[58] viewed the technique as a perturbation solution to the nonlinear Ricatti equation; after calculating the next higher term in the solution, he concluded that the Rytov technique was valid only in situations where the single-scatter theory could be applied. Fried[59] interpreted Coulman's data[60] as experimental proof that the Rytov approximation gave accurate answers in situations which could not be handled by single-scatter or ray optic theory. Various other papers have appeared either defending[61-63] or criticizing[64] the usefulness of the approach.

Perhaps the most meaningful conclusion that can be drawn in this situation is that the problem is not likely to be clearly and decisively resolved through analytical efforts. Properly designed experiments should be able to settle the issue and in fact, to this writer, it appears that certain aspects of the problem are now resolvable. In view of the data presented in this report as well as other recent experimental results,[46] it seems clear that Rytov theory accurately predicts amplitude statistics in cases where neither geometrical optics nor single-scatter theory is applicable. The remaining task is to determine the parameter ranges over which reliable answers for amplitude statistics can be expected. Specifically, the level at which the variance of log amplitude saturates is usually regarded as the upper limit for useful amplitude calculations. The available experimental data on this subject are contradictory. Section 2.3 includes a discussion of these data and presents new data which may help to clarify the problem.

Little can be said about phase statistics, since experimental data is so sparse. We note, however, that second-order statistics such as the phase structure function are not appreciably different for the geometrical optics and the wave optics approach. In any case, it is thought that solutions for phase statistics using Rytov's method will be valid for wider ranges than those for amplitude statistics.[45]

There are a number of well-known theoretical approaches which have been neglected for various reasons. Hufnagel and Stanley's[57] Mutual Coherence Function approach gives results which are in exact agreement with Tatarski[2]; in fact, their results may be considered a specialization of Tatarski's more general results. The renormalization technique advocated by deWolf[52,65,66] has the interesting facet that it predicts a saturation of irradiance fluctuations. In addition, the amplitude fluctuations are said to follow a Rayleigh or Rice distribution in place of the usually assumed log-normal behavior. However, the approach with its various approximations has not yet been subjected to a thorough critical review. In addition, the predicted saturation level is appreciably less than some of the measured values.

In summary, it appears that Rytov theory, although it has certain limits which at this time are not well defined, is the most fruitful approach available to the propagation problem. Subsequent sections of this report will emphasize results obtained from Rytov theory.

1.5 Theoretical Results

This section is a summary of theoretical results which have been evaluated for various types of optical propagation problem. We restrict ourselves to

those results which have developed based on the Kolmogorov Theory of Turbulence. Therefore, we feel that the validity of contemporary optical propagation theory can be rigorously tested by comparing these results to the outcomes of properly designed experiments.

The notational differences between authors is considerable, and we have attempted to standardize. This occasionally causes the constants in various equations to differ slightly from the original published values. The classification of results is according to type of source (infinite plane wave, spherical wave, finite gaussian beam) and propagation path (homogeneous turbulence, non-homogeneous turbulence). Non-homogeneous means simply that C_n^2 is a slowly varying function of position along the path. The assumed spatial dependence will be given for each case. For each group of results, the listed order agrees chronologically with appearance in the published literature. The classification of results is as follows:

(1) Infinite plane wave, homogeneous turbulence.

(2) Spherical wave, homogeneous turbulence.

(3) Finite gaussian beam, homogeneous turbulence.

(4) Infinite plane wave, non-homogeneous turbulence.

(5) Spherical wave, non-homogeneous turbulence.

(6) Finite gaussian beam, non-homogeneous turbulence.

LIST OF NOTATIONS

Common notation:

Log amplitude $\chi(\bar{x}) = 1/2\ ln\left[u(\bar{x})/u_0(\bar{x})\right]$,

where $u(\bar{x})$ is the field at $\bar{x}$ and $u_0(\bar{x})$ is the RMS field value at the same point.

Optical carrier phase: $\phi(\bar{x})$.

Refractive index structure constant as defined through the Kolmogorov "2/3 law": C_n^2.

L_o and ℓ_o : outer and inner scales of turbulence which define the limits of the Kolmogorov spectrum.

Wave number of the radiation: $k = 2\pi/\lambda$.

Length of propagation path: L.

Inner scale parameter: $k_m = (5.48/\ell_o)$.

Infinite plane wave:

Log amplitude covariance:

$$C_\chi(\rho) = \left\langle \left(\chi(\bar{r}) - \langle\chi(\bar{r})\rangle\right)\left(\chi(\bar{r}+\bar{\rho}) - \langle\chi(\bar{r}+\bar{\rho})\rangle\right)\right\rangle,$$

where $\bar{r}$ and $\bar{\rho}$ are position vectors perpendicular to the propagation path, and the assumptions of homogeneity and isotropy for χ have been made by writing $C_\chi(\bar{\rho})$ as $C_\chi(\rho)$.

Log-amplitude variance: $C_\chi(0) = \left\langle\left[\chi(\bar{r}) - \langle\chi(\bar{r})\rangle\right]^2\right\rangle$.

Log-amplitude structure function: $D_\chi(\rho) = \left\langle\left[\chi(\bar{r}) - \chi(\bar{r}+\bar{\rho})\right]^2\right\rangle$

$= 2\left[C_\chi(0) - C_\chi(\rho)\right]$.

Phase structure function: $D_\phi(\rho) = \left\langle\left[\phi(\bar{r}) - \phi(\bar{r}+\bar{\rho})\right]^2\right\rangle$.

Mutual coherence function: $M(\rho) = \left\langle u(\bar{r})\, u^*(\bar{r}+\bar{\rho})\right\rangle$.

Spherical wave:

Log-amplitude covariance: $C_\ell^S(\rho)$.

Log-amplitude variance: $C_\ell^S(0)$.

Phase structure function: $D_\phi^S(\rho)$.

Finite gaussian beam:

Standard deviation of amplitude profile: a_0,

i.e., beam amplitude profile is proportional to

$\exp\left[-\xi^2/2a_0^2\right]$.

On-axis log amplitude variance: $C_\ell^L(0, 0)$.

Log-amplitude variance as measured a distance R off the propagation axis: $C_\ell^L(0, R)$.

Mean value of log amplitude: $\langle \ell^L \rangle$.

Phase structure function: $D_\phi^L(s, S)$,

where s and S specify the position of the two measurement points with respect to the propagation axis.

Theoretical Results

a. Infinite Plane Wave, Homogeneous Turbulence. For $\sqrt{\lambda L} << \ell_0$ (i.e., geometrical optics),

$$C_\ell(0) = 2.46\, C_n^2 L^3 \ell_0^{-7/3}, \tag{36}$$

$$C_\ell(\rho) = 2\pi(0.017) L^3 C_n^2 \int_0^{\kappa_m} J_0(\kappa\rho)\, \kappa^{4/3}\, d\kappa, \tag{37}$$

$$D_\phi(\rho) = 3.44 k^2 L C_n^2 \rho^2 \ell_0^{-1/3}, \text{ with } \rho << \ell_0, \tag{38}$$

and

$$D_\phi(\rho) = 2.91 k^2 L C_n^2 \rho^{5/3}, \text{ with } \rho >> \kappa_m. \tag{39}$$

For $\sqrt{\lambda L} >> \ell_o$ (i.e., wave optics),

$$C_\ell(0) = 0.31 C_n^2 k^{7/6} L^{11/6}, \tag{40}$$

$$C_\ell(\rho) = 2\pi^2(0.033) C_n^2 k^2 L \int_0^\infty J_0(\kappa\rho)\left\{1 - \frac{k}{\kappa^2 L} \sin\frac{\kappa^2 L}{k}\right\}\kappa^{-8/3} d\kappa, \tag{41}$$

for $\rho >> \ell_o$,

and

$$D_\ell(\rho) = 1.72 C_n^2 k^2 L \ell_o^{-1/3} \rho^2, \text{ for } \rho << \ell_o. \tag{42}$$

Also, for $\rho >> \ell_o$ and for $\rho \geq \sqrt{\lambda L}$,

$$D_\phi(\rho) = 2.91 k^2 L C_n^2 \rho^{5/3}, \tag{43}$$

and for $\rho < \sqrt{\lambda L}$,

$$D_\phi(\rho) = 1.46 k^2 L C_n^2 \rho^{5/3}. \tag{44}$$

For $\rho << \ell_o$,

$$D_\phi(\rho) = 1.72 C_n^2 \ell_0^{-1/3} k^2 L \rho^2. \tag{45}$$

The above results, Eqs. 36-45, are due to Tatarski.[2] The integrals in Eqs. 37 and 41 have been evaluated numerically by him and are shown in his Figs. 8 and 13.

The following results (Eqs. 46-48) are due to Fried.[67]

For $\sqrt{\lambda L} >> \ell_o$,

$$C_\ell(\rho)/C_\ell(0) = \sum_{n=0}^{\infty}\left[a_n + b_n\left(\frac{k\rho^2}{4L}\right)\right]\cdot\left[\left(\frac{k\rho^2}{4L}\right)^{2n}\Big/(2n)!\right] - 7.53034\left(\frac{k\rho^2}{4L}\right)^{5/6}, \quad (46)$$

$$C_\ell(0) = 0.309\,k^{7/6}L^{11/6}C_n^2, \quad (47)$$

and

$$D_\phi(\rho)/C_\ell(0) = 2\left\{-1 + 7.53034\left(\frac{k\rho^2}{4L}\right)^{5/6} + \sum_{n=0}^{\infty}\left[a_n + b_n\left(\frac{k\rho^2}{4L}\right)\right]\left(\frac{k\rho^2}{4L}\right)^{2n}\frac{1}{(2n)!}\right\}. \quad (48)$$

The first ten values of a_n, b_n used in Eqs. 46 and 48 are listed in Table I and the results of Eqs. 46 and 48 are plotted in Fried's Figs. 1 and 3.[67]

TABLE I

Coefficients for Eqs. 46 and 48

n	a_n	b_n
0	1.00000	6.84209
1	-7.63889×10^{-1}	5.27939×10^{-2}
2	1.23778×10^{-2}	-4.00354×10^{-3}
3	-2.83086×10^{-3}	8.98375×10^{-4}
4	1.08825×10^{-3}	-3.09202×10^{-4}
5	-5.34385×10^{-4}	1.34605×10^{-4}
6	3.03065×10^{-4}	-6.80418×10^{-5}
7	-1.89046×10^{-4}	3.81508×10^{-5}
8	1.26184×10^{-4}	-2.30845×10^{-5}
9	-8.86012×10^{-5}	1.48081×10^{-5}

The mutual coherence function for an infinite plane wave as measured on a plane perpendicular to the direction of propagation was evaluated by Hufnagel and Stanley[57] as

$$M(\rho) = \exp\left[-\frac{1}{2}\left(2.91\,k^2\,\rho^{5/3}\int_0^L C_n^2(\ell)\,d\ell\right)\right], \tag{49}$$

where the integration is over the propagation path. Therefore, for homogeneous turbulence,

$$M(\rho) = \exp\left[-\frac{1}{2}\left(2.91\,k^2\,\rho^{5/3}\,C_n^2\,L\right)\right]. \tag{50}$$

b. Spherical Wave, Homogeneous Turbulence. From Tatarski,[2] for $\sqrt{\lambda L} << \ell_o$,

$$C_\ell(0) = 0.246\,C_n^2\,L^3\,\ell_o^{-7/3}, \tag{51}$$

and, for $\sqrt{\lambda L} >> \ell_o$,

$$C_\ell(0) = 0.13\,C_n^2\,L^{11/6}\,k^{7/6}. \tag{52}$$

From Fried,[68] for $\sqrt{\lambda L} >> \ell_o$, we have

$$C_\ell^S(\rho)/C_\ell^S(0) = \sum_{n=0}^{\infty}\left\{a_n + b_n\left[\frac{k\rho^2}{4L}\right] + c_n\left[\frac{k\rho^2}{4L}\right]^{17/6}\right\}\times \left[\frac{k\rho^2}{4L}\right]^{2n}\frac{1}{(2n)!} - 6.98442\left[\frac{k\rho^2}{4L}\right]^{5/6}, \tag{53}$$

$$C_\ell^S(0) = 0.124\,k^{7/6}\,L^{11/6}\,C_n^2, \tag{54}$$

and

$$D_\phi^S(\rho)/C_\ell^S(0) = 2\left\{\sum_{n=0}^{\infty}\left[a_n + b_n\left(\frac{k\rho^2}{4L}\right) + c_n\left(\frac{k\rho^2}{4L}\right)^{17/6}\right]\times \left(\frac{k\rho^2}{4L}\right)^{2n}\frac{1}{(2n)!} - 1 + 6.98442\left(\frac{k\rho^2}{4L}\right)^{5/6}\right\}. \quad (55)$$

The first ten values of a_n, b_n, and c_n are listed in Table II; the evaluation of the right-hand sides of Eqs. 53 and 55 is shown in Fried's Figs. 1 and 2.[68]

TABLE II

Coefficients for Eqs. 53 and 55

n	a_n	b_n	c_n
0	1.00000	6.84218	2.53100
1	-2.59722	-4.12854	-0.389951
2	4.01006	3.49205	0.150525
3	-5.32819	-3.17894	-0.0790161
4	6.58359	2.98285	0.0485236
5	-7.79261	-2.84418	-0.0327814
6	8.96511	2.73873	0.0236145
7	-10.1076	-2.65456	-0.0178143
8	11.2249	2.58505	0.0139142
9	-12.3202	-2.52616	-0.0111669

c. Finite Gaussian Beam, Homogeneous Turbulence. From Kon and Tatarski[69] we have, for a collimated beam with $\sqrt{\lambda L} << \ell_o$,

$$D_\phi(s, S) = 1.64\, C_n^2\, \ell_o^{-1/3}\, L k^2 s^2 \left[1 + {}_1F_1\left(1/6,\ 2,\ 1.16\, \frac{S^2 L^2 \kappa_m^2}{k\alpha_0^2}\right)\right], \quad (56)$$

where

$$\bar{s} = \bar{\rho}_1 - \bar{\rho}_2$$

and

$$\bar{S} = \left(\bar{\rho}_1 + \bar{\rho}_2\right)/2 .$$

$\bar{\rho}_1$ and $\bar{\rho}_2$ are the position vectors of the observation points with respect to the beam axis. ${}_1F_1$ is the confluent hypergeometric function, and the assumptions $\sqrt{\lambda L} << \ell_o$ and near-field operation have been incorporated. In addition, Eq. 56 has been written for the case where the observation points lie on a straight line passing through the beam axis.

For the wave optics case ($\sqrt{\lambda L} >> \ell_o$) with $L^2 \kappa_m^2 / k^2 \alpha_0^2 >> 1$,

$$D_\phi(s, S) = 0.617\, k^3 \alpha_0\, C_n^2\, \kappa_m^{-2/3}\, s^2\, ln\left(\frac{2.7 L^4 \kappa_m^4}{k^4 \alpha_0^4}\right) \times$$

$$\left[2\, {}_1F_1\left(1/6,\ 1,\ s^2/\alpha_0^2\right) - {}_1F_1\left(1/6,\ 2,\ s^2/\alpha_0^2\right)\right] . \quad (57)$$

From Fried[70] we have the following results for amplitude statistics. For collimated beam propagation,

$$C_\chi^L(0, 0)/C_\chi^S(0) = f\left(\frac{k\alpha_0^2}{L}\right), \quad (58)$$

where f is evaluated for argument values ranging from 0.005 to 128.0 in Table III.

TABLE III

Coefficients for Eq. 58

(ka_0^2/L)	$f(ka_0^2/L)$	(ka_0^2/L)	$f(ka_0^2/L)$
0.005	0.9548	0.60	0.6237
0.01	0.9268	0.70	0.6590
0.02	0.8844	0.80	0.7000
0.03	0.8510	0.90	0.7442
0.04	0.8232	1.0	0.7901
0.05	0.7991	2.0	1.1947
0.10	0.7129	4.0	1.6120
0.15	0.6593	8.0	1.9239
0.20	0.6243	16.0	2.1356
0.25	0.6019	32.0	2.2712
0.30	0.5890	64.0	2.3708
0.40	0.5834	128.0	2.3774
0.50	0.5971		

For focused beam propagation ,

$$C_{\ell}^{L}(0, 0)/C_{\ell}^{S}(0) = g\left(\frac{ka_0^2}{L}\right), \tag{59}$$

where the function g is shown for discrete argument values in Table IV.

TABLE IV

Coefficients for Eq. 59

$k\alpha_0^2/L$	$g(k\alpha_0^2/L)$	$k\alpha_0^2/L$	$g(k\alpha_0^2/L)$
0.005	0.9547	0.60	0.3691
0.01	0.9266	0.70	0.3402
0.02	0.8837	0.80	0.3157
0.03	0.8496	0.90	0.2948
0.04	0.8208	1.0	0.2766
0.05	0.7955	2.0	0.1723
0.10	0.7001	4.0	0.09827
0.15	0.6329	8.0	0.05212
0.20	0.5811	16.0	0.02606
0.25	0.5390	32.0	0.01234
0.30	0.5039	64.0	0.005583
0.40	0.4476	128.0	0.002304
0.50	0.4041		

We emphasize that Eqs. 58 and 59 hold only for measurement points on or near the axis of propagation. The results (Eqs. 58 and 59) are plotted in Fried's Fig. 1.[70]

Results for the behavior of the log-amplitude variance off-axis are available from Ho.[71] These results are restricted to measurement points which lie in the near field of the transmitter aperture as well as to collimated beams. For $\sqrt{\lambda L} << \ell_o$,

$$C_\ell^L(0, R) = C_\ell(0)\left[1 - .815\left(\frac{L^2 \kappa_m^2}{k\alpha_0^2}\right) + \frac{10.3\, R^2}{\alpha_0^4 \kappa_m}\right], \tag{60}$$

$$C_\ell(0) = 0.0108\,\Gamma(1/6)\,C_n^2\,\kappa_m^{7/3}\,L^3, \tag{61}$$

and

$$C_\ell^L(0,\,0) = C_\ell(0)\left[1 - .815\left(\frac{L^2\,\kappa_m^2}{k^2\,a_0^2}\right)\right]. \tag{62}$$

For $\sqrt{\lambda L} >> \ell_o$,

$$C_\ell^L(0,\,R) = C_\ell(0)\left[1 - 2\left(1 - \frac{R^2}{a_0^2}\right)\left(\frac{L^2\,\kappa_m^2}{k^2\,a_0^2}\right)\left(\frac{L\kappa_m^2}{k}\right)^{-5/6} + \frac{2L}{k a_0^2}\right], \tag{63}$$

$$C_\ell(0) = 0.0552\,\Gamma(1/6)\,C_n^2\,k^{7/6}\,L^{11/6}, \tag{64}$$

and

$$C_\ell^L(0,\,0) = C_\ell(0)\left[1 - 1.97\left(\frac{L}{k a_0^2}\right)\left(1.025\left(\frac{L\kappa_m^2}{k}\right)^{1/6} - 1.02\right)\right]. \tag{65}$$

For clarity, we restate that R is the measurement point's off-axis radial distance and $C_\ell(0)$ is the log-amplitude variance for an infinite plane wave traversing the same path. Ho's results are plotted in his Figs. 1 and 2.[71]

More general results are available from Ishimaru.[72] These results are valid for collimated beams and a vanishingly small inner scale. The most useful results of this work take the form

$$C_\ell^L(0,\,R) = \pi^2\left(0.033\,C_n^2\right)\Gamma(-5/6)\,k^{7/6}\,L^{11/6}\left\{\frac{\alpha L}{1 + (\alpha L)^2}\right\}^{5/6} \times$$

$$\left\{\frac{3}{8}\,{}_1F_1\left(-\frac{5}{6},\,1;\,\frac{2R^2}{2a_0^2\left[1 + (\alpha L)^2\right]}\right) - g(\alpha L)\right\}, \tag{66}$$

where

$$g(\alpha L) = \int_0^1 \mathrm{Re}\left\{(1-x)^2 - \frac{i\left[1+(\alpha L)^2 x\right][1-x]}{\alpha L}\right\}^{5/6} dx$$

$$= \frac{6}{11}\,\mathrm{Re}\left\{\left(\frac{1+i\alpha L}{i\alpha L}\right)^{5/6} \cdot {}_2F_1\left(-\frac{5}{6}, 1; \frac{17}{6}; i\alpha L\right)\right\}. \qquad (67)$$

${}_2F_1$ is the hypergeometric function and $\alpha = \lambda/2\pi\,\alpha_0^2$. On the beam axis, the log-amplitude variance is

$$C_\ell^L(0,0) = \pi^2\left(0.033\,C_n^2\right)\Gamma(-5/6)\,k^{7/6}\,L^{11/6}\left\{\frac{\alpha L}{1+(\alpha L)^2}\right\}^{5/6}\left\{\frac{3}{8} - g(\alpha L)\right\}. \qquad (68)$$

Eq. 68 is plotted as a function of αL in Ishimaru's Fig. 4, and it is shown there that $C_\ell^L(0,0)$ increases initially at a rate between the rates for plane and spherical waves, eventually crosses the spherical-wave value, and thereafter grows at a lesser rate.

The mean value for log amplitude has been evaluated by Gebhardt and Collins[73] for the case where the detector is on or near the propagation axis and is in the near field of the transmitter. The analysis is based on prior work by Schmeltzer[74] and is valid for focused and collimated-beam propagation.

For collimated-beam propagation, it is seen that

$$\langle \ell \rangle / C_\ell^S(0) = M\left(\frac{k\alpha_0^2}{L}\right), \qquad (69)$$

where M was evaluated at discrete argument values as shown in Table V.

TABLE V

Coefficients for Eq. 69

ka_0^2/L	$M(ka_0/L)$	ka_0^2/L	$M(ka_0/L)$
0.005	-2.796590	0.60	-2.071238
0.01	-2.730011	0.70	-2.089343
0.02	-2.632161	0.80	-2.108799
0.03	-2.558014	0.90	-2.128209
0.04	-2.497791	1.0	-2.146857
0.05	-2.447162	2.0	-2.273239
0.10	-2.276834	4.0	-2.365396
0.15	-2.180511	8.0	-2.417845
0.20	-2.122361	16.0	-2.445360
0.25	-2.087121	32.0	-2.459626
0.30	-2.066645	64.0	-2.468092
0.40	-2.052230	128.0	-2.473000
0.50	-2.057157		

For focused-beam propagation,

$$\langle \ell \rangle / C_\ell^S(0) = N\left(\frac{ka_0^2}{L}\right) . \tag{70}$$

This result is shown in Table VI, and both results (Eqs. 69 and 70) are plotted in Gebhardt and Collins' Fig. 1.[73]

TABLE VI

Coefficients for Eq. 70

$k\alpha_0^2/L$	$N(k\alpha_0^2/L)$	$k\alpha_0^2/L$	$N(k\alpha_0^2/L)$
0.005	-2.796449	0.60	-1.755759
0.01	-2.729521	0.70	-1.730162
0.02	-2.630392	0.80	-1.711608
0.03	-2.554293	0.90	-1.698131
0.04	-2.491542	1.0	-1.688406
0.05	-2.437886	2.0	-1.677912
0.10	-2.246825	4.0	-1.740934
0.15	-2.123765	8.0	-1.838889
0.20	-2.035778	16.0	-1.936671
0.25	-1.969364	32.0	-2.015523
0.30	-1.917504	64.0	-2.071282
0.40	-1.842334	128.0	-2.107402
0.50	-1.791461		

d. Infinite Plane Wave, Non-Homogeneous Turbulence. From Tatarski,[75] we have, for geometrical optics $(\sqrt{\lambda L} << \ell_o)$,

$$C_\ell(0) = 7.37\,\ell_o^{-7/3} \int_0^L C_n^2(x)\,x^2\,dx, \tag{71}$$

and, for wave optics $(\sqrt{\lambda L} >> \ell_o)$,

$$C_\ell(0) = 0.56\,k^{7/6} \int_0^L C_n^2(x)\,x^{5/6}\,dx, \tag{72}$$

where the integration variable x is the distance from the observation point to the part of the path being considered. Also,

$$D_\phi(\rho) + D_\ell(\rho) = 2.91\, k^2 \rho^{5/3} \int_0^L C_n^2(x)\, dx \ . \tag{73}$$

For $\ell << \rho << \sqrt{\lambda L}$,

$$D_\phi(\rho) = 1.46\, k^2 \rho^{5/3} \int_0^L C_n^2(x)\, dx \ . \tag{74}$$

For $\rho \geq \sqrt{\lambda L} >> \ell_o$,

$$D_\phi(\rho) = 2.91\, k^2 \rho^{5/3} \int_0^L C_n^2(x)\, dx \ . \tag{75}$$

Two models for the turbulence are used for calculations. For

$$C_n^2(x) = C_{n0}^2 \exp\left[-x/x_0\right] \ ,$$

the wave optics solutions become

$$C_\ell(0) = 0.53\, C_{n0}^2 \exp\left[-x/x_0\right] \tag{72A}$$

and

$$D_\phi(\rho) = 2.91\, k^2 \rho^{5/3} C_{n0}^2\, x_0 \ , \tag{75A}$$

and, for

$$C_n^2(x) = C_{n0}^2 \left[\frac{1}{1 + (x/x_0)^2}\right] ,$$

they become

$$C_\ell(0) = 3.4 C_{n0}^2 k^{7/6} x_0^{11/6} \tag{72B}$$

and

$$D_\phi(\rho) = 4.57 C_{n0}^2 k^2 \rho^{5/3} x_0 . \tag{75B}$$

The above results (Eqs. 71-75B) are discussed in the context of the stellar "seeing" problem in Chapter 8 of Tatarski.[2] Fried[76] has investigated the same problem using the more realistic turbulence model

$$C_n^2(h) = 4.2 \times 10^{-14} h^{-1/3} \exp\left[-h/h_0\right] , \tag{76}$$

where h is the altitude measured from sea-level and h_0 is the scale height of the atmosphere (3200 meters). The results are

$$C_\ell(0) = 0.730 \cos^{-11/6}\theta \left(\frac{5 \times 10^{-7}}{\lambda}\right)^{7/6} , \tag{77}$$

$$C_\ell(\rho)/C_\ell(0) = \sum \left\{a_n + b_n \left(\frac{k\rho^2}{4h_0 \sec\theta}\right) + c_n \left(\frac{k\rho^2}{4h_0 \sec\theta}\right)^{3/2} + d_n \left(\frac{k\rho^2}{4h_0 \sec\theta}\right)\right\} \times$$

$$\left\{\left(\frac{k\rho^2}{4h_0 \sec\theta}\right)^{2n} \left(\frac{1}{(2n)!}\right)^2\right\} - 6.27602 \left(\frac{k\rho^2}{4h_0 \sec\theta}\right)^{5/6} , \tag{78}$$

and

$$D_\phi(\rho)/C_\ell(0) = 2\left\{-1 + 6.27602\left(\frac{k\rho^2}{4h_0 \sec\theta}\right)^{5/6} + \sum_{n=0}^{\infty}\left[a_n + b_n\left(\frac{k\rho^2}{4h_0 \sec\theta}\right) + c_n\left(\frac{k\rho^2}{4h_0 \sec\theta}\right)^{3/2} + d_n\left(\frac{k\rho^2}{4h_0 \sec\theta}\right)^{5/2}\right]\frac{\left(k\rho^2/4h_0 \sec\theta\right)^{2n}}{[(2n)!]^2}\right\}, \quad (79)$$

where θ is the zenith angle of the source and the coefficients a_n, b_n, c_n, and d_n are listed in Table VII. The results of Eqs. 78 and 79 are plotted in Fried's Figs. 2 and 4.[76]

TABLE VII

Coefficents for Eqs. 78 and 79

n	a_n	b_n	c_n	d_n
0	1.00000	6.22008	-7.85622×10^{-1}	1.45145×10^{-1}
1	-5.55556×10^{-1}	-1.79179×10^{-1}	2.28026×10^{-2}	-1.73367×10^{-3}
2	3.74486×10^{-1}	5.05797×10^{-2}	-4.36773×10^{-3}	1.67119×10^{-4}
3	-3.13723×10^{-1}	-2.24463×10^{-2}	1.45802×10^{-3}	-3.32886×10^{-5}
4	2.79596×10^{-1}	1.23097×10^{-2}	-6.40001×10^{-4}	9.68214×10^{-6}
5	-2.56692×10^{-1}	-7.63945×10^{-3}	3.30962×10^{-4}	-3.55757×10^{-6}
6	2.39822×10^{-1}	5.14252×10^{-3}	-1.90915×10^{-4}	1.53244×10^{-6}
7	-2.26661×10^{-1}	-3.66677×10^{-3}	1.19079×10^{-4}	-7.40745×10^{-7}
8	2.15982×10^{-1}	2.72914×10^{-3}	-7.87611×10^{-5}	3.90776×10^{-7}
9	-2.07068×10^{-1}	-2.09991×10^{-3}	5.45286×10^{-5}	-2.20795×10^{-7}

e. Spherical Wave, Non-Homogeneous Turbulence. From Fried[77] we have the following general result:

$$D_\phi(\rho) + D_\ell(\rho) = 2.91\, k^2 \rho^{5/3} \int_0^L C_n^2(x) \left(\frac{x}{L}\right)^{5/3} dx, \tag{80}$$

where, in this case, x is the distance from the source to a point on the propagation path and L is the total path length. Also, from Fried[78] we have

$$C_\ell^S(0) = 0.727 \sec^{11/6}\theta \left(\frac{5 \times 10^{-7}}{\lambda}\right)^{7/6}, \tag{81}$$

where the turbulent profile of Eq. 76 has been used and it is assumed that the measurement point is at a much greater altitude than h_0 (3200 meters).

f. Finite Gaussian Beam, Non-Homogeneous Turbulence. From Fried,[78]

$$C_\ell^L(0, 0)/C_\ell^S(0) = \sum_{n=0}^{\infty} \left(a_n + b_n \Omega + c_n \Omega^{3/2} + d_n \Omega^{5/2}\right) \times \left(\frac{\Omega^{2n}}{[2n]!}\right) - 5.90358\, \Omega^{5/6}, \tag{82}$$

where

$$\Omega = \frac{k a_0^2}{h_0 \sec\theta},$$

and the coefficients are listed in Table VIII. Again, the turbulence model of Eq. 76 has been used and assumption of measurement ranges much greater than h_0 has been applied. Eq. 82 is plotted in Fried's Fig. 1.[78]

TABLE VIII

Coefficients for Eq. 82

n	a_n	b_n	c_n	d_n
0	1.00000	6.22009	-1.04436	4.82369×10^{-1}
1	-5.55555×10^{-1}	-5.37538×10^{-1}	1.32617×10^{-1}	-4.53727×10^{-2}
2	3.74486×10^{-1}	2.52899×10^{-1}	-5.23919×10^{-2}	1.30301×10^{-2}
3	-3.13723×10^{-1}	-1.57124×10^{-1}	2.84200×10^{-2}	-5.51539×10^{-3}
4	2.79596×10^{-1}	1.10788×10^{-1}	-1.79886×10^{-2}	2.85744×10^{-3}
5	-2.56692×10^{-1}	-8.40340×10^{-1}	1.24807×10^{-2}	-1.67697×10^{-3}
6	2.39822×10^{-1}	6.68528×10^{-2}	-9.20387×10^{-3}	1.07123×10^{-3}
7	-2.26661×10^{-1}	-5.50016×10^{-2}	7.08917×10^{-3}	-7.27633×10^{-4}
8	2.15983×10^{-1}	4.63955×10^{-2}	-5.64133×10^{-3}	5.17810×10^{-4}
9	-2.07068×10^{-1}	-3.98984×10^{-2}	4.60446×10^{-3}	-3.82207×10^{-4}

The preceding equations (Eqs. 36-82) are, to the author's knowledge, a complete listing of numerically useful results now available based on Kolmogorov turbulence theory. At the time of this writing, it appears that most theoretical efforts are being directed toward the finite gaussian beam propagation problem. This approach is particularly interesting since it is compatible with experiments utilizing laser sources. Also, the finite beam solutions must reduce in limiting cases to the spherical-wave and infinite-plane-wave results. The work of the Japanese group of Kinoshita, Asakura, and Suzuki [79-81] has been particularly

noteworthy. Using the Rytov approximation and a gaussian model for the covariance function of the refractive index field, this group has evaluated various second-order statistics for —

(1) Log amplitude.

(2) Phase.

(3) Joint log-amplitude-phase fluctuations throughout the beam.

The results pertain to homogeneous turbulence and focused, collimated, or uncollimated propagation. We do not list these results, however, since their accuracy is questionable owing to the gaussian turbulence model employed.

CHAPTER 2

EXPERIMENTAL RESULTS

2.1 Experimental Program

a. Introductory Remarks. The experimental side of the optical propagation problem has been investigated in one form or another for many years. Historically, astronomers who have studied the brightness and position fluctuations of stellar images must be regarded as the first experimentalists. However, these workers often failed to recognize the problem in its true statistical form; their measurements are difficult to interpret and, therefore, equally difficult to relate to contemporary theories. The pioneering theoretical treatise by Tatarski[2] also contained a substantial amount of experimental work, but these results have been criticized in recent years as regards the type of optical source and the data analysis procedures used. In general, the experimental situation is very confusing; only a few published results are widely accepted by workers in the field.

It should be clear that optical propagation measurements are useful only if they are taken in such a manner as to permit direct comparisons with theory. Otherwise, the measurements must be regarded as pertinent only for the time, location, and meteorological conditions under which they were taken. In principle, the experimenter should have knowledge of the statistical state of the turbulence

along the entire propagation path. Then a wave of the proper type (e.g., spherical, infinite plane) is launched into the medium, and the received fields are measured and statistically analyzed at the receiver. Practical limitations dictate that the number of meteorological stations be small, and one therefore usually chooses paths which are nearly uniform topologically. The measurements at a single station or the average of measurements at a few stations are used to characterize the turbulent state of the atmosphere along the entire path.

There are two primary reasons for seeking a theory which accurately predicts the effects of turbulence on optical waves. In the first case, the efficient implementation of optical systems for informational purposes requires that the designer be able to predict accurately the optical carrier fluctuations induced by the known (or assumed) turbulence. Therefore, for known turbulence models, systems can be optimized to reduce the effects of turbulence. In the second case, the optical fluctuations are used to infer the state of the turbulence. The measured field quantities are substituted into the theory, and a unique solution for the turbulence which caused the fluctuations is sought. Either approach requires the existence of an accurate theoretical treatment of the propagation problem.

In the work that follows, we emphasize the first type of problem, the optical communication problem. The experiments are designed to measure those parameters which control the quality of a communication channel. In all cases, the measurements are carried out in a manner which permits direct comparison with theory. The results to be presented hold for near-ground horizontal paths.

b. Test Facilities. All of the experiments to be described were performed on a test range operated by Goddard Space Flight Center about 5 miles east

of Greenbelt, Md. The range is located in an agricultural research area and consists mostly of live-stock graze-lands. The optical path lies approximately in an east-west geometry and has winds which are usually out of the northwest. At the west end of the path, a permanent structure houses all transmitting, receiving, and recording equipment. Two large mirrors are located on the range and serve to reflect transmitted beams back to the transmitter station. The transmitter and receiver systems are separated by about 1 meter, so that the optical path to and from the mirror has overlap only in a small region near the "folding" mirror. A profile of the optical path is shown in Fig. 1. The average beam height about ground level is 4.2 meters with a standard deviation of 1.3 meters.

The transmitter-receiver building is a 20' by 20' structure (Fig. 2) which is partitioned into two 10' by 20' sections. During experiments, one of these sections is well enough ventilated so that conditions remain near ambient. The other section contains all the apparatus requiring a stable environment and is heated and air-conditioned. The transmitter and receiver systems are mounted on a one-ton granite slab (Fig. 3). This table has three supports, which are isolated from the building floor and rest on the eight-inch-deep concrete pad beneath the building. The granite table can be "floated" on pneumatic supports (compressed nitrogen) for additional vibration isolation. In this condition, the system rejects input excitations of frequency 1 Hz or greater.

The first folding mirror is 50.8 cm in diameter and is located at a range of 583 meters. The mirror is in a two-axis adjustable mount (Fig. 4) and is attached to a one-ton concrete block. The second mirror (Fig. 5) is 30.5 cm in diameter

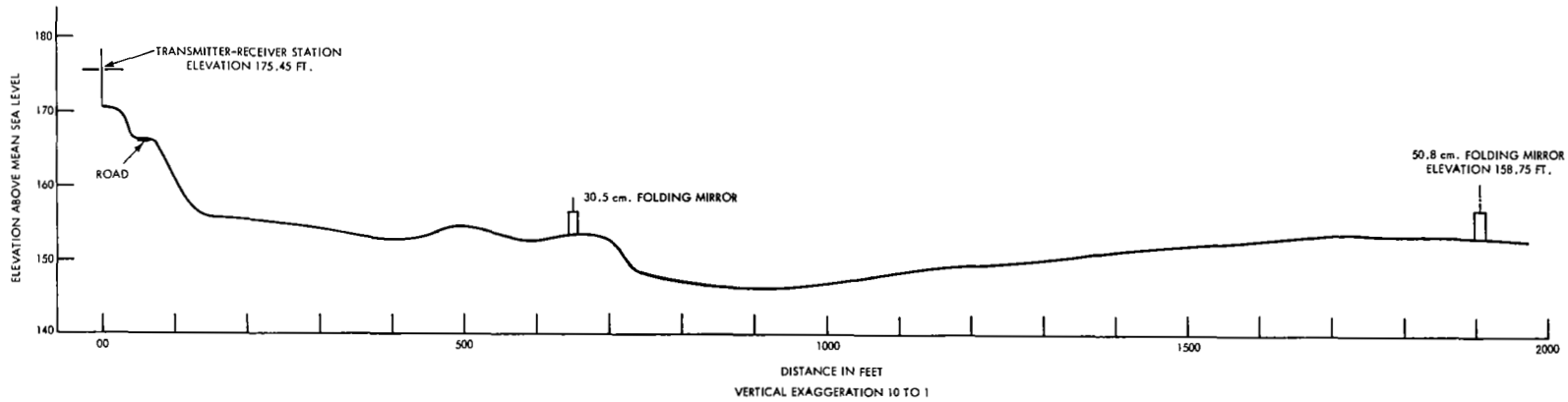

Figure 1. Profile of topography, optical propagation range, Goddard Space Flight Center, Greenbelt, Md.

Figure 2. Transmitter-receiver station. The building is 20' by 20' and sits on an 8-inch-deep concrete pad. Transmitted and received beams both go through the open window shown above.

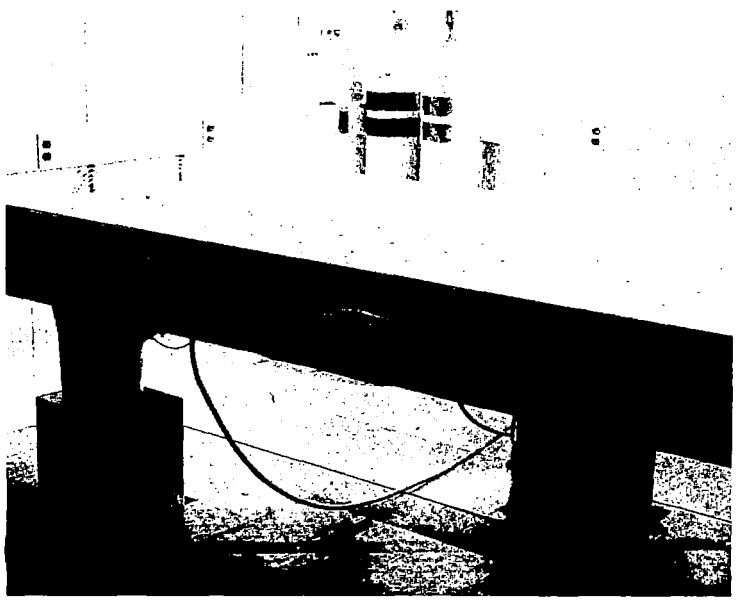

Figure 3. Stable transmitter-receiver platform. The compressed nitrogen tanks in the background can be used to "float" the table for additional vibration isolation.

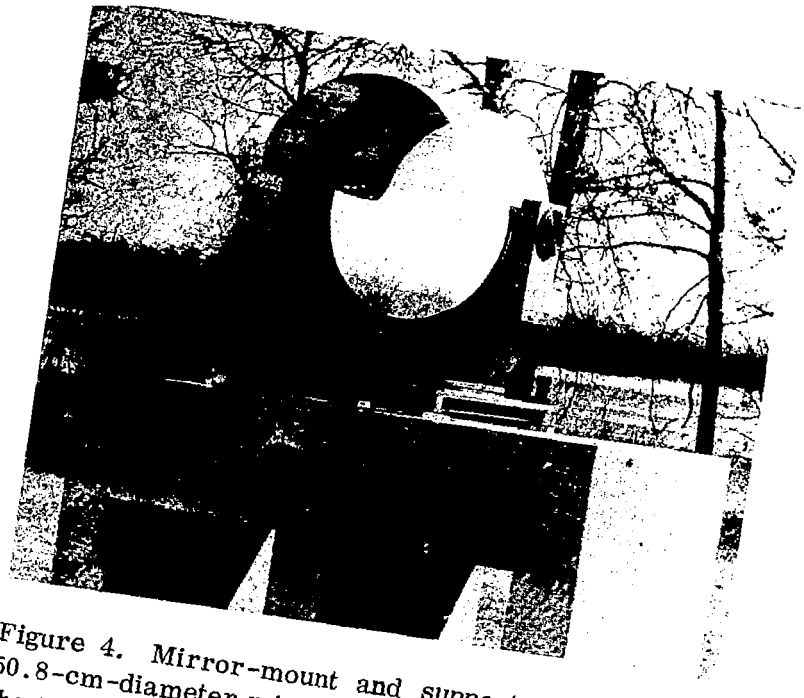

Figure 4. Mirror-mount and support. This is the 50.8-cm-diameter mirror, which is 583 meters from the transmitter.

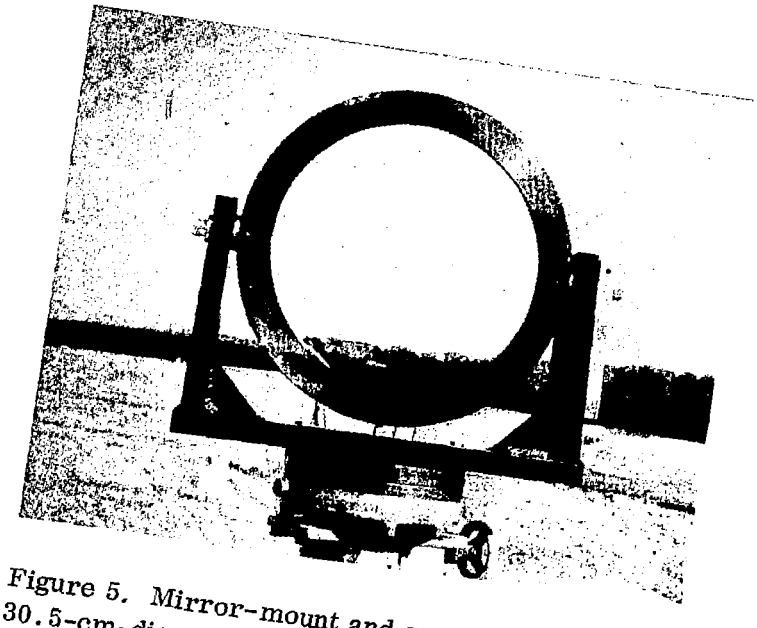

Figure 5. Mirror-mount and support. This is the 30.5-cm-diameter mirror, which is 200 meters from the transmitter. The transmitter-receiver station is imaged in the lower-left portion of the mirror.

and is also in an adjustable mount and located at a range of 200 meters. Both mirrors are optical-quality flats and are protected by shelters when not in use.

During data runs, the signals of interest were recorded on magnetic tape. The recorder was an Ampex FR-600, which is a 7-channel machine having either direct- or fm-recording capability on each track. Binary coded decimal time signals were also recorded, so that efficient data processing could be implemented. In all cases the recorder was run at 7-1/2 inches per second, which resulted in an fm bandwidth of DC to 2.5 kHz. Figure 6 shows the tape recorder and associated signal electronics.

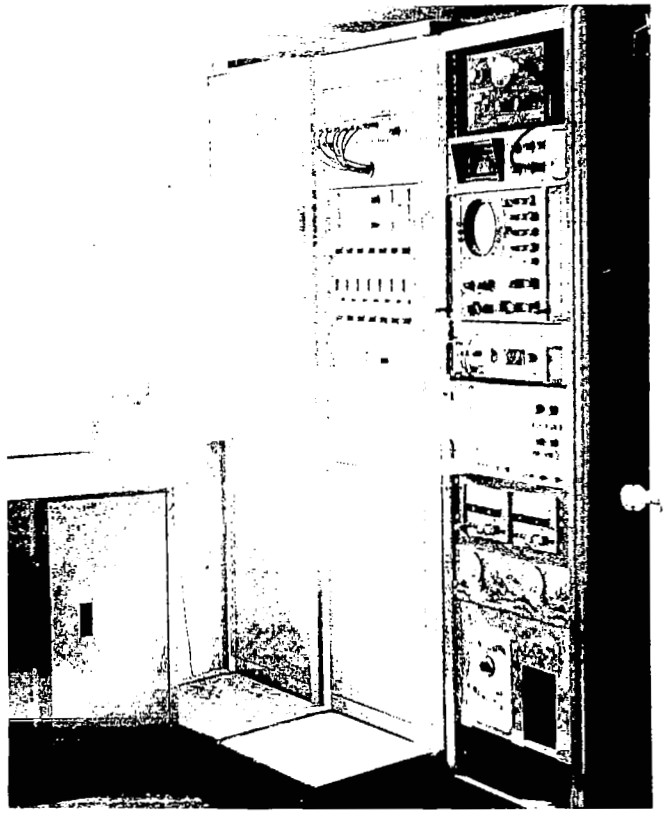

Figure 6. Magnetic tape recorder and supporting electronics. This system was located in the heated/air-conditioned portion of the building and was connected by about 25 feet of cable to the optical detectors.

Several data-processing techniques were used, depending on the statistic of interest. We discuss here only the digital computer approach and note that the other techniques will be discussed as they occur in the sections to follow. Two computers were used during the course of the program. The first was a Raytheon 520, which is a relatively small machine (8K memory). This machine had input analog-to-digital converters, with sample rates variable up to 10^4 per second. The playback of the tape recorder was sampled by these units 10^3 times per second and stored in the memory in correct time sequence. Data analysis was initiated manually by a switch and terminated when the designated number of samples had been stored. The program analyzed both the amplitude statistics of the signal (i.e., probability density, cumulative density, moments) and the time statistics (autocorrelation, power spectral density). After this procedure, each stored data point was normalized by the mean value of the original signal; then the natural logarithm was taken to produce the variable log amplitude. Identical amplitude and time analysis was then performed for log amplitude.

In order to process longer time records it was necessary to use a larger machine. The IBM 360/91 was therefore programmed to do the same analysis as outlined above, on longer data records. In this case, the analog data tape had to first be converted into a digital data tape. The digitization was carried out at a 1-kHz rate and with sufficient bits per sample point so that quantization noise was insignificant compared to other noise sources.

During all experiments the average meteorological conditions (temperature, pressure, relative humidity, wind magnitude, and direction) were monitored at the transceiver station. In addition, a pair of high-speed microthermal probes

were mounted near the west end of the path at a height of 4.15 meters in order to make direct measurements of the strength and spectrum of the temperature fluctuations. Figure 7 shows the pair of thermal sensors mounted on a wind-vane-type structure which was used to keep the sensor elements perpendicular to the wind vector. The center probe is a velocity sensor which was used for accurate wind speed measurements. The thermal sensor elements were 2.0-micron-diameter strands of platinum with a length of 1.6 mm. The system had a resolution of 0.01°C and a bandwidth of 1 kHz. The processing electronics for these sensors is shown in Fig. 8.

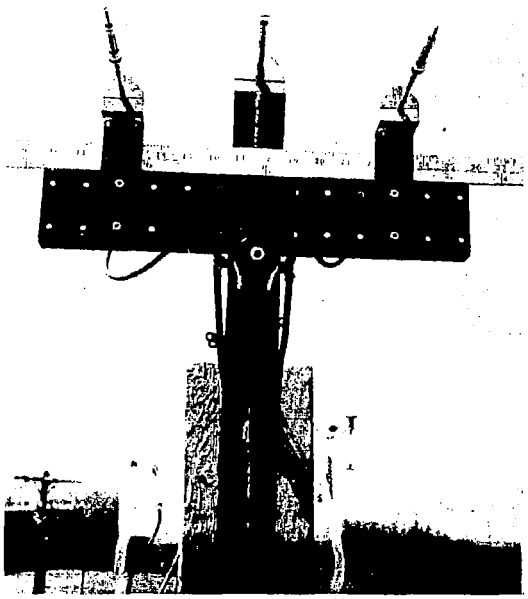

Figure 7. Micrometeorological measurement system. The center probe measures wind speed, while the two outside probes monitor microthermal fluctuations. The system was mounted 4.2 meters above ground, which was the average height of the propagation path.

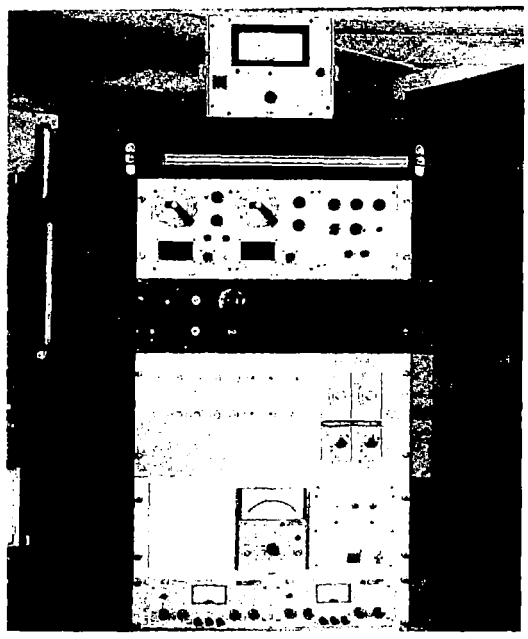

Figure 8. Processing electronics for micrometeorological system. The unit at the top of the rack is the velocity meter. The remainder of the system processed temperature and temperature-difference fluctuations.

We note that this experimental program was approximately a 2-year effort starting in Dec. 1967. Not all of the instrumentation described in this section was available at all times during the program. For example, the microthermal sensor system did not become operational until near the end of the program. Also, the shorter range capability provided by the 30.5-cm mirror was not available at the time of the dual-wavelength experiment (Section 2.2).

2.2 Wavelength Dependence of Laser Beam Scintillation*

a. Introduction. It is shown in Appendix B that the variance of log amplitude calculated through Rytov theory has a wavelength dependence $k^{(3/2 - p/2)}$, where p describes the spatial behavior of the refractive index fluctuations through

$$\left\langle \left[n(\bar{x} + r) - n(\bar{x}) \right]^2 \right\rangle \sim r^p \ . \tag{83}$$

Using the Obukhov-Kolmogorov turbulence model, we obtain

$$p = 2/3 \ .$$

Therefore the strength of optical fluctuations (as denoted by the log-amplitude variance) can be expected to vary as the 7/6 power of the wave number. The experiment described in this section was designed to test this theoretical prediction.

b. Experimental Technique. Because of the short-term stationarity and lack of statistical homogeneity of the atmosphere, the experimenter must transmit simultaneously through the same portion of the atmosphere at each wavelength of interest. The experiment is shown schematically in Fig. 9. A He-Ne laser at 0.632 micron and a CO_2 laser at 10.6 microns were aligned parallel, with an offset of 12 cm, and were operated over a folded horizontal 1.17-km path. The He-Ne output was unmodulated, and no external optics were used; thus, the assumptions of a spherical-wave transmitter were satisfied. The CO_2 output

*A substantial portion of the results of this section was presented to the Spring 1968 meeting of the Optical Society of America and subsequently published[82] in the Journal of the Optical Society of America.

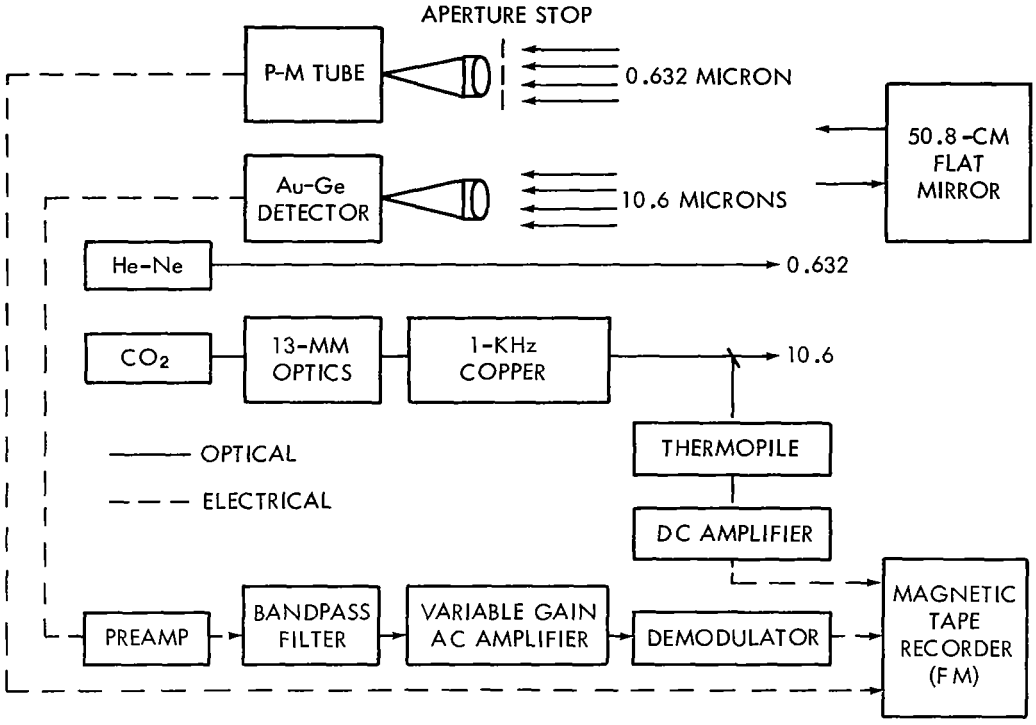

Figure 9. Experiment schematic diagram, dual-wavelength experiment.

was modulated at a 1-kHz rate to minimize the background and to enhance the detector operation. The 10.6-micron beam was transmitted through a 13-mm-aperture telescope which, because of the longer wavelength, also approximated a spherical-wave source. A small portion of the CO_2 beam was diverted and detected by a thermopile to monitor any fluctuations in output power.

A mirror in the field reflected the two beams, and they were then detected at the transmitter station by a photomultiplier and a gold-doped germanium detector. The output of the photomultiplier tube was recorded directly on an FM tape recorder. The 10.6-micron detected signal was demodulated by means of a standard envelope detection scheme and then recorded.

Table IX lists the important parameters of the experiment. In order to avoid the effects of aperture-averaging, each detector aperture was made to approximate a point detector. In addition, the photomultiplier tube aperture was adjusted so as to make the ratio of the apertures equal to the square root of the ratio of the wavelengths. This ensured that aperture-averaging effects were insignificant.

TABLE IX

System Parameters, Dual-Wavelength Experiment

Parameter	CO_2	He-Ne
Output power	2 W	1 mW
Beam divergence	0.4 mr	0.7 mr
Beam diameter	13 mm	1.4 mm
Detector aperture	2.5 cm	0.62 cm
Detector field of view	2°	5°
Detection signal bandwidth	220 Hz	2.5 kHz
Chopper frequency	1 kHz	
Range	1.2 km	1.2 km
Average beam height	4m	4m
Folding mirror diameter	50.8 cm	50.8 cm
Length of data run	10 sec	10 sec

The recorded scintillation data were replayed through an analog-to-digital converter into a Raytheon 520 digital computer that analyzed the statistics of the scintillation. The computer was programmed to analyze both irradiance and

log-amplitude statistics. Available statistics and functional relationships are given in Table X. The analog scintillation signal was sampled at a 1-kHz rate for 10 seconds, with each sample assigned to one of 500 discrete levels available in the computer. The selection of the time-record length for a single data run is a tradeoff between the statistical reliability of a measurement and the statistically time-varying atmosphere.

TABLE X

Computer Analysis, Dual-Wavelength Experiment

Irradiance Statistics	Log-Amplitude Statistics
Average value	Average value
Variance	Variance
Median	Median
3rd central moment	3rd central moment
4th central moment	4th central moment
Probability density function	Probability density function
	Cumulative distribution function
Power spectral density	
Autocorrelation function	

c. Results. Fig. 10 shows results of measurements taken over a 2-hour nighttime period in December. Plotted along the Y-axis is the parameter ψ, defined as the ratio of log-amplitude variances at 0.632 and 10.6 microns. The X-axis is the log-amplitude variance for the He-Ne beam ($\sigma\ell^2_{0.632}$) and the refractive index structure constant C_n^2, which in this case was determined from

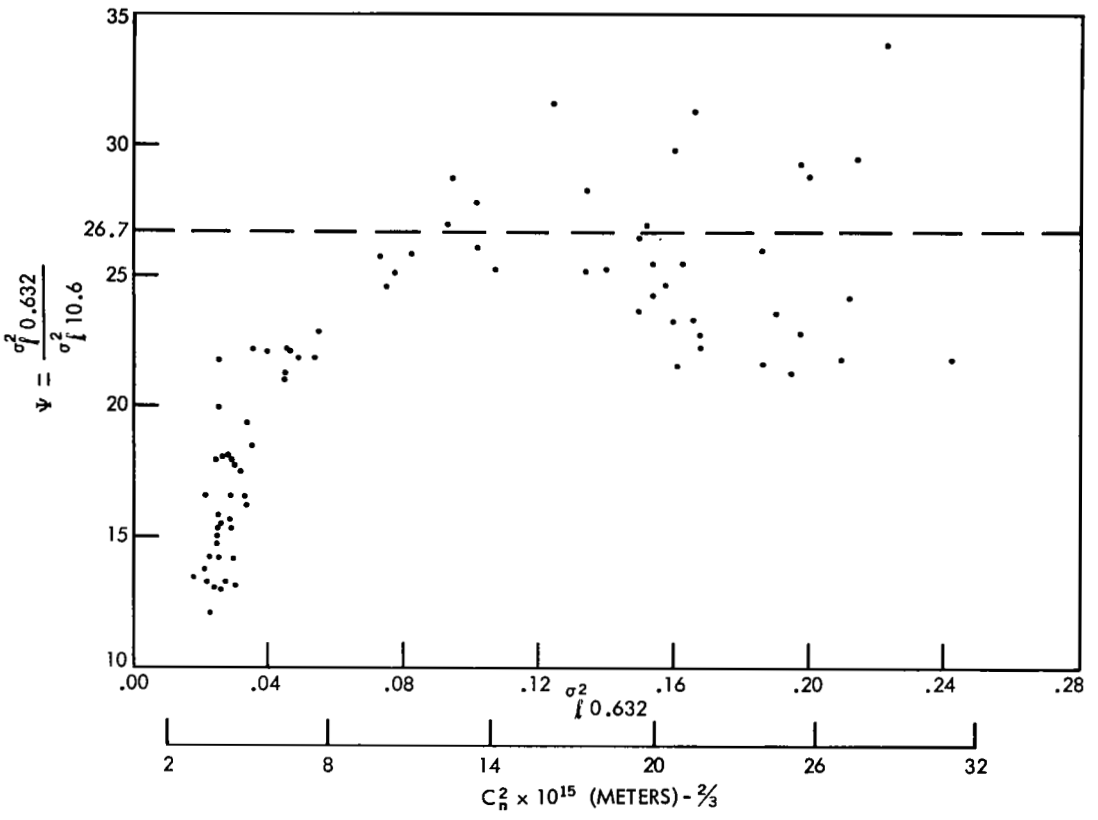

Figure 10. Ratio of log-amplitude variances for He-Ne and CO_2 wavelengths.

the equations for horizontal spherical-wave propagation. The value 26.7 is the theoretical ratio obtained from the 7/6 power predictions.

The data would seem to indicate that the scintillation statistics depart from the 7/6 power law in the region to the left. The difficulty here is that the region to the left corresponds to very low turbulence. The CO_2 laser output unfortunately had an appreciable amount of 120-Hz power supply ripple. In this region, the dominant noise on the 10.6-micron signal was caused not by the atmosphere but by the 120-Hz ripple. The output of the CO_2 unit was recorded on tape; an evaluation of the magnitude of the ripple showed that, in the 0.04 region, the

internal laser modulation became the same order of magnitude as the atmosphere-induced modulation. Therefore, the data points in the region below 0.07 are of questionable value. Some compensation for the CO_2 internal noise can be accomplished if one makes approximate assumptions.

The intensity at the detector aperture can be considered as the product of two random variables,

$$I(t) = I_L h(t) .$$

The first, I_L, is the irradiance fluctuation caused by internal laser ripple; the second, $h(t)$, is the time-varying atmospheric transmission. If both variables are assumed log-normal with respective variances σ_1^2 and σ_2^2, their product is also log-normal with a variance equal to $\sigma_1^2 + \sigma_2^2$.[83] Several experiments[70,84] have indicated that $h(t)$ is log-normal in the visible spectrum, and inspection of cumulative density of log amplitude for the transmitter noise (Fig. 11) has indicated normality as a reasonable approximation.

The data are shown replotted in Fig. 12 with the transmitter noise subtracted from the CO_2 statistics; the measurements obtained during low-scintillation conditions are neglected. The average value of the 39 independent data points shown is 26.8, and their variance is 10.8. The average value of ψ is in close agreement with the predicted value of 26.7.

The statistical reliability of the measurements has been analyzed to determine the magnitude of data scatter to be expected under ideal conditions.

Consider two target populations x and y where the random variable x and y are independent gaussian random variables. (Note that x and y represent the

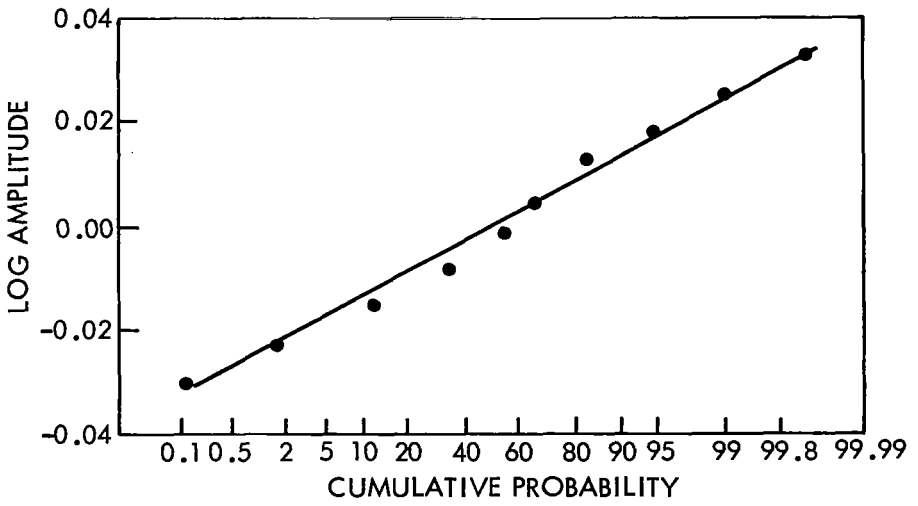

Figure 11. CO_2 transmitter noise; log-amplitude cumulative probability.

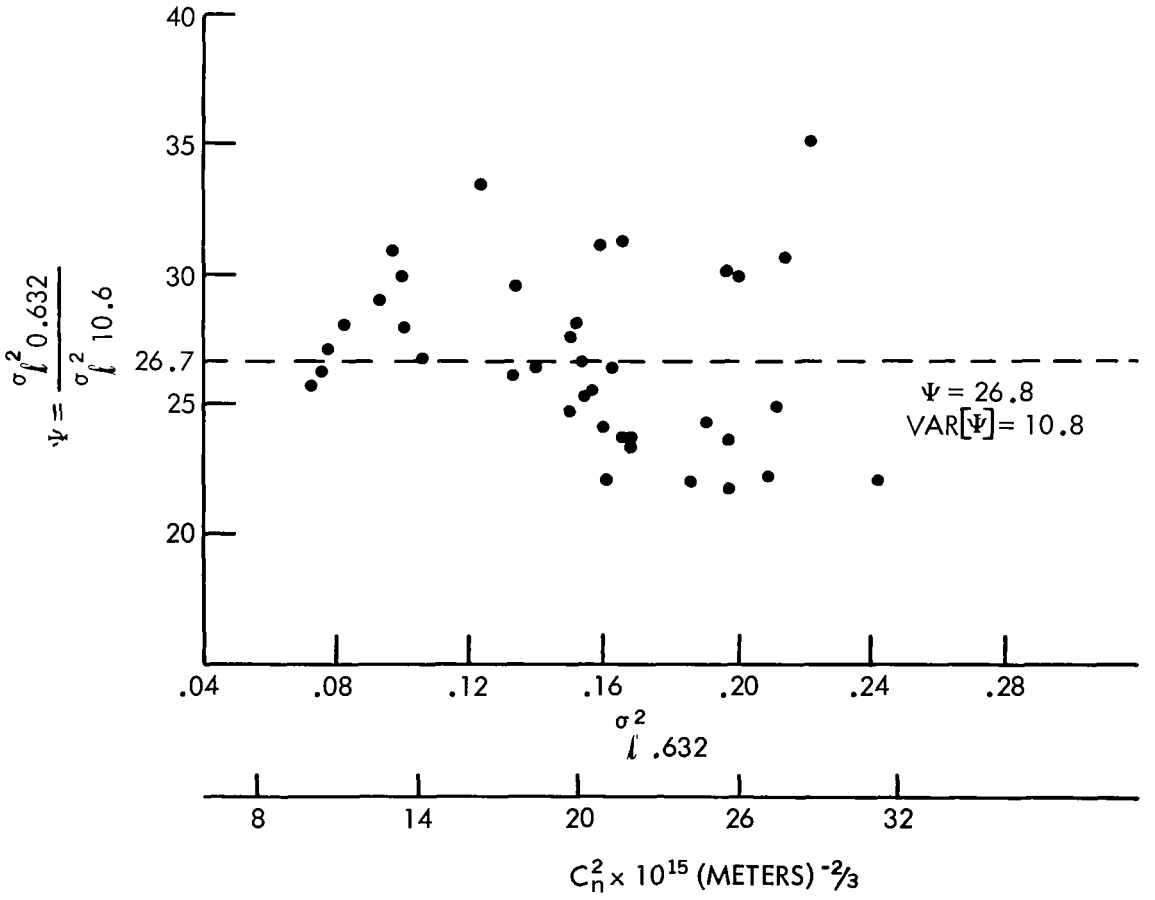

Figure 12. Ratio of log-amplitude variances for He-Ne and CO_2 wavelengths (transmitter noise removed, and all data $\sigma^2_{\ell\ 0.632}$ less than 0.07 neglected).

variable log amplitude at 0.632 and 10.6 microns; the assumption that they are independent is thus a very good approximation, as shown later in Fig. 32.) Let

$$\mathrm{VAR}(x) = \sigma_x^2$$

and (84)

$$\mathrm{VAR}(y) = \sigma_y^2 \ .$$

Select a random sample of size N from x and form the sample variance

$$S_x^2 = \frac{1}{N-1} \sum_{i=1}^{N} (x_i - \bar{x})^2 \ . \tag{85}$$

Since the x_i are normally distributed, then the random variable

$$\chi^2 = \frac{(N-1)\, S_x^2}{\sigma_x^2}$$

has the probability density function

$$P(\chi^2) = \frac{(\chi^2)^{N+1/2}}{2^{N-1/2}\, \Gamma\left(\frac{N-1}{2}\right)} \exp\left[-\chi^2/2\right] , \text{ for } \quad \chi^2 > 0 , \tag{86}$$

which is the chi-square density with N - 1 degrees of freedom. So, in this case,

$$\chi^2 = \chi^2_{N-1} \ .$$

Similarly, one can repeat the experiment with the y population and form the sample variance

$$S_y^2 = \frac{1}{M-1} \sum_{j=1}^{M} (y_i - \bar{y})^2 , \tag{87}$$

where the random sample is of size M. Note that the quantities N and M refer to the number of independent samples and not the total number of samples.

As before, $(M-1)\, S_y^2/\sigma_y^2$ is a chi-square random variable with $M-1$ degrees of freedom. Therefore,

$$\chi^2_{M-1} = \frac{(M-1)\, S_y^2}{\sigma_y^2} . \tag{88}$$

We now consider the normalized ratio of the sample variances, i.e.,

$$\frac{S_x^2/\sigma_x^2}{S_y^2/\sigma_y^2} \equiv F_{N-1,M-1} .$$

This quantity is a function of a random variable and is therefore itself a random variable. It is well known[85] that $F_{N-1,M-1}$ has the density

$$p\left(F_{N-1,M-1}\right) = \frac{\Gamma\left(\frac{N+M}{2}-1\right)\left(\frac{N-1}{M-1}\right)^{N-1/2}\left(F_{N-1,M-1}\right)^{N-3/2}}{\Gamma\left(\frac{N-1}{2}\right)\Gamma\left(\frac{M-1}{2}\right)\left[1+\left(\frac{N-1}{M-1}\right)F_{N-1,M-1}\right]^{N+M-2/2}} , \text{ for } F \geq 0 . \tag{89}$$

So, in order to construct a 90% confidence interval for a particular set of measurements, we write the probability statement

$$P\left[A < F_{N-1,M-1} < B\right] = 1 - \alpha = .90 , \tag{90}$$

where B can be determined directly from tables, once N and M are known. In order to find A, we use the relation

$$F_{N-1,M-1:1-\alpha/2} = \frac{1}{F_{M-1,N-1:\alpha/2}} . \tag{91}$$

Therefore,

$$P\left[\frac{1}{F_{M-1,N-1:\alpha/2}} < \frac{S_x^2 \sigma_y^2}{S_y^2 \sigma_x^2} < F_{N-1,M-1:\alpha/2}\right]$$

$$= P\left[\frac{S_x^2}{S_y^2 F_{N-1,M-1:\alpha/2}} < \frac{\sigma_x^2}{\sigma_y^2} < \frac{S_x^2 F_{M-1,N-1:\alpha'/2}}{S_y^2}\right] = 1 - \alpha = .90 . \tag{92}$$

For the sake of interest consider the following situation: Assume that a time record of length T has been analyzed for both the x and y target populations and that the evaluated ratio of the respective variances is 27, i.e.,

$$\frac{S_x^2}{S_y^2} = 27 .$$

In order to determine the degrees of freedom for S_x^2 and S_y^2, we inspect a typical autocorrelation function for each process (Fig. 14) and use a linear fit to the autocorrelation functions as well as the results of Appendix A; the number of independent samples N and M is then evaluated as

$$N = \alpha T \approx 120(10) = 1200, \text{for } S_x^2,$$

and (93)

$$N = \alpha T \approx 28.6(10) = 286, \text{for } S_y^2.$$

Therefore, from F-distribution tables (with linear interpolation) we get

$$P\left[\frac{27}{1.18} < \frac{\sigma_x^2}{\sigma_y^2} < 27(1.18)\right] = .90 . \tag{94}$$

Therefore,

$$P\left[22.9 < \frac{\sigma_x^2}{\sigma_y^2} < 31.8\right] = .90 .$$

---

*In a strict sense, the equivalent bandwidth used for finding N should be the bandwidth of the log-irradiance signal and not the bandwidth of the irradiance fluctuations. However, the data reduction system did not permit an evaluation of the sprectrum of log irradiance; therefore, the equivalent bandwidth of the irradiance signal was used. It is easy to show that the bandwidth of the irradiance signal is not seriously affected by the logarithmic operation under weak scintillation conditions (which is the situation at 10.6 microns, for most paths). Consider a system with input $x = v_0 = v(t)$ and output $y = A \log x$, where

v_0 = constant (dc level),

$v(t)$ = random time function with mean value equal to zero,

and

A = constant (gain of the log amplifier).

Power spectral density (psd) analysis of the input x is performed on v(t) only, since v_0 merely results in a delta function at the origin in the frequency domain. The output of the system is

$$y = A \log\left[v_0 + v(t)\right] = A \log\left(v_0\right)\left[1 + \frac{v(t)}{v_0}\right] = A \log\left(v_0\right) + A \log\left[1 + \frac{v(t)}{v_0}\right] .$$

Therefore, psd analysis of the output needs to be performed only on the second term, since A log $[v_0]$ is a constant. However,

$$\log(1 + x) \approx x, \text{ for } x << 1 ;$$

therefore,

$$\log\left[1 + \frac{v(t)}{v_0}\right] \approx \frac{v(t)}{v_0}$$

for $v(t) << v_0$ (i.e., weak scintillation). Thus, psd analysis of y is equivalent to psd analysis of $A\, v(t)/v_0$; this is the same as psd analysis of the input x, since the constant factors A, v_0 are removed by dividing through by the mean-square value.

The length of the confidence interval for the other data runs can be expected to be about the same, since T = 10 seconds for all cases. In addition, $B_{eq.}$* is determined chiefly by the component of wind velocity perpendicular to the propagation path, and this did not change significantly during the experiment. So we conclude that the observed data scatter is of the same order of magnitude as could be expected from statistical variation.

The normalized power spectral density for both wavelengths for a particular data run is shown in Fig. 13. These functions were evaluated by means of a

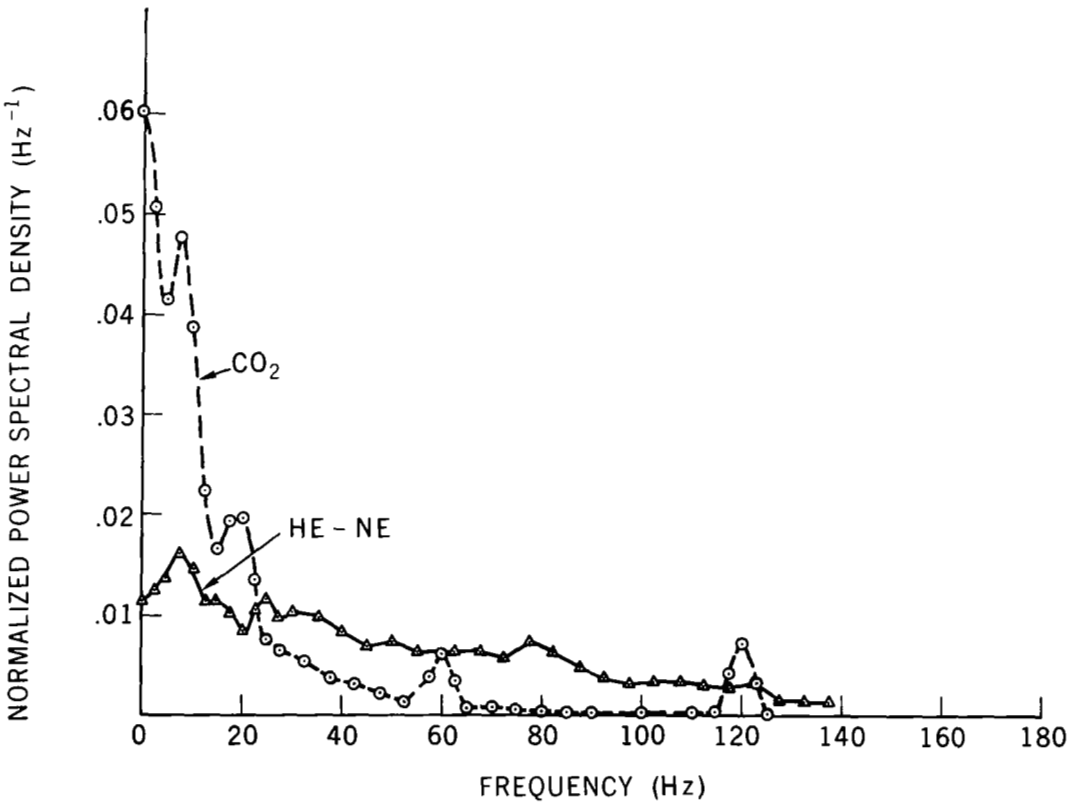

Figure 13. Dual-wavelength normalized power spectral density (resolution bandwidth = 5 Hz; each curve normalized to the same area; log-amplitude variances for these data are $\sigma_{\ell}^2{}_{0.632}$ = 0.200 and $\sigma_{\ell}^2{}_{10.6}$ = 0.00693).

Fourier transformation of their respective autocorrelation functions. Both curves are normalized by their intensity variances. Thus, if each wavelength has equal amounts of scintillation, this plot would indicate spectral distribution of the scintillation. The normalization scheme used requires the height of the CO_2 plot to be increased by a factor of 16. Therefore, it should be clear that, at any frequency, there is far more scintillation in the visible spectrum than at 10 microns. The resolution bandwidth is 5 Hz, and the wind velocity perpendicular to the propagation path is approximately 1.5 meters per second. The power supply ripple on the 10-micron beam is obvious in this plot.

Fig. 14 presents the same data in the time domain in terms of the normalized autocorrelation function $R_x(\tau)/R_x(0)$. Again, the internal modulation of the CO_2 laser appears as peaks at 8- and 16-millisecond intervals. If one fits an exponential function of the form $e^{-\alpha\tau}$ to each of these curves, the correlation time constants (the alphas) have a ratio of 4.4, which is close to the ratio of the square roots of the wavelengths. This is in agreement with propagation theory, as can be seen from the following argument. Tatarski has shown that the covariance of log amplitude $C_\chi(\rho)$ falls off to zero for separations on the order of $\sqrt{\lambda z}$. Also, it is shown analytically in this report and experimentally by others[2] that the irradiance covariance function $C_I(\rho)$ has a similar characteristic. So, $C_I(\rho) \approx 0$ at $\rho = \sqrt{\lambda z}$. Assuming that the relationship between the spatial dependence and the time dependence of the covariance functions is predicted by the concept of "frozen-in turbulence," then $\rho = V_n \tau$, where V_n is the component of wind velocity perpendicular to the propagation path; therefore,

$$C_I(\tau) \approx 0 \qquad \text{at} \qquad \tau \approx \frac{\rho}{V_n} = \frac{\sqrt{\lambda z}}{V_n} .$$

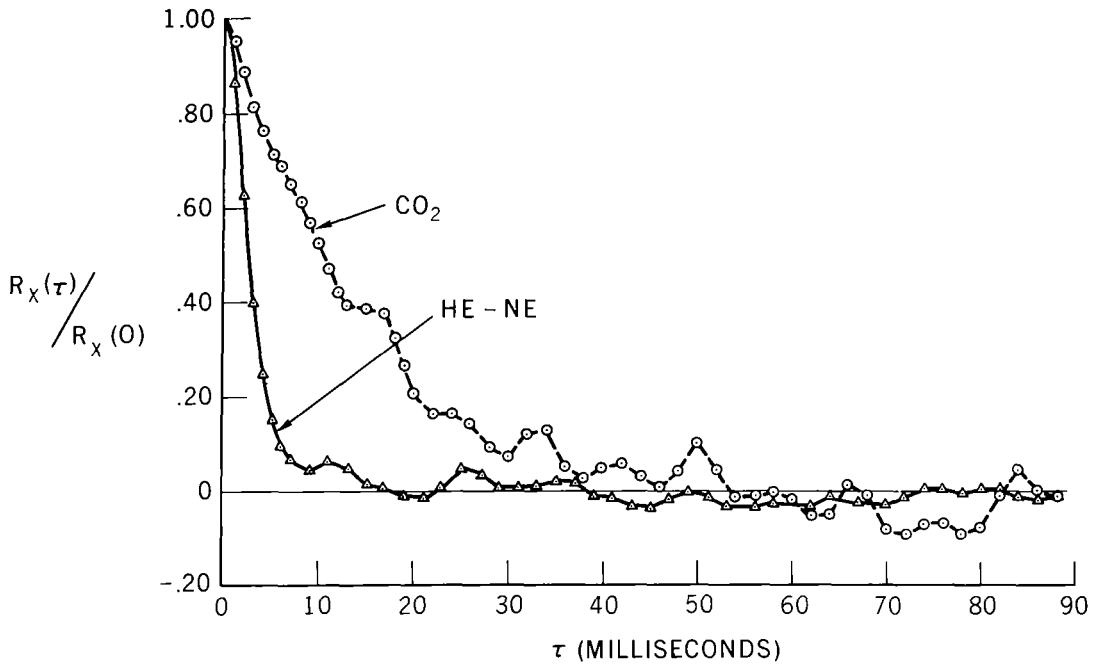

Figure 14. Normalized autocorrelation function for dual-wavelength scintillation; fitting the data with the exponential $e^{-\alpha\tau}$ gives $\alpha\,(CO_2) = 71.4$, α(He-Ne) = 312.

So, if we inspect $C_I(\tau)$ for two different wavelengths, we expect the ratio of the correlation times to be proportional to $(\lambda_1/\lambda_2)^{1/2}$.

A typical portion of the analog scintillation signal is shown in Fig. 15. The computer evaluated the variances as 0.200 and 0.00668, which gives a ψ value of 30. The chart recorder had a 110-Hz, 3-db bandwidth, which tends to smooth some of the high-frequency He-Ne scintillation (very little CO_2 scintillation is in the 110-Hz region). The important parameter is the ratio of the maximum and minimum signal excursions from the average value. For the He-Ne scintillation, excursions of several octaves are common. In both of these traces, the background levels were not significantly different from the zero level.

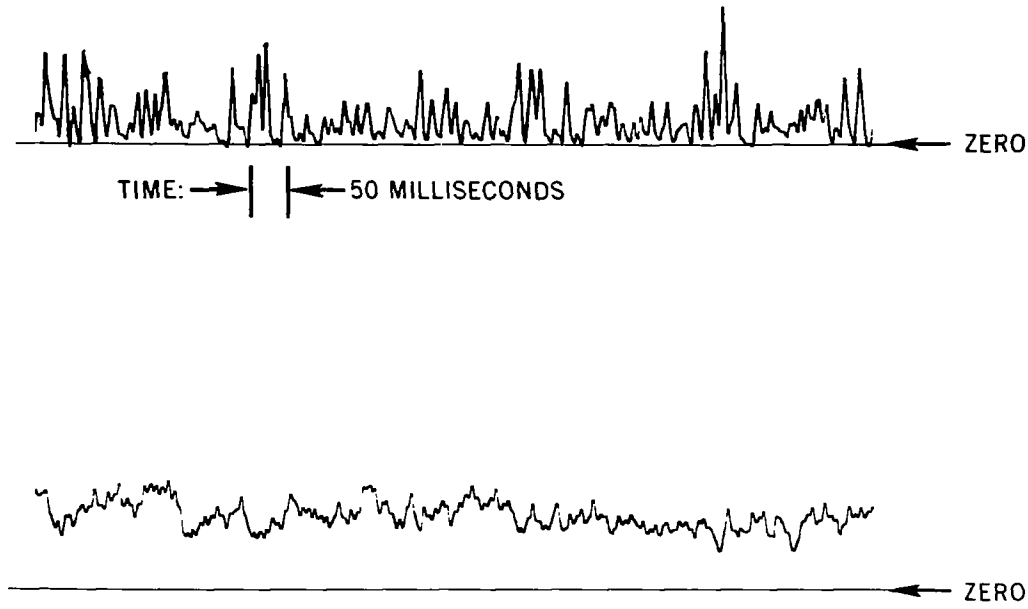

Figure 15. Typical analog scintillation signal; log-amplitude variances are 0.200 for He-Ne and 0.00668 for CO_2.

Fig. 16 is a typical cumulative probability plot of log amplitude at 10.6 microns on Gaussian probability paper. The abscissa is $F(\ell)$, where

$$F(\ell) = \int_{-\infty}^{\ell} f(u)\,du ,$$

and $f(u)$ is the probability density function for log amplitude; the ordinate is log amplitude. The abscissa scale is constructed so that a normal random variable would plot as a straight line. Thus it is clear that the statistics of scintillation at 10.6 microns satisfy this test for log-normality.

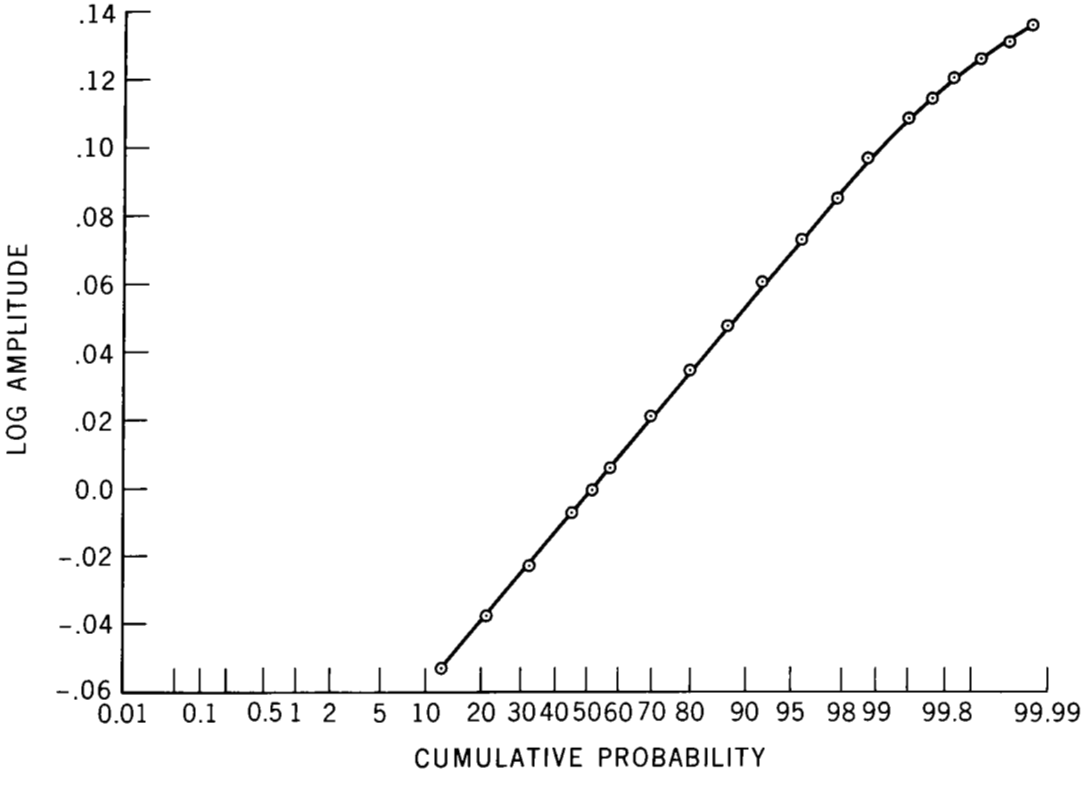

Figure 16. Cumulative probability of log amplitude at 10.6 microns; data plotted on a Gaussian abscissa scale.

d. Conclusions. In summary, the following conclusions can be made:

(1) The average value for the log-amplitude variance ratio at 10.6 and 0.632 microns is very close to the predicted value of 26.7.

(2) The C O_2 scintillation has a bandwidth that is several times less than for the He-Ne and a correlation time that is approximately 4.4 times greater than for the He-Ne.

(3) The probability distribution of scintillation at 10.6 microns is approximately linear when plotted on log-normal probability paper and thereby satisfies this test for log-normality.

2.3 Measurement of Log-Amplitude Variance and the Saturation Level of Irradiance Fluctuations*

a. Measurement of Log-Amplitude Variance. Theoretical expressions for the variance of log amplitude (σ_ℓ^2) have been derived for several types of propagation paths.[2,70,78] Numerous experiments have been devised to check the theory and have resulted in several techniques for the experimental evaluation of σ_ℓ^2. The first part of this section is concerned with numerical differences in σ_ℓ^2 which we have noted in our work when two different techniques were applied to the same raw data.

It has been shown[86] that for log-normal scintillation, irradiance and log-amplitude variances are related through

$$\frac{\sigma_I^2}{I_0^2} = \exp\left[4\sigma_\ell^2\right] - 1, \tag{95}$$

where σ_I^2 = irradiance variance. Since irradiance fluctuations are easily measured, several experimenters[2,84,87] have used Eq. 95 to evaluate σ_ℓ^2. Another technique is to simply normalize a group of quantized irradiance samples (I_1, $I_2, \cdots I_n$) by I_0 and form ($\ell_1, \ell_2, \cdots \ell_n$), where

$$\ell_i = \frac{1}{2} \ln \frac{I_i}{I_0}, \text{ for } i = 1, 2, \ldots, n \ .$$

*A portion of the work reported in this section was published in the Journal of the Optical Society of America.[88]

A histogram (i.e., probability density function) can then be constructed and the moments of log amplitude computed.

Both of these techniques were used on scintillation measurements with a He-Ne laser (0.632 microns) over a 1.17-km horizontal path. The laser output was 1.4 mm between $1/e^2$ points in the irradiance profile and had a divergence of 0.7 mr. At the receiver, the fluctuating signal was detected by a photomultiplier through a 3-mm aperture. The results are shown in Fig. 17, where σ_T^2 is the log-amplitude variance based on irradiance measurements and Eq. 95, and σ_E^2 is the log-amplitude variance evaluated from the moments of log amplitude.

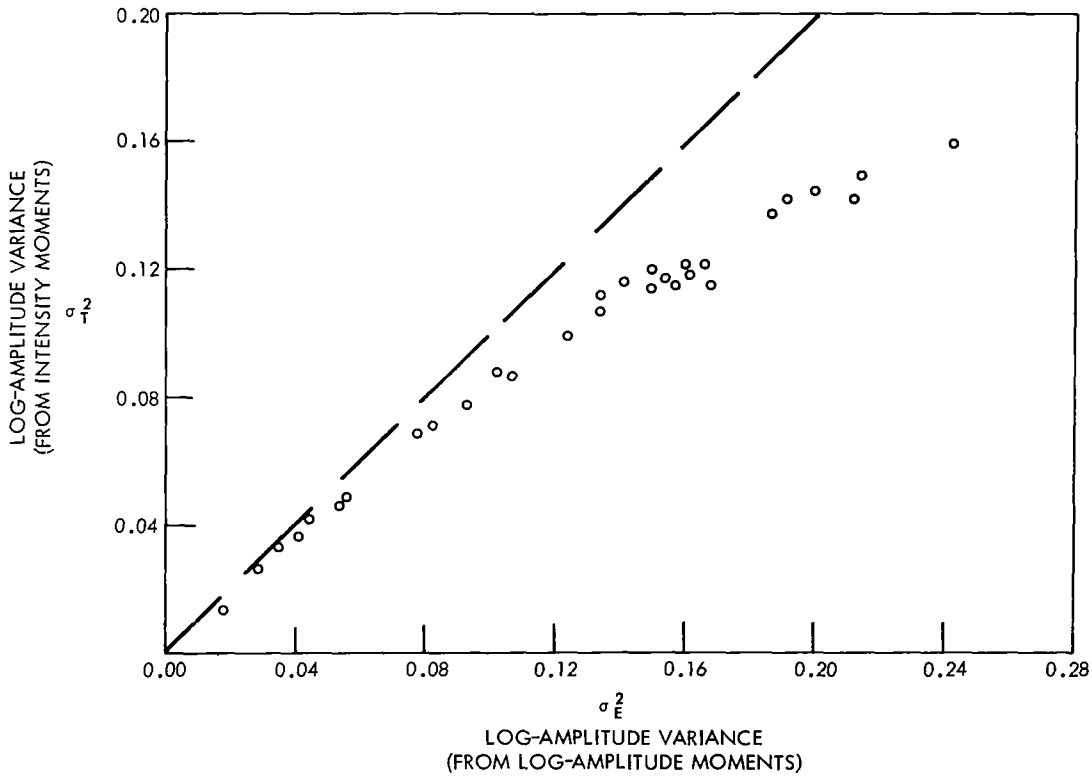

Figure 17. Comparison of log-amplitude variance: σ_T^2 calculated from irradiance moments [Eq. (95)] and σ_E^2 calculated from log-amplitude moments.

Ideally, either technique should give the same result and all points should lie on the unity-slope straight line in Fig. 17. However, as the scintillation becomes stronger, the difference $(\sigma_E^2 - \sigma_T^2)$ becomes significantly greater. Therefore, the discussion must center on which of the two techniques for $\sigma_E^2 - \sigma_T^2$ evaluation is more valid.

Objections to the use of moments to evaluate σ_E^2 are based primarily on the dynamic range and frequency response limitations of the instrumentation. In this experiment the average photomultiplier current was approximately a microampere and the signal-to-noise ratio was sufficiently high so that dynamic range constraints were not excessive.* Power spectral density analysis of the data indicates that the frequency response of the system (2.5 kHz) was also not a problem.

Since σ_T^2 is based on the Gaussian behavior of log amplitude (through Eq. 95), it would seem reasonable to try to correlate $(\sigma_E^2 - \sigma_T^2)$ with deviations from normality. Fig. 18 plots percent deviation versus skewness S, where $S = m_3/(m_2)^{3/2}$ and m_i is the ith moment of log amplitude about the mean. For a symmetrical distribution such as the normal, S should vanish. Fig. 18 is shown with a least-square linear fit.

The data indicates that for scintillation with $|S| > 1$, the error in calculating log-amplitude variance through Eq. 95 becomes significant. If Fig. 17 is extrapolated to stronger turbulent conditions, one gets a saturation-like effect which is similar to that noted by Gracheva and Gurvich,[84] and Dietz.[89] This is

*See Appendix C.

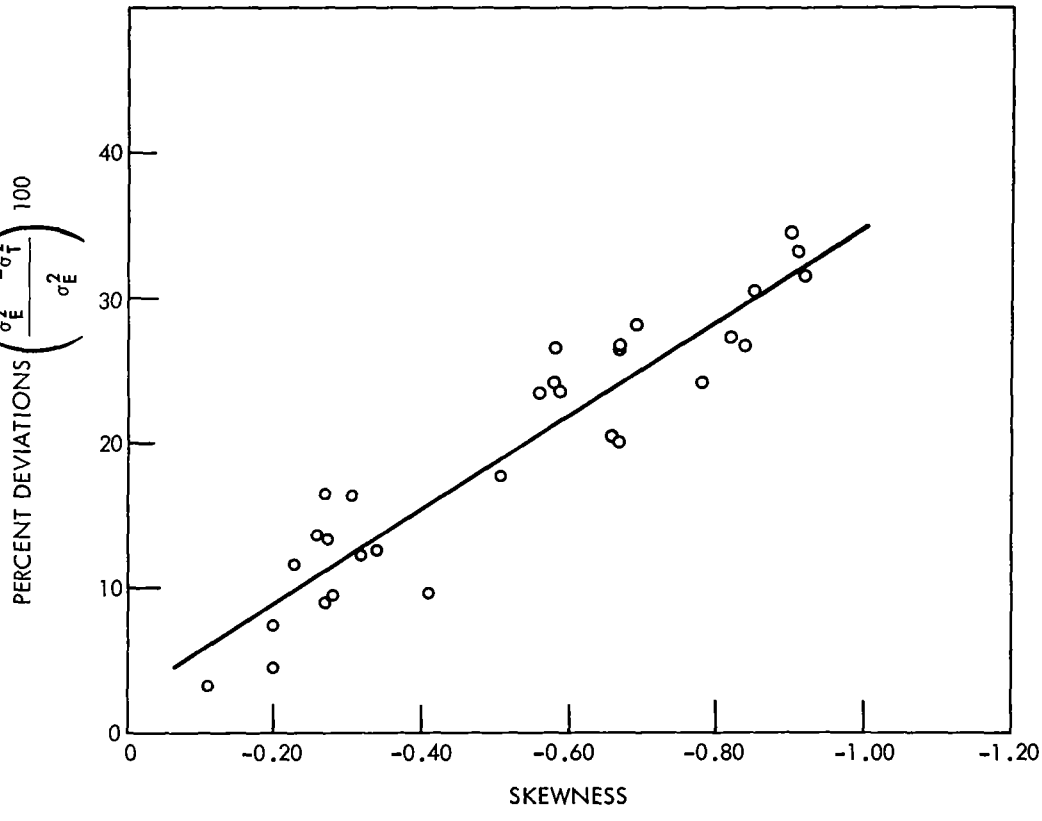

Figure 18. Percent deviation of log-amplitude variance measurements vs skewness of log amplitude.

particularly interesting since Eq. 95 was used to evaluate log-amplitude variance in References 91 and 95. Fig. 19 presents the difference $\sigma_E^2 - \sigma_T^2$ as a function of the third central moment. As pointed out by Hufnagel,[90] $\sigma_E^2 - \sigma_T^2 = 2m_3$ + higher-order terms.

This relationship seems to be in fairly good agreement with the data. It is noteworthy that cumulative probability plots of log amplitude for various S values do not appear significantly different on Gaussian probability paper. Fig. 20 presents results for typical data with S ranging from -0.143 to -0.694.

Concluding this section, it appears that the validity of Eq. 95 is extremely sensitive to deviations from log normality and, in most interesting experiments, its accuracy is very dubious.

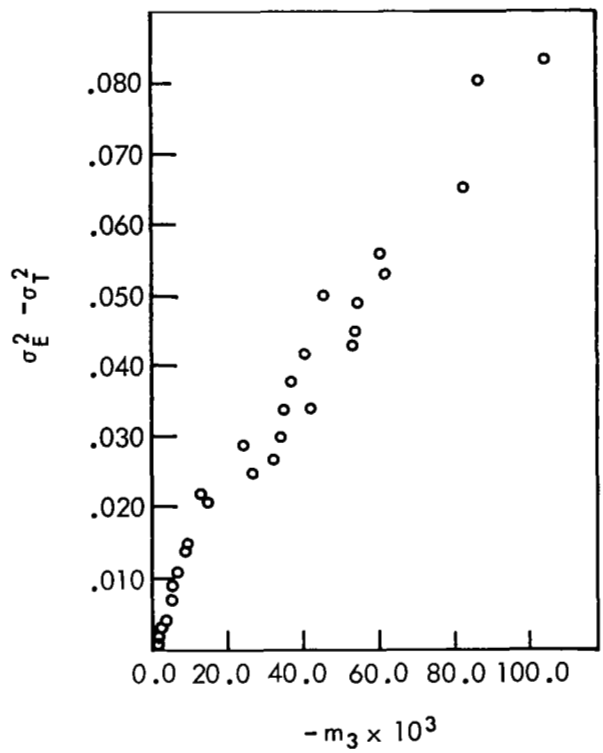

Figure 19. Difference $\sigma_E^2 - \sigma_T^2$ as a function of third central moment, m_3.

b. Saturation Level of Irradiance Fluctuations. In order to give more insight into the implications of Fig. 17, more data were recorded over the same range during strong turbulence conditions. An argon laser radiating at 4880Å was used. The output beam had a diameter of 1.2 mm between $1/e^2$ points and a divergence of 0.7 mr. The received energy was measured by a photomultiplier through a 1.5-mm aperture.

The results are shown in Fig. 21, where the circled points represent the argon data and the solid points are the He-Ne measurements already presented in Fig. 17. It is clear that σ_T^2 fails to increase much beyond 0.3, regardless of how large σ_E^2 becomes. At the time of this writing, there have been five

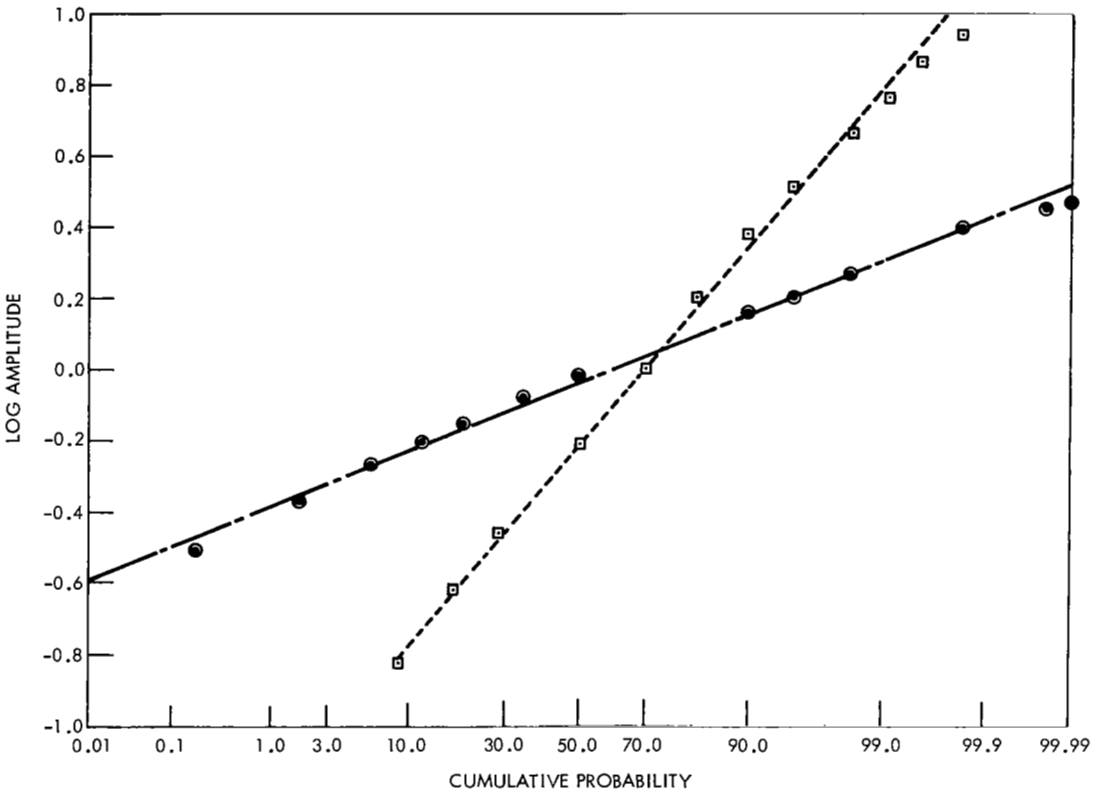

Legend	Log-amplitude variance	Skewness
—— - ——	0.0215	-0.143
- - - - - - -	0.226	-0.694.

Figure 20. Cumulative probability of log amplitude

experimental efforts known to the author directed toward measuring the saturation level for irradiance fluctuations at visible wavelengths. The net result seems to be that there is complete agreement that saturation occurs but very little agreement as to the actual level at which this happens.

The work of Gracheva and Gurvich[84] in the Soviet Union produced the first experimental evidence of the saturation of log-amplitude variance. The saturation level was measured as approximately 0.58. However, as pointed out by deWolf,[65] there was an error in the data reduction, and the actual measured value was 0.14.

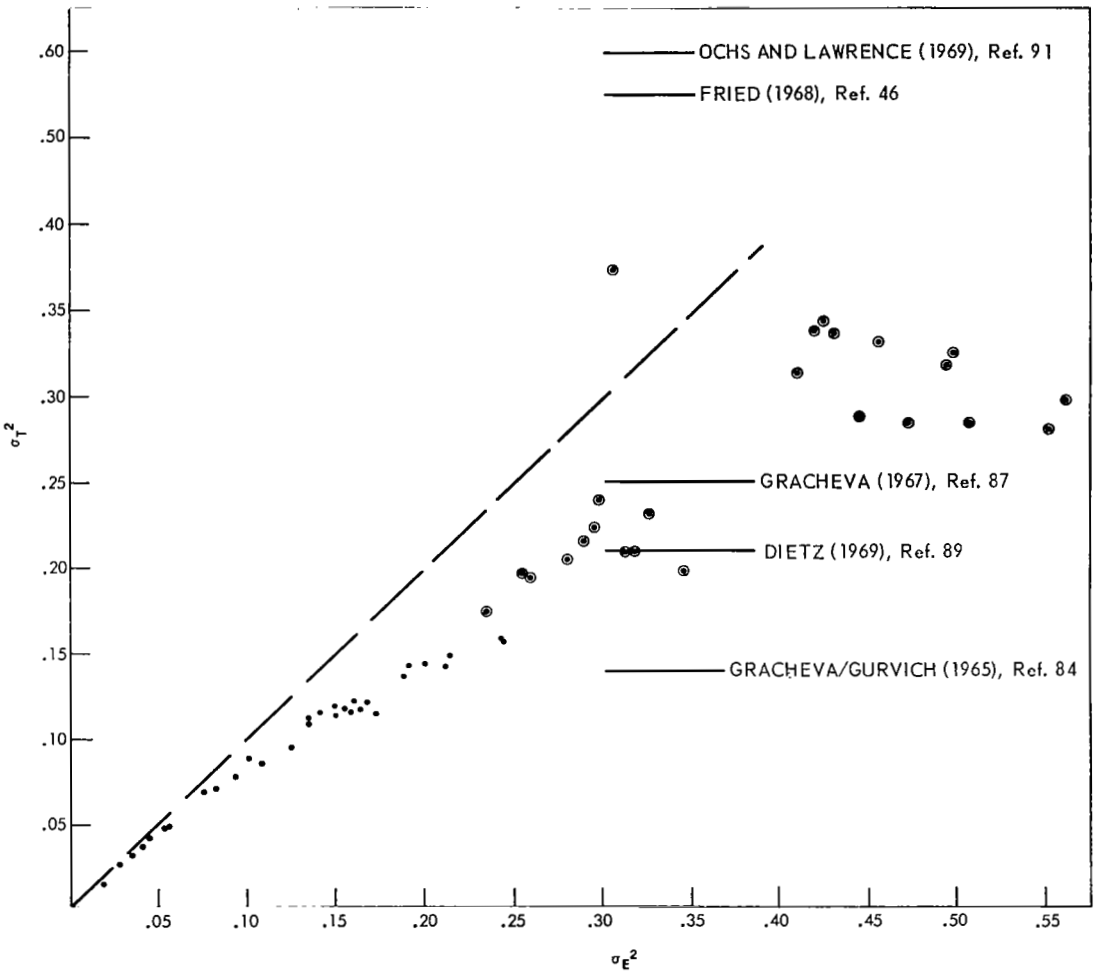

Figure 21. Comparison of log-amplitude variance: σ_T^2 calculated from irradiance moments [Eq. 95] and σ_E^2 calculated from log-amplitude moments. The circled data points represent argon data, and the solid points are He-Ne measurements. The five levels shown are the saturation levels measured in five different experiments.

Following this, additional data were published by Gracheva[87] and the saturation level was observed to be 0.25. In the United States, Ochs and Lawrence[91] published data indicating saturation at about 0.6. Two data-processing techniques were used; the first measured the slope of the cumulative density of log amplitude; the second was entirely analog and used logarithmic amplifiers and RMS

voltmeters; the techniques gave similar results. Unfortunately, the authors concluded that their data were in agreement with those of Gracheva and Gurvich. Apparently they had not noted deWolf's correction to these data, although it had been published nine months earlier. Later, using photographic techniques, Dietz[89] measured saturation at about 0.21. In this case, as well as in Ref. 84, the variance of log-amplitude was computed by measuring irradiance statistics and transforming to log amplitude statistics using Eq. 95. The remaining experimental effort was conducted by Fried[46] who observed saturation for both visible and infrared fluctuations, and in addition noted that the saturation level was wavelength-dependent. The analysis technique based on the slope of the cumulative probability function was used here and resulted in a saturation level in the visible of 0.55. Since the experimental conditions in each of the listed instances were approximately the same, it seems likely that only Fried and Lawrence and Ochs have really measured saturation. The saturation observed in the other experiments appears to be either a "statistical saturation" (i.e., the use of Eq. 95) or perhaps an effect due to dynamic range limitations.* Dietz[89] remarks that when his data were analyzed with the cumulative probability technique (which is less dependent on dynamic range), the values for log-amplitude variance became "somewhat

*In addition to the published experimental efforts, there is a widely-quoted summarization of contemporary propagation work by Strohbehn[45] which has also contributed to the confusion. The saturation level is discussed and the factor of two error in the Gracheva/Gurvich data is noted. The data of Gracheva are presented; through a succession of notation errors, missing factors of two and interchanging of variances (χ^2) with standard deviations ($\sigma_1^2 = 4\sigma_\chi^2 = \langle \chi^2 \rangle$), Strohbehn concludes that the saturation level is approximately 0.8 (p. 1307). It appears to this writer that the calculation should be $\sigma_\chi^2 = (0.8/2)^2 = 0.16$.

higher," but not enough information is given so that meaningful comparisons can be made.

In addition, there are some fundamental problems associated with the use of pulsed sources and photographic techniques such as those used in Ref. 89. Often the output of such sources is spatially quite non-homogeneous, and, as a result, the measured spatial probability density function of log amplitude is the convolution of two densities: the output density associated with the source and the density associated with the atmospheric-induced fluctuations. In fact, the source characteristics may mask the atmospheric-caused fluctuation for ranges up to 200 meters.[89] Other obvious problem areas include compensating for the nonlinear transfer functions of the film and overcoming the severe dynamic-range problem. Judged by the noticeable nonlinearity of the cumulative probability plots of log amplitude presented in Ref. 89, as well as in other reports[92-94] by the same group of experimenters, it does not appear that the combination of pulsed sources and photographic detection techniques permits accurate measurement of the density function of irradiance fluctuations.

The difference $\sigma_E^2 - \sigma_T^2$ for the high-turbulence argon data presented in Fig. 21 is superimposed on the original He-Ne data and presented in Fig. 22 as a function of m_3. The data appear to be in approximate agreement with theory.

We conclude that much of the data on the saturation of the variance of log amplitude are suspect.* The level at which saturation occurs appears

*The absolute accuracy of the very high-turbulence argon data (i.e. $\sigma_E^2 > 0.3$) presented in Figs. 21 and 22 must be estimated with caution, because of the extended instrumental dynamic range required for such measurements (see Appendix C). However, the conclusions presented are not affected even if all data points with $\sigma_E^2 > 0.3$ are deleted.

to be considerably greater than the 0.2 value first reported in the literature.[84,87]

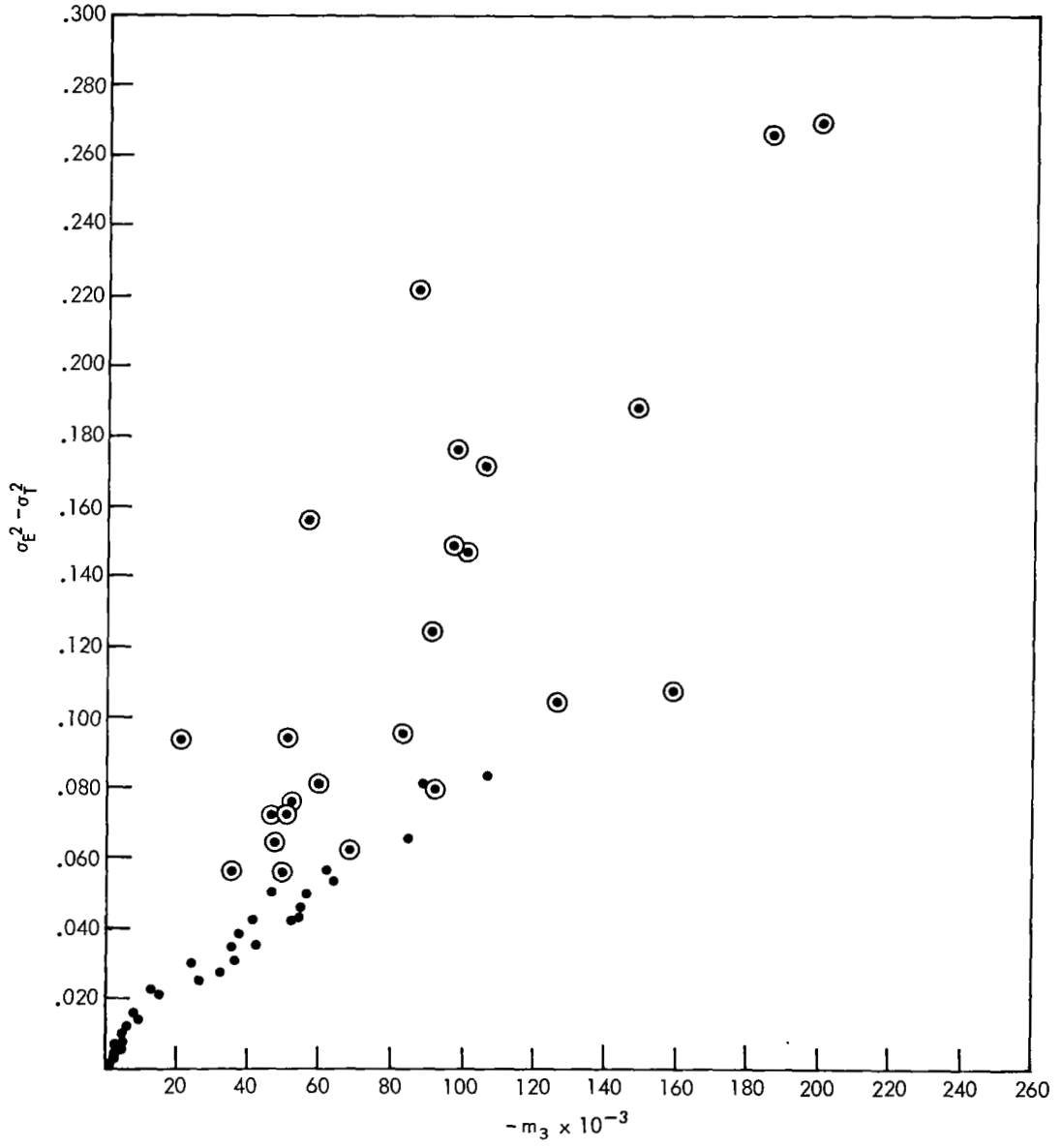

Figure 22. Difference $\sigma_E^2 - \sigma_T^2$ as a function of the third central moment, m_3. The circled data points represent argon data, and the solid points are He-Ne measurements.

2.4 Spatial and Spectral Correlation of Irradiance Fluctuations

This section presents the results of an experimental investigation of certain second-order statistics of the amplitude field. Specifically, we consider the two-point statistic (spatial correlation) and the two-wavelength statistic (spectral correlation). Part (a) deals with spatial correlation, and Part (b) deals with spectral correlation.

a. Spatial Correlation: Theory. We consider an electromagnetic wave which propagates through a medium characterized by zero conductivity, constant permeability, and a permittivity which is a random-point function. A degree of randomness is imposed on the amplitude and phase of the wave by the stochastic nature of the medium. The log-amplitude covariance for the wave as measured at points $\bar{X}$ and $\bar{X}_2$ is

$$C_\ell(\bar{X}_1, \bar{X}_2) = \left\langle \left\{ \ell(\bar{X}_1) - \langle \ell(\bar{X}_1) \rangle \right\} \left\{ \ell(\bar{X}_2) - \langle \ell(\bar{X}_2) \rangle \right\} \right\rangle, \qquad (96)$$

where $\ell(\bar{X})$ is the log-amplitude value measured at $\bar{X}$, and the angle brackets denote an ensemble average over all the possible realizations of the permittivity field. When the electromagnetic field quantities are assumed to be locally homogeneous and isotropic, Eq. 96 becomes

$$C_\ell(\rho) = \left\langle \left\{ \ell(\bar{X}_1) - \langle \ell(\bar{X}_1) \rangle \right\} \left\{ \ell(\bar{X}_1 + \rho) - \langle \ell(\bar{X} + \rho) \rangle \right\} \right\rangle, \qquad (97)$$

where

$$\rho = |\bar{X}_1 - \bar{X}_2| \ .$$

Tatarski[95] has evaluated $C_\ell(\rho)$ for infinite plane-wave propagation through homogeneous isotropic turbulence, and Fried[96] has solved the spherical-wave case for similar turbulence conditions. Unfortunately, direct experimental testing of these results is difficult; existing optical detectors are square-law devices and, therefore, have outputs which are proportional to the square of the electric field rather than the logarithm of the field. High-speed logarithmic processors with sufficient accuracy, moreover, are difficult to obtain and have, up to this time, limited the accuracy with which theoretical-experimental comparisons can be made. It is possible, however, to transform the results for log-amplitude covariance into irradiance covariance. This permits more direct comparisons of experiment with theory.

The starting point is the covariance of irradiance $C_I(\rho)$, defined as

$$C_I(\rho) = \left\langle \left\{ I(\bar{X}_1) - I_0(\bar{X}_1) \right\} \left\{ I(\bar{X}_2) - I_0(\bar{X}_2) \right\} \right\rangle , \tag{98}$$

where

$$I_0(\bar{X}_1) = \langle I(\bar{X}_1) \rangle ,$$

$$I_0(\bar{X}_2) = \langle I(\bar{X}_2) \rangle ,$$

$$\rho = |\bar{X}_1 - \bar{X}_2| ,$$

and the assumptions of homogeneity and isotropy have been incorporated in Eq. 98. From the definition of log amplitude $\ell(\bar{X})$, we obtain

$$I(\bar{X}) = I_0(X) \exp\left[2\ell(\bar{X})\right] . \tag{99}$$

We assume statistical homogeneity in the plane of the detectors $\left(I_0(\bar{X}_1) = I_0(\bar{X}_2) \equiv I_0\right)$ and Gaussian statistics for log amplitude. Then,

$$C_I(\rho) = I_0^2 \left\langle \left\{ \exp\left[2\ell(\bar{X}_1)\right] - 1 \right\} \left\{ \exp\left[2\ell(\bar{X}_2)\right] - 1 \right\} \right\rangle$$

$$= I_0^2 \left\langle \exp\left[2\ell(\bar{X}_1) + 2\ell(\bar{X}_2)\right] - \exp\left[2\ell(\bar{X}_2)\right] - \exp\left[2\ell(\bar{X}_1)\right] + 1 \right\rangle \quad \cdot \quad (100)$$

The moment-generating function with parameters t_1, t_2 for the bivariate normal distribution with random variables α_1, α_2 is

$$m(t_1, t_2) \equiv \left\langle \exp\left[t_1 \alpha_1 + t_2 \alpha_2\right] \right\rangle$$

$$= \exp\left[t_1 \mu_1 + t_2 \mu_2 + \frac{1}{2} \left(t_1^2 \sigma_1^2 + 2r t_1 t_2 \sigma_1 \sigma_2 + t_2^2 \sigma_2^2 \right) \right], \quad (101)$$

where

$$\langle \alpha_1 \rangle = \mu_1 ,$$

$$\left\langle (\alpha_1 - \mu_1)^2 \right\rangle = \sigma_1^2 ,$$

$$\langle \alpha_2 \rangle = \mu_2 ,$$

$$\left\langle (\alpha_2 - \mu_2)^2 \right\rangle = \sigma_2^2 ,$$

and

$$r = \frac{\left\langle (\alpha_1 - \mu_1)(\alpha_2 - \mu_2) \right\rangle}{\sigma_1 \sigma_2} \quad .$$

Therefore, the first term of Eq. 100 is the bivariate normal moment-generating function (m.g.f.) evaluated at $t_1 = t_2 = 2$, while the second and third are the m.g.f. for the corresponding marginal density functions. Using Eq. 99 and noting that[86]

$$\langle I(X) \rangle = I_0(X) = \langle I_0(X) \exp\left[2\ell(X)\right] \rangle \tag{102}$$

implies that

$$\langle \exp\left[2\ell(X)\right] \rangle = 1$$

and

$$\langle \ell(X) \rangle = -\left\langle \left[\ell(X) - \langle \ell(X) \rangle\right]^2 \right\rangle . \tag{103}$$

Then, we obtain

$$C_I(\rho) = I_0^2 \left\{ \exp\left[2\mu_1 + 2\mu_2 + 2\left(\sigma_1^2 + 2C_\ell(\rho) + \sigma_2^2\right)\right] - 1 \right\}$$

$$= I_0^2 \left\{ \exp\left[4C_\ell(\rho)\right] - 1 \right\} , \tag{104}$$

where $C_\ell(\rho)$ is the covariance function for log amplitude, and the μ and σ^2 symbols are respectively log-amplitude means and variances at $\bar{X}_1$ and $\bar{X}_2$. The irradiance correlation coefficient γ at separation ρ is

$$\gamma(\rho) = \frac{C_I(\rho)}{C_I(0)} = \frac{\exp\left[4C_\ell(\rho)\right] - 1}{\exp\left[4C_\ell(0)\right] - 1} , \tag{105}$$

and we define the log-amplitude correlation coefficient $F(\rho)$ through

$$C_\chi(\rho)/C_\chi(0) = F(\rho) \quad . \tag{106}$$

Therefore,

$$\gamma(\rho) = \frac{\exp\left[4C_\chi(0)\,F(\rho)\right] - 1}{\exp\left[4C_\chi(0)\right] - 1} \quad . \tag{107}$$

It is clear that $\gamma(\rho)$ depends upon $F(\rho)$ and also on the strength of turbulence through the scintillation statistic $C_\chi(0)$. Expanding the numerator and denominator of Eq. 107 in a Maclaurin series reveals clearly that in the limiting case, as the turbulence becomes very weak, the normalized log-amplitude and irradiance correlation coefficients become equal. This is intuitively satisfying, since for weakly fluctuating phenomena the logarithmic operator approaches linearity.

Tatarski[95] presents $F(\rho)$ (Fig. 7-13) for plane-wave propagation through homogeneous and isotropic turbulence, and Fried derives a similar result for the spherical-wave case in Fig. 1, Ref. 96. We can now transform from log-amplitude correlation coefficient to irradiance correlation coefficient through Eq. 107 for any specified degree of turbulence [i.e. any value of $C_\chi(0)$]. This has been carried out in Fig. 23 and Fig. 24 for the plane-wave and the spherical-wave case, respectively, and with log-amplitude variance values of 0.076 and 0.460. These particular values were chosen to correspond with the experimental data, and, in addition, the 0.460 value is on the order of the upper limit of Rytov theory. The detector separation has been normalized by $(\lambda z)^{1/2}$, where λ is the optical wavelength and z is the propagation path length.

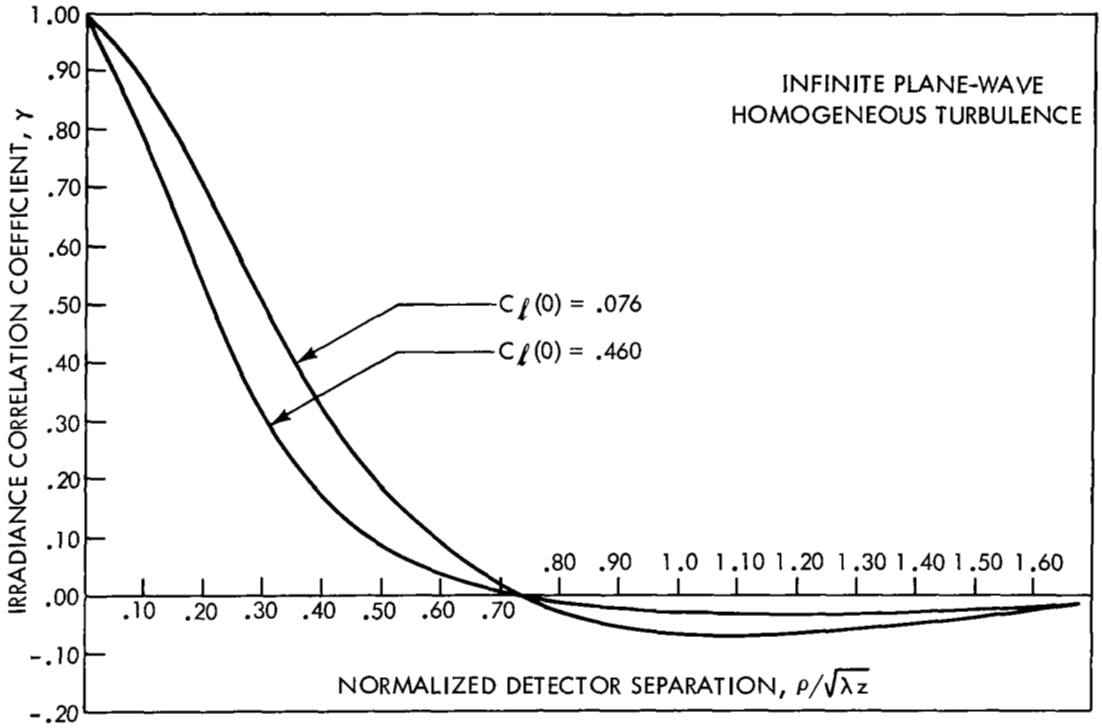

Figure 23. Irradiance correlation coefficient γ as a function of normalized detector separation $\rho/(\lambda z)^{1/2}$. The curves are obtained from Tatarski's[2] results for the plane-wave log-amplitude correlation coefficient.

Experiment. The system for measuring spatial correlation is shown schematically in Fig. 25. A vertically polarized argon laser beam radiating at 4880 Å with a divergence of 0.7 mr and a diameter of 1.2 mm was transmitted over a folded 1.17-km horizontal path. After reflection from a 51-cm flat mirror in the field, the beam was detected back at the transmitter station by two photomultiplier tubes which had 1-mm entrance pupils and which were spaced from 2 to 52 mm apart. The outputs of the detectors were amplified and then recorded on magnetic tape through an FM system with 2.5-kHz bandwidth. For each detector separation, approximately two minutes of data were taken.

Analysis of two-point statistics is complicated by the fact that each detector (and subsequent electronic chain) may have different scale factors. However, if

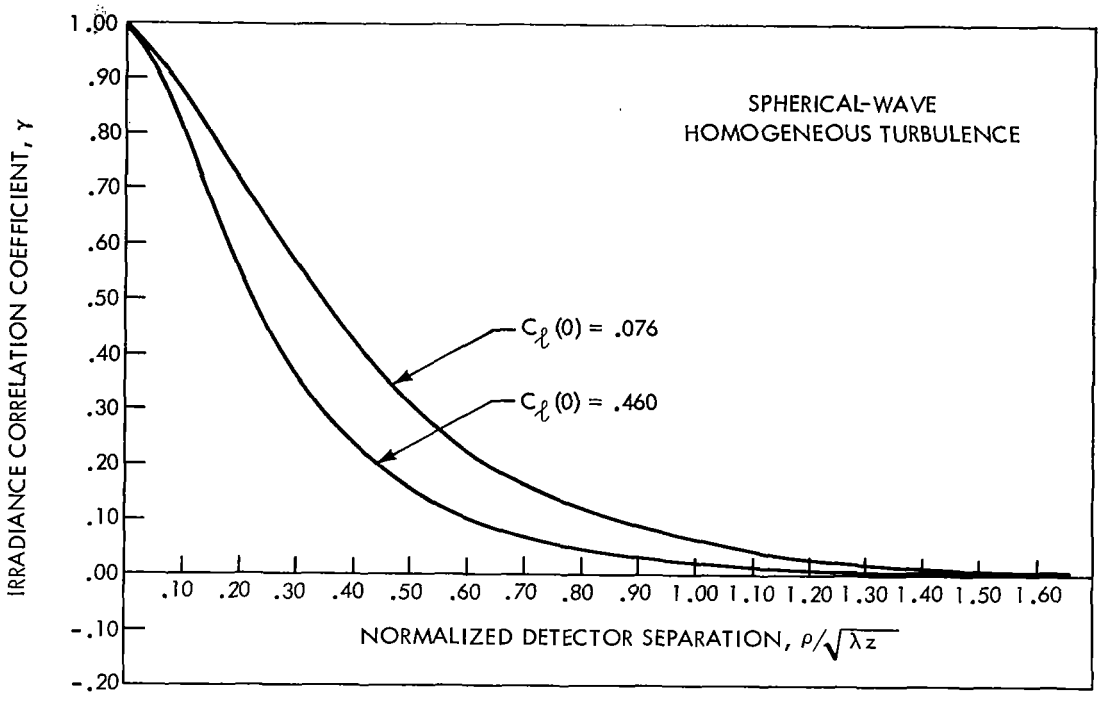

Figure 24. Irradiance correlation coefficient γ as a function of normalized detector separation $\rho/(\lambda z)^{1/2}$. The curves are obtained from Fried's[96] results for the spherical-wave log-amplitude correlation coefficient.

all gains remain constant during the time interval corresponding to a single data point (2 minutes), then gain variation can be easily taken into account.

When the recorded data are played back, the voltages V_1 and V_2 appearing at tape recorder outputs 1 and 2 are related to the irradiance values at detectors 1 and 2 as follows:

$$V_1 = K_1 I_1$$

and

$$V_2 = K_2 I_2 , \tag{108}$$

where K_1 and K_2 include all detector and tape-recorder gains. Consider the playback of the data with outputs V_1 and V_2 connected to amplifier lines 1 and 2,

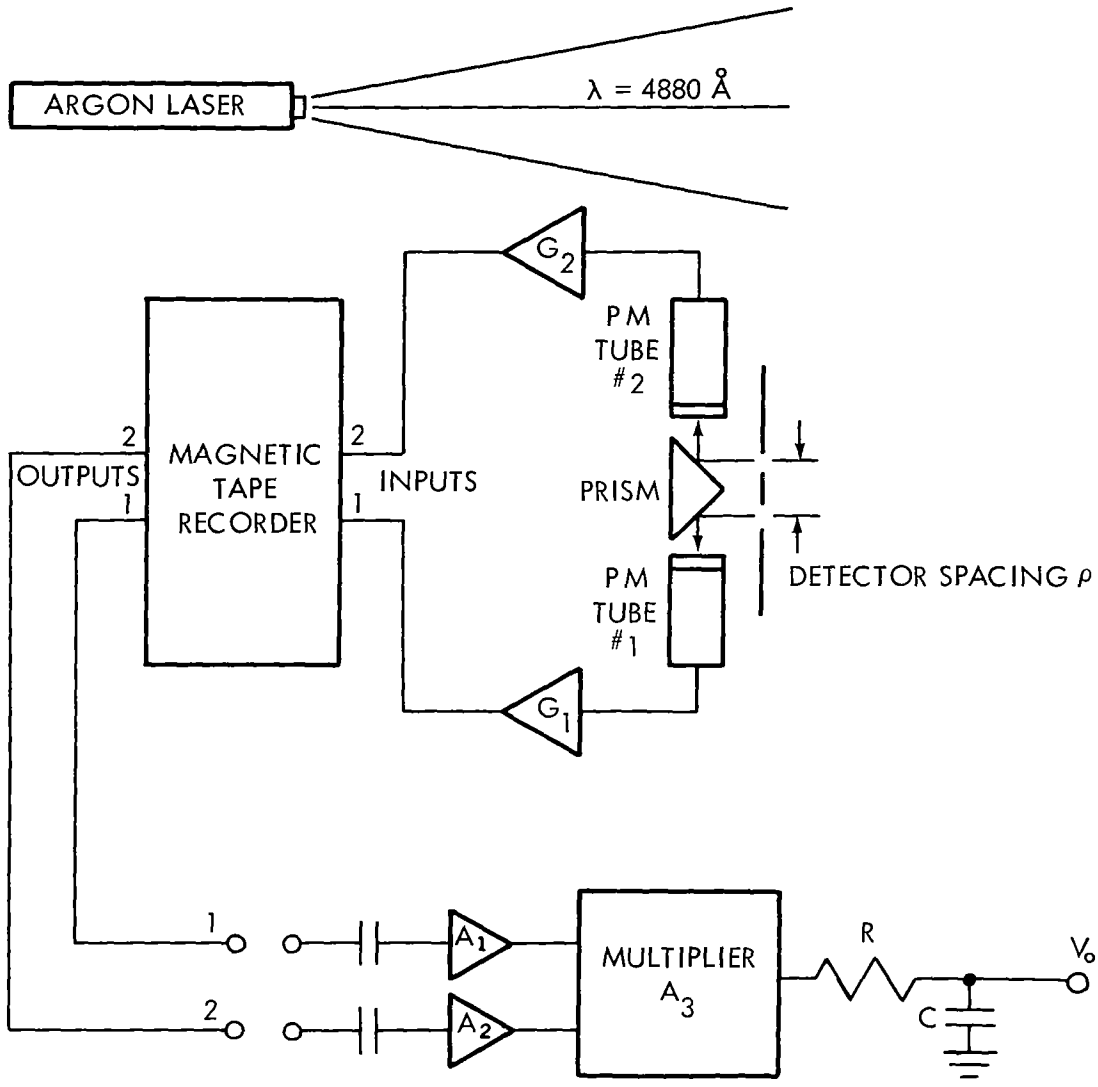

Figure 25. Experimental schematic, spatial correlation.

respectively. Then the output voltage V_0 after a time interval equal to RC (the time constant of the averaging network) is

$$V_0 = \langle A_1 A_2 A_3 (V_1 - \bar{V}_1)(V_2 - \bar{V}_2) \rangle = V_{01}, \tag{109}$$

where $\bar{V}_1$ and $\bar{V}_2$ are the respective average values of V_1 and V_2, and A_1, A_2, A_3 are amplifier gains. Similarly, if we repeat the playback with V_1 connected to

both amplifier lines, we get

$$V_0 = \langle A_1 A_2 A_3 (V_1 - \bar{V}_1)^2 \rangle \equiv V_{02} . \tag{110}$$

Repeating with V_2 connected to both amplifier lines, we get

$$V_0 = \langle A_1 A_2 A_3 (V_2 - \bar{V}_2)^2 \rangle \equiv V_{03} . \tag{111}$$

Therefore,

$$V_{01} / (V_{02} V_{03})^{1/2} = \frac{\langle (V_1 - \bar{V}_1)(V_2 - \bar{V}_2) \rangle}{\left\{ \langle (V_1 - \bar{V}_1)^2 \rangle \langle (V_2 - \bar{V}_2)^2 \rangle \right\}^{1/2}} . \tag{112}$$

Applying Eq. 108, we get

$$V_{01} / (V_{02} V_{03})^{1/2} = \frac{C_I(\rho)}{\left\{ C_{I_1}(0) C_{I_2}(0) \right\}^{1/2}} . \tag{113}$$

Using the assumption of isotropy in the detector plane, we get

$$C_{I_1}(0) = C_{I_2}(0) = C_I(0) .$$

Therefore,

$$\frac{V_{01}}{\left\{ V_{02} V_{03} \right\}^{1/2}} = \gamma . \tag{114}$$

So it is clear that one can evaluate γ for each particular separation ρ by playing back the recorded data three times and measuring the appropriate voltages. From the two minutes of data available for each detector separation, a 30-second

portion was selected such that the signal levels were best contained within the linear range of the amplifier and multiplier circuits. Even so, it was apparent that some of the analyzed data exhibited peak irradiances which exceeded the dynamic range of the tape recorder. This problem will be discussed more fully in the next section.

Experimental Results. Typical data are compared to spherical-wave theory and plotted in Fig. 26. Actual values for the log-amplitude variance at each data point were not available in this case, but the theoretical curves of 0.076 and 0.460 can be expected to contain most of the data. For cases where the log-amplitude variance drops below 0.076, the pertinent theoretical curve is still very close to that shown for $C_\ell(0) = 0.076$. If $C_\ell(0)$ becomes much greater than 0.460, Rytov theory appears to lose its validity, and hence the analytical approaches which produced the results shown in Figs. 23 and 24 are of questionable usefulness.

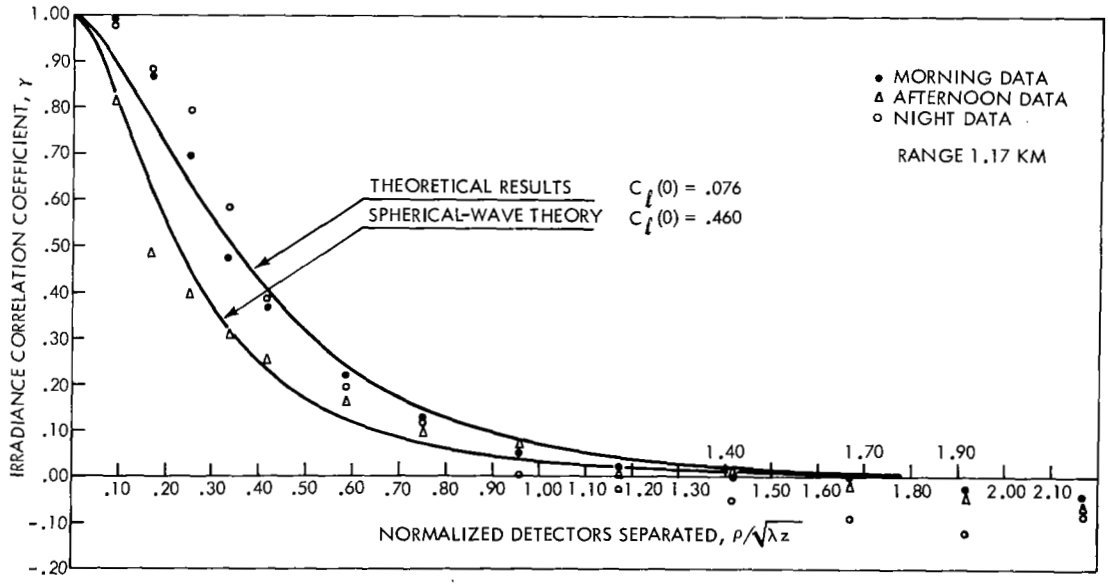

Figure 26. Spatial correlation of irradiance fluctuations.

The data in Fig. 26 show a reasonably good agreement with theory; however, there are some rather disturbing aspects. For most detector separations the data spread is rather large and is certainly greater than that which could be attributed to statistical sampling theory. Also, significant negative correlations for $\rho/(\lambda z)^{1/2} > 1$ appear consistently in the data of Fig. 26.

Certainly some of the data scatter can be attributed to the lack of stationarity of the atmospheric statistics. It is well known that the refractive index structure constant can change by an order of magnitude within a few minutes of time. However, this does not account for the data which lie above the 0.076 curve of Fig. 26 because this curve is not significantly different from the curve for vanishingly small $C_\ell(0)$ obtained from Eq. 107.

Another area of concern is the effect that atmospheric deviations from the Kolmogoroff model spectrum might produce on the measured correlation function. It is shown in Appendix B that, if the refractive index structure function increases as r^p (r being the distance between measurement points), then the log-amplitude variance takes on the range dependence $L^{(3/2+p/2)}$ and a wavelength dependence $k^{(3/2-p/2)}$. Thus if p differs slightly from its usual value 2/3,* then it is clear that the range and wavelength dependence of $C_\ell(0)$ are not drastically altered. However, it is not clear how seriously the shape of the covariance function would change in response to varying p.

*Lawrence and Ochs have suggested in private communications that near ground the refractive index structure function may frequently vary as $r^{1/2}$ due to the fact that input energy to the inertial subrange may be applied throughout the inertial subrange and not just at the outer scale as is usually assumed.

Additional data are shown in Fig. 27. In this case the data were processed through a digital computer (Raytheon 520) as well as through the analog instrumentation of Fig. 25. The computer evaluated $C_\ell(0)$ by calculating the moments of the random variable $1/2\ ln\left[I/\langle I\rangle\right]$, where I is the instantaneous irradiance at one of the detectors shown in Fig. 25 and $\langle I\rangle$ is the average irradiance at the same location. The value of log-amplitude variance changed from point to point for both the afternoon and the night data, but excursions from the mean value were nearly always less than an octave. Therefore, since the dependence of γ on $C_\ell(0)$ is rather weak, we can meaningfully form an "average log-amplitude variance" for both afternoon and night data. Some of the raw data were inspected in terms of their probability density function also. A typical example for one of the 30-second data runs is shown in Fig. 28. The approximately linear behavior on log-gaussian probability paper indicates that the data satisfies this test for log-normality.

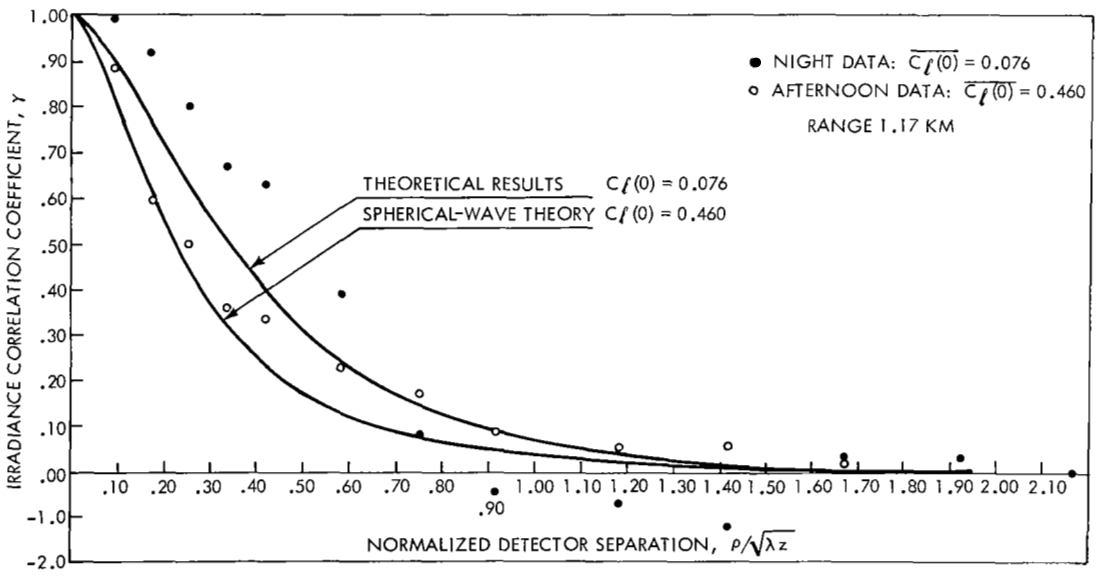

Figure 27. Spatial correlation of irradiance fluctuations.

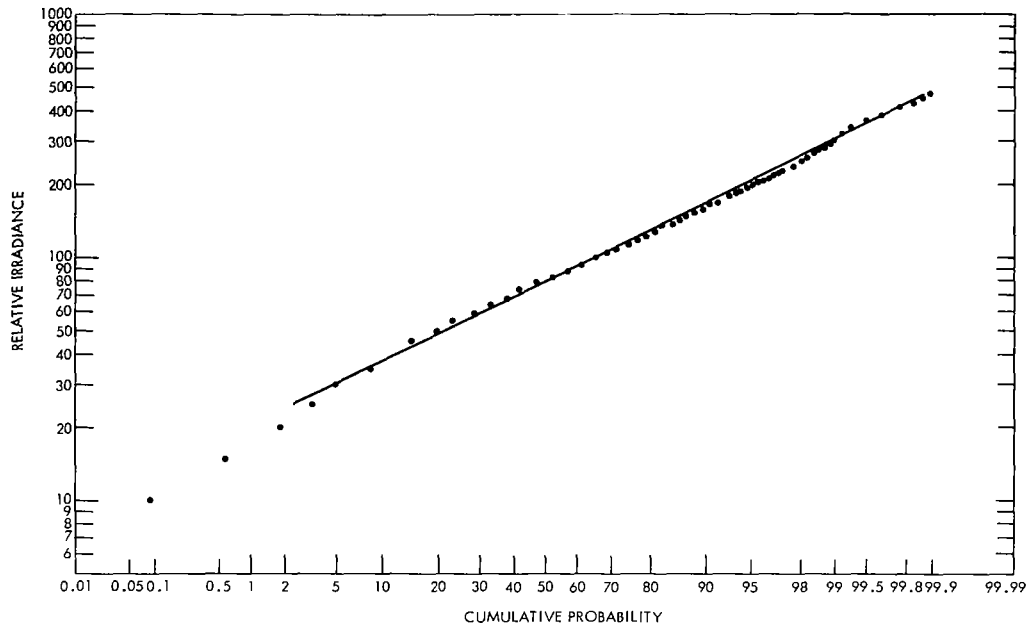

Figure 28. Cumulative probability of irradiance fluctuations. The data are plotted on log-normal probability paper.

The results in Fig. 27 continue to exhibit the wide data spread noted previously. The nighttime data also show a significant negative correlation for $\rho/(\lambda z)^{1/2} \approx 1.4$. It is interesting that the strong turbulence data tend to take on a different shape which is characterized by increasingly positive correlation for large detector separations. This was observed several times in our data and has also been observed by others, either directly[97,98] or indirectly.[99] In Ref. 97 it was found that $\gamma(\rho)$ evaluated at $\rho = (\lambda z)^{1/2}$ may be as great as 0.40.

It is tempting to conclude that this change in the measured shape of $\gamma(\rho)$ for strong irradiance fluctuations is real and is explainable on the basis of the breakdown of Rytov theory. This may be the case, since it is generally agreed that Rytov theory does not successfully predict the behavior of $C_\ell(0)$ for very strong fluctuations; so one would not expect $C_\ell(0)\gamma(\rho)$ to be accurate. However,

one must be very cautious about the results of covariance measurements made on such strongly fluctuating signals. Extremely large dynamic ranges are required for the instrumentation,* and it is not always clear in published reports what the actual dynamic range capability is.

From inspection of the experimental results shown in Figs. 26 and 27 and from the large data spread as well as the anomalous negative correlations which frequently occurred for $\rho/(\lambda z)^{1/2} > 1$, it was decided that there were three areas where the experimental technique could be improved. In an attempt to resolve whether the results had, in fact, been affected by the measurement technique, the following changes were implemented:

(1) The dynamic range of the instrumentation was increased by 6 db. The limiting processor in the data reduction system was the FM magnetic tape recorder. The signal representing instantaneous irradiance is inherently unipolar, owing to the type of optical detectors employed. However, by DC-biasing the signal voltage to one extreme signal level, the useful recording range of the magnetic tape is fully utilized and is increased by 6 db over the unbiased case. The bias level must be subtracted during data reduction if accurate average values are required. The signal-to-noise ratio of the tape recorder in this configuration was 43 db.

(2) The low-frequency cutoff implied by the capacitor coupling preceding the multiplier (see Fig. 25) was changed from 4 Hz to 1 Hz.

*See Appendix C of this report and Appendix A of Ref. 46 for a discussion of dynamic range requirements in the measurement of log-normal random variables.

(3) The analog multiplier used in the data reduction (see Fig. 25) was replaced by a digital multiplier.

Steps 2 and 3 were actually implemented by replacing the preamplifiers (A_1, A_2), the multiplier A_3, and the RC averaging components with a digital processor: the Hewlett-Packard Model 3721 A correlator. The analog multiplier was a Burr-Brown Model 1671 and had a bandwidth of 40 kHz and a transfer function accuracy of 0.15%. The bandwidth was not a constraint (the tape recorder was run at 7.5 inches per second and limited bandwidth from DC to 2.5 kHz), but the transfer function accuracy was a source of concern. Especially for large $\rho'(\lambda z)^{1/2}$ values, one can expect a significant portion of the covariance to be contributed when one input is at a very low level (where the percent error is high) and the other input is at a rather high level. Detailed specifications for the 3721 A correlator are not listed here, since they are readily available in the manufacturer's literature. However, we do note that it is a completely digital device with a low-frequency cutoff of either 1 Hz or DC and a high-frequency limitation of 250 kHz. It is possible to compute any of the following in an on-line configuration:

(1) Autocorrelation of a single signal

(2) Cross-correlation of two signals

(3) Amplitude probability density function

(4) Amplitude cumulative density function.

All correlation calculations are made with 100 timelags of selectable spacing. Results are presented on a storage oscilloscope and can be interfaced with an X-Y recorder.

Additional data were recorded with a biased recording technique and processed through the digital correlator. The results are shown in Fig. 29. Log-amplitude-variance values were not available for these data, but both the morning and evening fluctuations were relatively weak and can be expected to lie closer to the 0.076 curve than to the 0.460 curve. The quantity of data analyzed was small* but, even so, some significant differences are apparent. The data spread between runs (which were separated in time by 11 hours) are considerably less than those noted

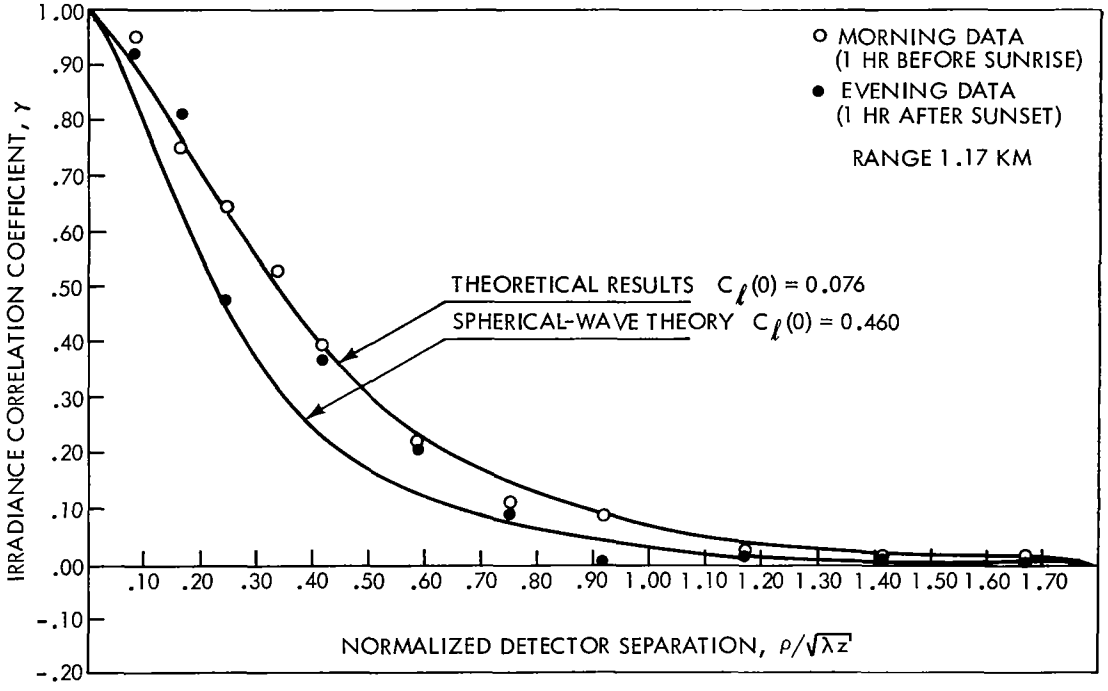

Figure 29. Spatial correlation of irradiance fluctuations (digital-data processing).

*The digital processor was obtained on a short-term loan basis and was available only for two days. During this time the spatial correlation data presented in Fig. 7, as well as a somewhat larger quantity of spectral correlation data [to be presented in Part (b) of this section], were reduced and plotted.

previously in Figs. 26 and 27. Also, the anomalous negative correlations for $\rho \approx (\lambda z)^{1/2}$ are no longer present. Judged by this limited data sample, it appears that the extension of the dynamic range and the employment of the seemingly more accurate digital processing have resulted in measurements which are in excellent agreement with spherical-wave theory.

An added output which was available from this digital analysis was the more general time-dependent correlation coefficient $\gamma(\rho, \tau)$, defined as

$$\gamma(\rho, \tau) = \frac{\left\langle \left\{ I(\bar{X}_1, t+\tau) - \langle I(\bar{X}_1, t+\tau) \rangle \right\} \left\{ I(\bar{X}_2, t) - \langle I(\bar{X}_2, t) \rangle \right\} \right\rangle}{\left[\left\langle \left\{ I(\bar{X}_1, t+\tau) - \langle I(\bar{X}_1, t+\tau) \rangle \right\}^2 \right\rangle \left\langle \left\{ I(\bar{X}_2, t) - \langle I(\bar{X}_2, t) \rangle \right\}^2 \right\rangle \right]^{1/2}} , \tag{115}$$

where

$$\rho = |\bar{X}_1 - \bar{X}_2| .$$

The assumptions of isotropy and homogeneity are again incorporated in the definition; $\gamma(\rho, 0)$ is identical with the correlation coefficient $\gamma(\rho)$ defined in Eq. 107 and used in Figs. 23, 24, 26, 27, and 29.

Consider the following model for the propagation problem. The turbulons which exist along the optical path vary very slowly in time but are transported across the path in a horizontal sense by a wind vector $\bar{V}_{H,N}$ which is both horizontal and perpendicular to the optical path.* In this situation the field at $\bar{X}_1$ at

*We note that the component of the wind vector which is along the path has some effect on the problem, but it is shown in Ref. 2, p. 215, that this is usually insignificant.

time t_1 is the same as that at $\bar{X}_2$ at time

$$t_1 \pm \frac{|\bar{X}_1 - \bar{X}_2|}{|\bar{V}_{H,N}|} ,$$

where $\bar{X}_1$ and $\bar{X}_2$ are position vectors which are collinear with one another and parallel to $\bar{V}_{H,N}$ and which are also assumed to lie in a plane perpendicular to the optical path. The plus or minus ambiguity is easily resolved by inspecting the relative directions of $\bar{X}_1 - \bar{X}_2$ and $\bar{V}_{H,N}$. If this model is accurate, one can always expect to obtain nearly perfect correlation between two side-by-side detectors (such as in Fig. 25) for some particular time delay

$$\tau = \frac{|\bar{X}_1 - \bar{X}_2|}{|\bar{V}_{H,N}|} .$$

The time-dependent correlation function $\gamma(\rho, \tau)$ was evaluated for most of the data shown in Fig. 29. Some typical results are presented in Figs. 30 and 31. The data of Figs. 30 and 31.A were recorded about one hour after sunset. The wind was rather calm, with an average component of about 2.0 meters per second perpendicular to the optical path. This wind measurement was made at the transmitter-receiver station, and it is not known how well this measurement represents the actual average wind velocity along the path. It would have been more meaningful to measure the velocity at the folding mirror location, since turbulence in this region of the path can be expected to dominate the field

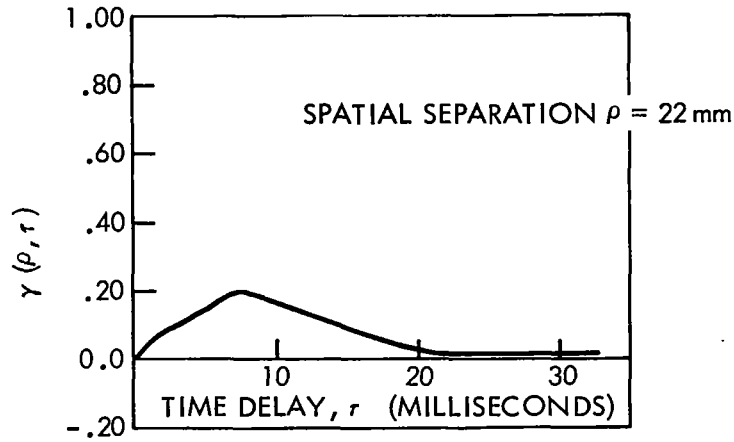

(A)

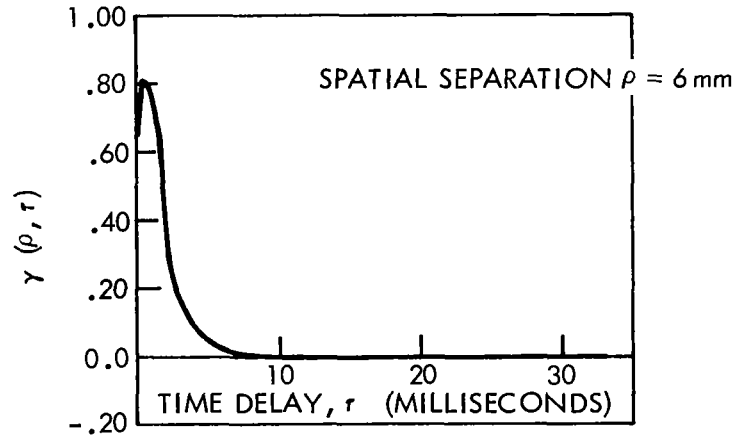

(B)

Figure 30. Time-dependent spatial correlation coefficient $\gamma(\rho, \tau)$ as a function of time delay τ.

fluctuations, but this point was not accessible.* The Fig. 31.B data were recorded about one hour before sunrise, during a period of gusty winds with an average perpendicular component of about 7.5 meters per second.

*For spherical-wave propagation the turbulence near the source has little to do with the amplitude fluctuations, since in this region the beam cross section is small compared to the turbulence scale size. The net effect of this turbulence is to "steer" the beam as a whole rather than break up the beam. Near the receiver, the small-angle scattering aspect of optical propagation tends to minimize the effects of turbulence.

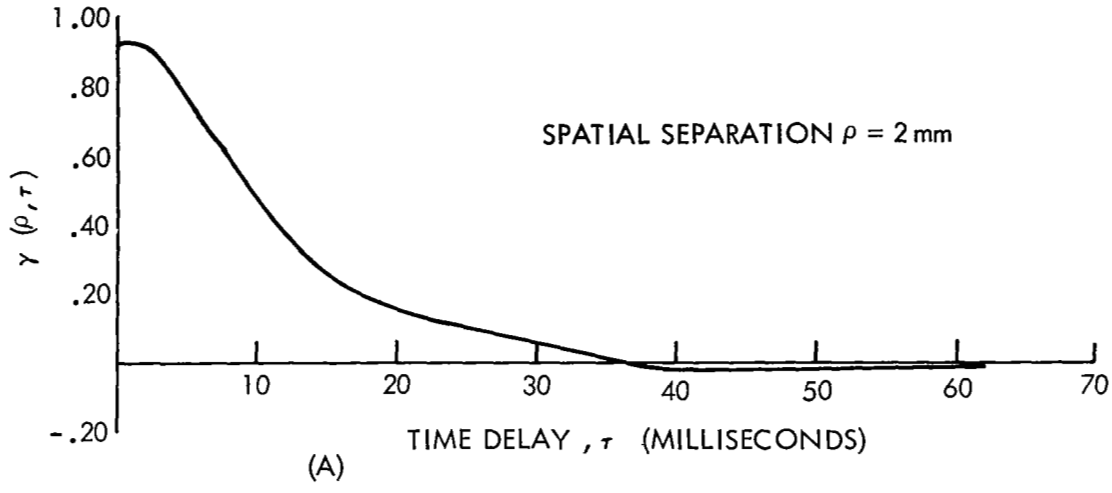

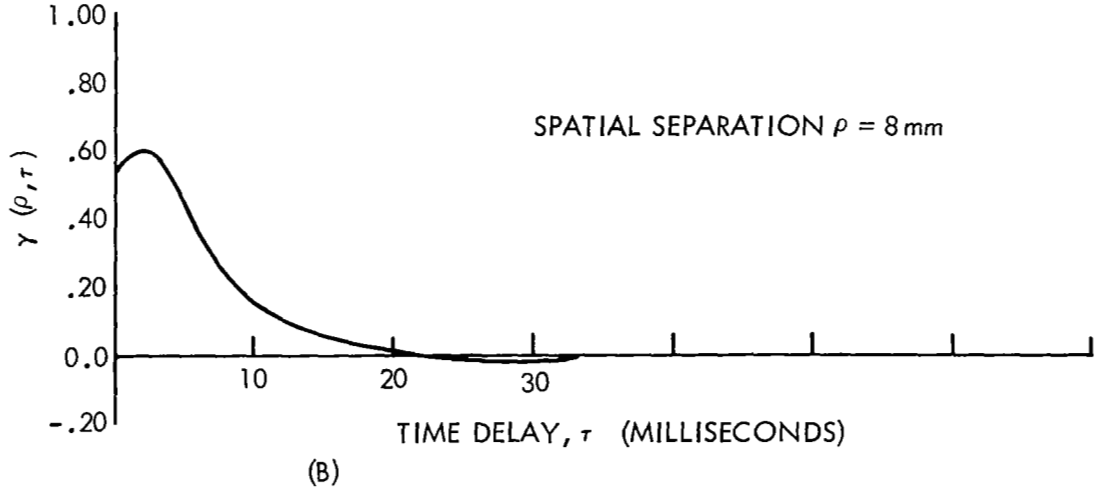

Figure 31. Time-dependent spatial correlation coefficient $\gamma(\rho, \tau)$ as a function of time delay τ.

The failure of any of the curves of Figs. 30 and 31 (or any of the other data) to exhibit near-unity correlation at some time delay shows clearly that the often-assumed propagation model described earlier is inadequate for predicting the time behavior of irradiance fluctuations. Several possibilities exist for explaining the observed data:

(1) The motion of the turbulons across the optical path may contain a significant vertical component due to buoyancy effects induced by the lapse rate. This effect can be expected to be emphasized in rather calm conditions (such as existed in Figs. 30 and 31.B).

(2) The average wind component perpendicular to the propagation path may differ significantly along the path.

(3) The concept of "frozen-in-turbulence" described earlier may not be valid.

It is felt that (2) is probably not very significant, since for spherical-wave propagation it is the turbulence near the midpoint of the path which dominates and the average wind velocity need only be uniform in this region. Also, alternative (3) seems unlikely since this concept (usually referred to as Taylor's hypothesis) has been extensively investigated by micrometeorologists[24,25] and is generally considered to be a valid concept. We conclude that it is most likely the addition of a vertical component to the motion of the turbulons which has altered $\gamma(\rho, \tau)$ from its expected form. It is quite possible that greater degree of correlation would have appeared for some timelag if the detectors had been located such that the line joining their respective apertures was tilted rather than completely horizontal. We summarize the results of this section as follows:

(1) It has been shown that the previously derived log-amplitude covariance can be transformed to the more useful irradiance covariance under the assumption of log-normality.

(2) Measurements of the irradiance correlation coefficient over a 1.17-km horizontal path have been shown to be in good agreement with the Rytov spherical-wave theory.

(3) The propagation model employing "frozen-in-turbulence" undergoing horizontal transport has been found inadequate in this experiment under low-wind conditions.

b. Spectral Correlation: Theory. We next consider the problem of evaluating the degree of correlation between amplitude fluctuations which are imposed on two beams of different frequency which have traversed exactly the same optical path. We neglect the dependence of the average index of refraction on wavelength, since the average value does not enter into the problem of amplitude fluctuations. Heuristically, different frequency beams will exhibit less than perfect correlation in their amplitude fields since the ratio of wavelength to turbulon size is different for each beam. Thus, even though each propagating beam "sees" the exact same refractive index field, the amplitude fields will tend to lose correlation if the measurement plane is far removed from a substantial amount of the turbulence.

The spectral covariance of irradiance $C_I(0, \theta)$ can be defined as

$$C_I(0, \theta) = \left\langle \left\{ I_1(\bar{X}) - \langle I_1(\bar{X}) \rangle \right\} \left\{ I_2(\bar{X}) - \langle I_2(\bar{X}) \rangle \right\} \right\rangle , \qquad (116)$$

where

$I_1(\bar{X})$ = the irradiance of beam 1 (of wave number k_1),

$I_2(\bar{X})$ = the irradiance of beam 2 (of wave number k_2),

and

$$\theta = \frac{|k_2 - k_1|}{k_2 + k_1} ,$$

and we emphasize that both irradiances are measured at the same point $\bar{X}$. As was noted earlier, for spherical- and plane-wave propagation,

$$I(X) = I_0(X) \exp\left[2\ell(X)\right] . \qquad (99)$$

(We drop the vector notation on the position vector $\bar{X}$ by applying the usual homogeneity - isotropy assumptions.) Substituting Eq. 99 into Eq. 116, we write

$$C_I(0, \theta) = I_{01} I_{02} \left\langle \exp\left[2\ell_1 + 2\ell_2\right] - \exp\left[2\ell_1\right] - \exp\left[2\ell_2\right] + 1 \right\rangle \cdot \quad (117)$$

Using the relationship

$$\left\langle \exp\left[2\ell\right] \right\rangle = 1$$

and the right-hand side of Eq. 101, we have

$$C_I(0, \theta) = I_{01} I_{02} \left[\exp\left\{4C_\ell(0, \theta)\right\} - 1\right], \quad (118)$$

where $C_\ell(0, \theta)$ is the log-amplitude covariance for beams 1 and 2 and is defined as

$$C_\ell(0, \theta) = \left\langle \left\{\ell_1(X) - \left\langle \ell_1(X) \right\rangle\right\} \left\{\ell_2(X) - \left\langle \ell_2(X) \right\rangle\right\} \right\rangle \cdot \quad (119)$$

In Ref. 100 it is shown that, for plane-wave propagation with wave numbers k_1 and k_2 through homogeneous and isotropic Kolmogorov-type turbulence, the generalized spectral covariance of log amplitude $C_\ell(\rho, \theta)$ may be written as

$$C_\ell(\rho, \theta) = C_{\ell'}(0) \left(1 - \theta^2\right)^{7/6} \left[F\left\{ \frac{\rho}{\left[\frac{4z}{k\left(1 - \theta^2\right)}\right]^{1/2}} \right\} - \theta^{5/6} F\left\{ \frac{\rho}{\left[\frac{4z\theta}{k\left(1 - \theta^2\right)}\right]^{1/2}} \right\} \right], \quad (120)$$

where F is the function use earlier in Eq. 106* and $C_\ell'(0)$ is evaluated at wave number $|k_2 - k_1|/k_2 + k_1$. Since $F(0) = 1$, $C_\ell(0, \theta)$ becomes

$$C_\ell(0, \theta) = C_\ell'(0)\left[1 - \theta^2\right]^{7/6}\left[1 - \theta^{5/6}\right]$$

$$\equiv C_\ell'(0)\, G(\theta) \quad . \tag{121}$$

Substituting this result into Eq. 118, we have

$$C_I(0, \theta) = I_{01}\, I_{02}\left[\exp\left\{4C_\ell'(0)\, G(\theta)\right\} - 1\right] \quad . \tag{122}$$

Evaluating Eq. 104 at $\rho = 0$, we have

$$C_I(0) = I_0^2\left[\exp\left\{4C_\ell(0)\right\} - 1\right],$$

and, substituting this into the defining equation for the spectral irradiance correlation coefficient $\gamma_{12}(\theta)$, we can write

$$\gamma_{12}(\theta) \equiv C_I(0, \theta) \Big/ \left(C_{I_1}(0)\, C_{I_2}(0)\right)^{1/2}$$

$$= \frac{\exp\left\{4C_\ell'(0)\, G(\theta)\right\} - 1}{\left(\left[\exp\left\{4C_{\ell_1}(0)\right\} - 1\right]\left[\exp\left\{4C_{\ell_2}(0)\right\} - 1\right]\right)^{1/2}} \quad . \tag{123}$$

The result is now in a form such that for various strengths of turbulence (i.e., various log-amplitude variances) the correlation between two plane waves with

*We note that the function $F(\rho)$ defined in Eq. 106 can be expressed more precisely in terms of the dimensionless variable $\rho/(\lambda z)^{1/2}$; therefore, $F(\rho)$ becomes $F\ \rho/(\lambda z)^{1/2}$.

wave numbers k_1 and k_2 can be numerically evaluated. We assume 7/6-power wave number dependence for log-amplitude variance (Eq. 52). Results are shown in Fig. 32, where beam 1 is held constant at 6328 Å and beam 2 varies over shorter wavelengths. The assumed turbulence levels apply to beam 1. The $C_{\ell_1}(0)$ values were chosen so as to bracket the conditions under which Rytov theory can be expected to be valid. The 0.05 $C_{\ell_1}(0)$ curve is not significantly different from the vanishingly weak turbulence condition. So now, just as in Part (a), we have theoretical predictions which can be rigorously compared to experiment.

Experiment. The experimental schematic is shown in Fig. 33. A helium-neon laser operating at 6328 Å was aligned collinear with an argon laser through a mirror-beamsplitter combination and transmitted over the folded 1.17-km horizontal path. The two lasers had the following characteristics:

Helium - Neon Laser (Spectra-Physics 130B)

Power (TEM_{00}):	1.0 mW.
Beam diameter ($1/e^2$ points):	1.4 mm.
Beam divergence (total angle):	0.7 mr.
Amplitude stability (short term):	1% (RMS).
Amplitude stability (long term):	2.8% (RMS).
Wavelength:	6328 Å.

Argon Laser (RCA - LD 2100)

Power (TEM_{00}, all lines):	125 mW.
Beam diameter ($1/e^2$ points):	1.2 mm.
Beam divergence (total angle):	0.7 mr.

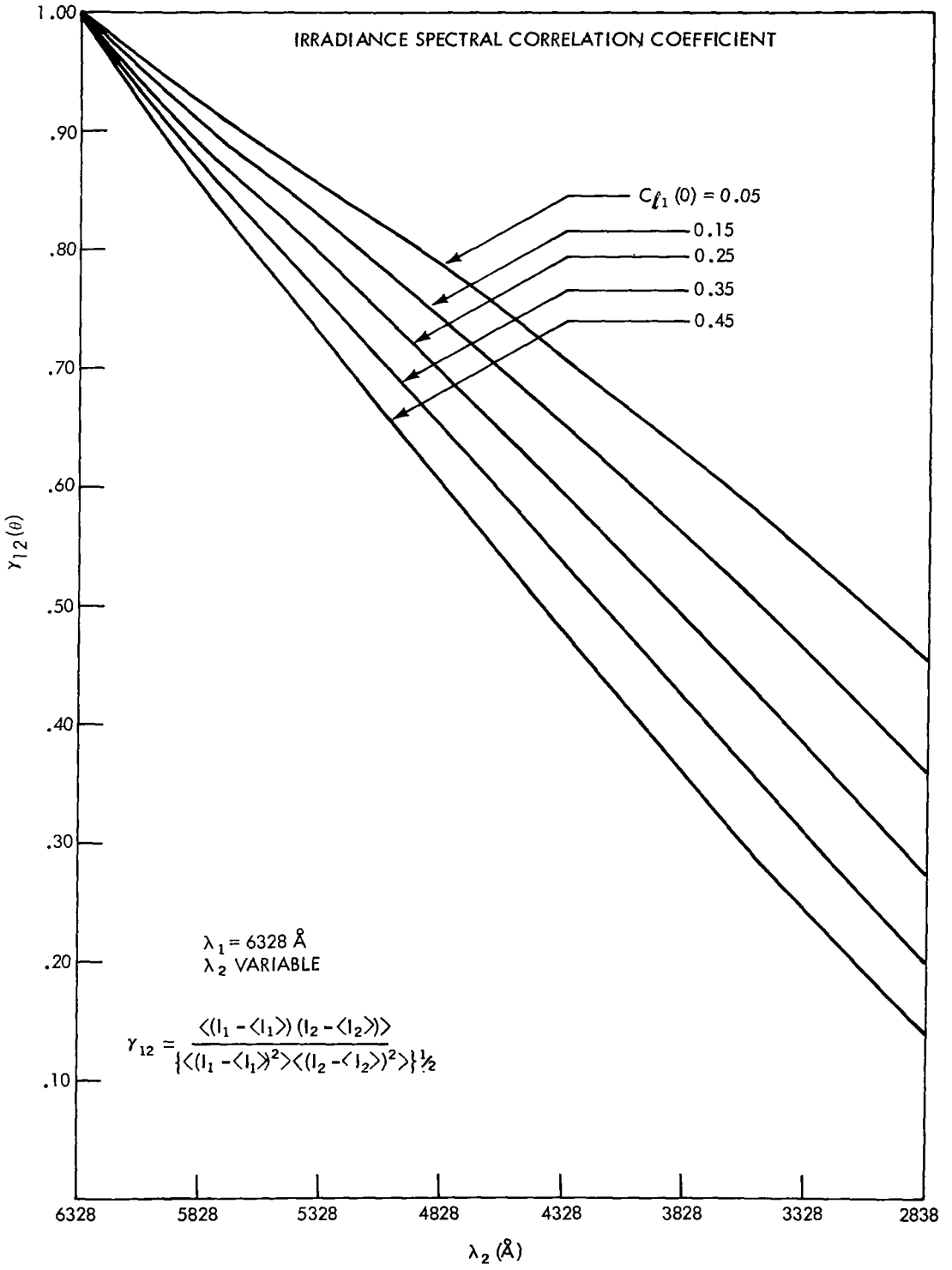

Figure 32. Irradiance spectral correlation coefficient $\gamma_{12}(\theta)$. The assumed turbulence levels apply to beam 1, which has wavelength 6328 Å in all cases.

Amplitude stability (total):	1.5% (RMS) .
Wavelengths:	4579 Å individual power 5 mW.
	4658 Å individual power 1 mW.
	4727 Å individual power 5 mW.
	4765 Å individual power 16 mW.
	4880 Å individual power 50 mW.
	4965 Å individual power 10 mW.
	5017 Å individual power 5 mW.
	5145 Å individual power 30 mW.

The argon unit was operated on one spectral line at a time. Each photomultiplier detector was equipped with optical filters such that detector 1 "saw" only the He-Ne wavelength and detector 2 "saw" only the particular argon wavelength being transmitted. The detected signals were amplified, as required, and recorded on magnetic tape in a manner identical to that described earlier. The two signals were later played back through the analog circuitry of Fig. 33 to evaluate $\gamma_{12}(\theta)$.

Results. Data were recorded under conditions of strong (mid-afternoon) and weak (night) turbulence. The results are shown in Fig. 34 superimposed on the theoretical predictions of Fig. 32. Each plotted point represents 40 seconds of data.* Additional night data are shown in Fig. 35. The nighttime data show an acceptably small spread but exhibit very poor agreement with theory. The

*We note that this part of the report actually compares plane-wave theory with spherical-wave experiments. As far as is known, no spherical-wave analysis of this problem is available.

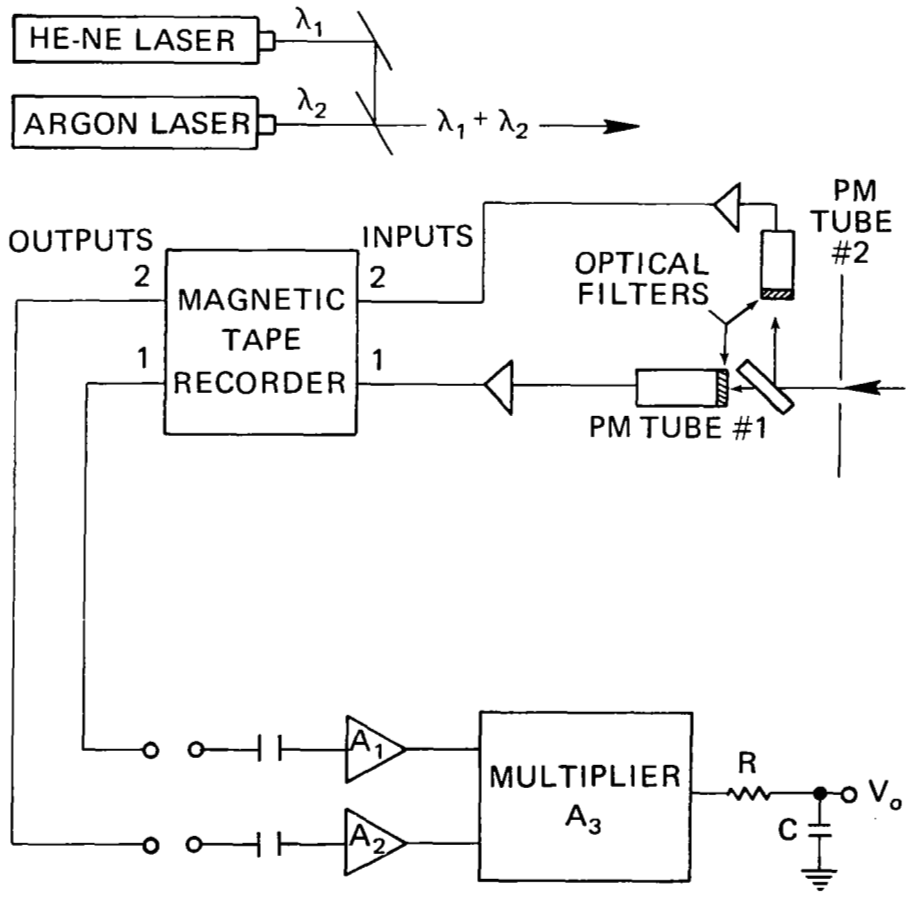

Figure 33. Experimental schematic, spectral correlation.

daytime measurements appear more compatible with theory but have a large spread. As before, no significant portion of this spread can be ascribed to statistical sampling theory, since the $2B_{eq}$. T product is large.* Both sets of measurements (Figs. 34 and 35) were obtained under weak-wind conditions. Typically, the wind speed ranged from absolute calm up to 2 meters per second. As has been noted by other experimenters, under such conditions there may not be enough turbulent energy present to generate an inertial subrange. Under such

*See Appendix A for a discussion of the statistical aspects of the problem.

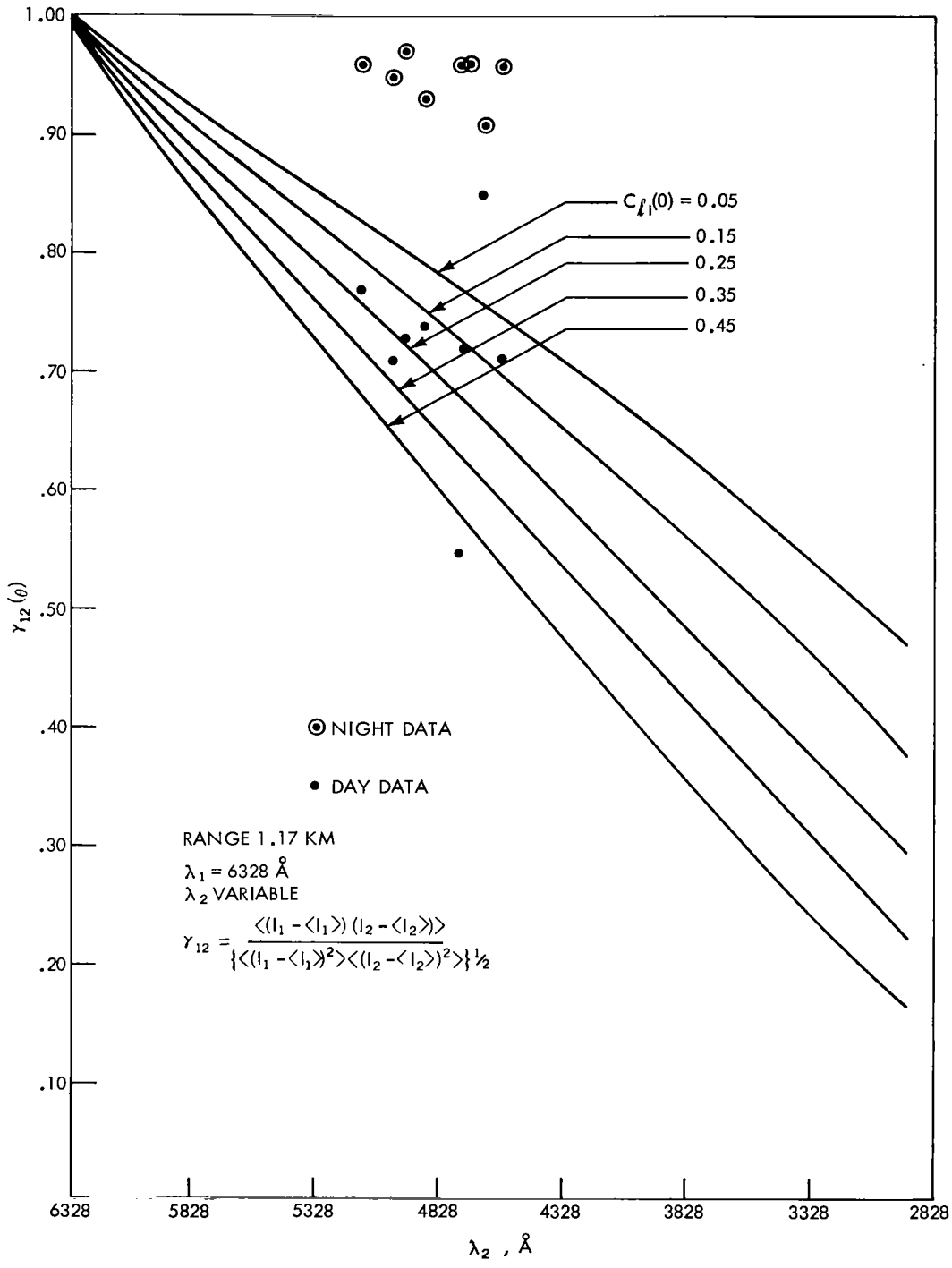

Figure 34. Experimental results, spectral correlation—run # 1, analog data reduction.

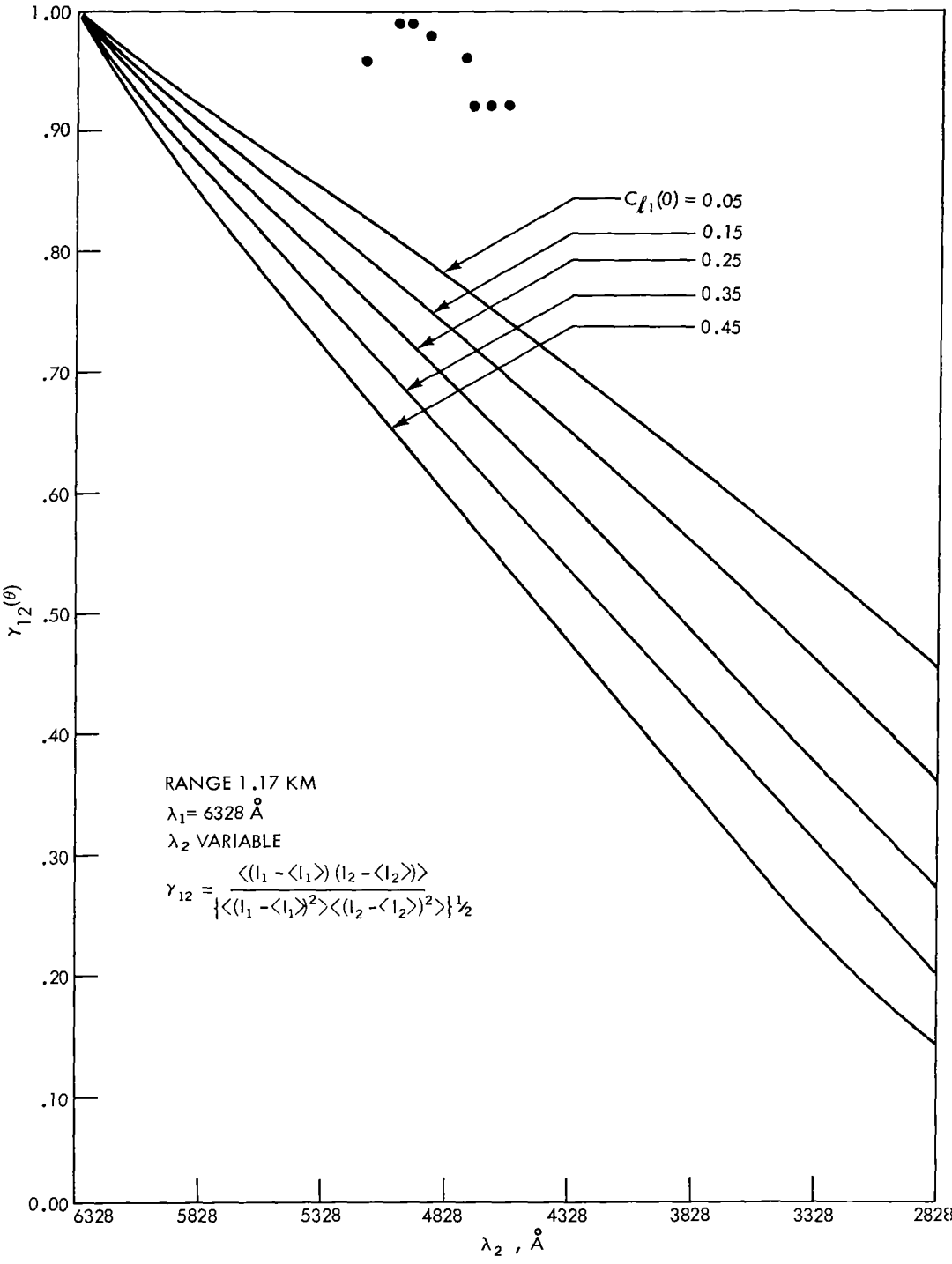

Figure 35. Experimental results, spectral correlation—run # 2, analog data reduction.

conditions, the turbulent field can be expected to lose its homogeneous and isotropic properties and take on something other than a Kolmogorov-type spatial spectrum. Solutions to the optical propagation problems do not exist for such conditions; therefore, measurements taken under such circumstances are nearly meaningless. Sufficient meteorological instrumentation was not available at the time of measurement to determine definitely that this was the case; therefore, this explanation is merely offered conjecturally. The conditions for the existence of an inertial subrange during midday are less dependent on wind speed, since the strong lapse rate which usually exists at this time is a potentially large source of input turbulent energy. It is possible that the afternoon data of Fig. 34 are more representative of a properly conducted experiment.

After this preliminary look at data, it was decided that the remainder of the experimental measurements should not be taken at night; this was to minimize the possibility of encountering non-isotropic turbulence. In addition, the experimental modifications described in part a. were installed. That is, the tape-recorder dynamic range was increased by 6 db, the low-frequency cutoff in the covariance calculation was changed from 4 Hz to 1 Hz, and a digital processor was substituted for the analog multiplier and averaging circuits. Some range flexibility was also incorporated by installing another folding mirror on the range. This mirror was also flat, with a diameter of 30.5 cm, and located so as to provide a second folded path of length 400 meters. The results of measurements taken over this short path in late January are shown in Figs. 36-39. The graphs are labeled with the hours of the day of the respective data run, with zero hour at midnight. Each plotted point represents 30 to 60 seconds of raw data. A

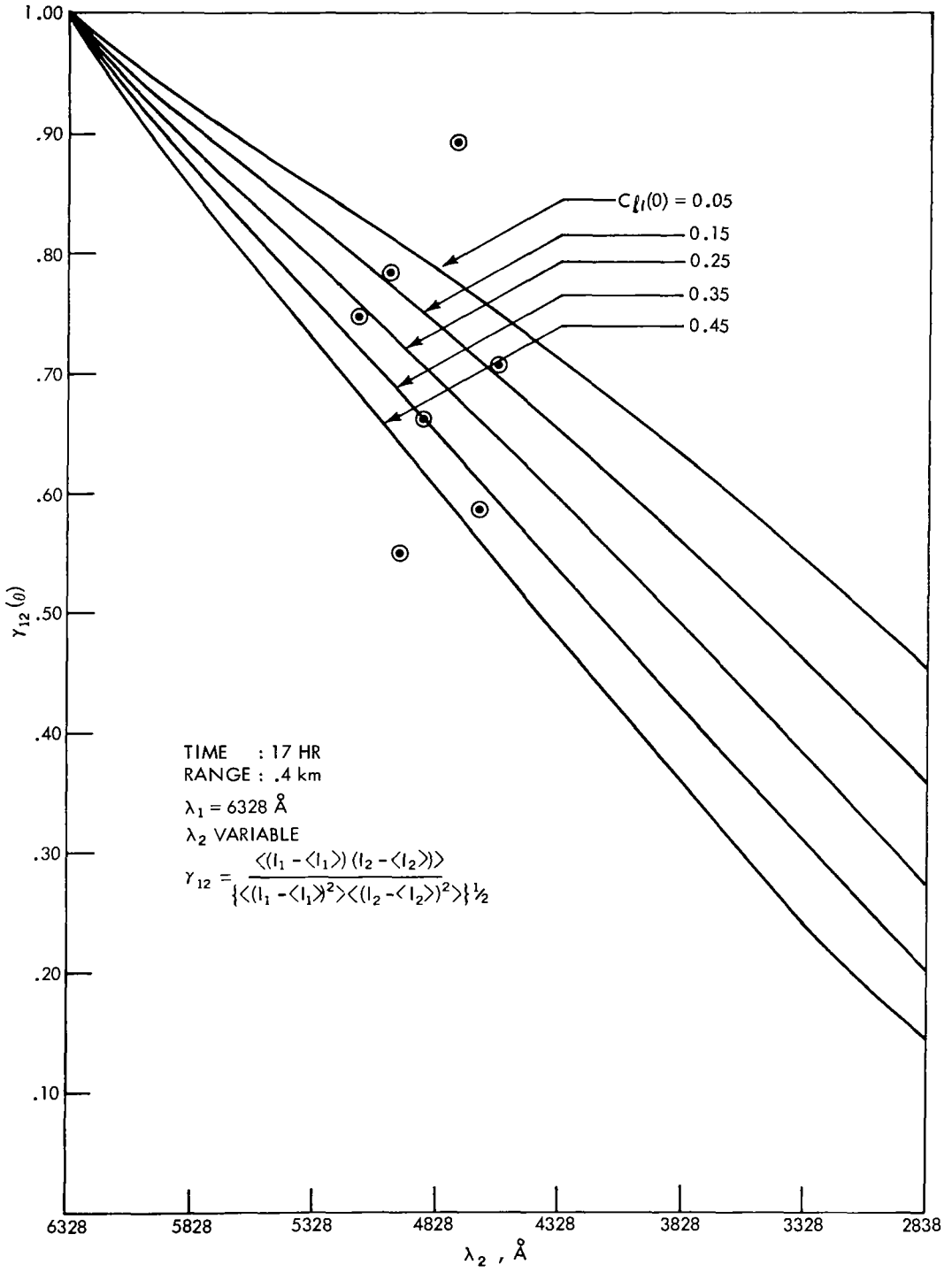

Figure 36. Experimental results, spectral correlation—run # 1, digital data reduction.

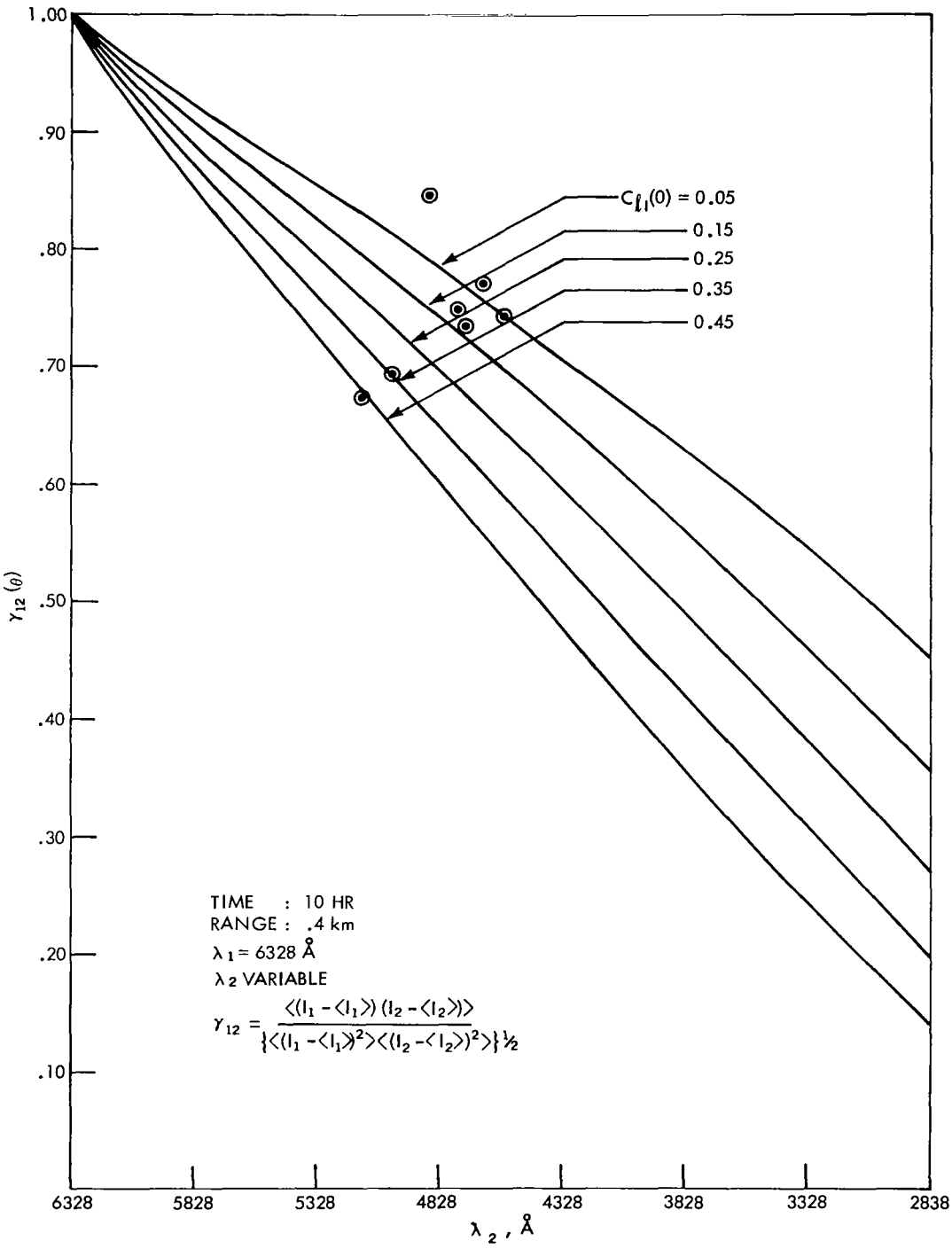

Figure 37. Experimental results, spectral correlation—run # 2, digital data reduction.

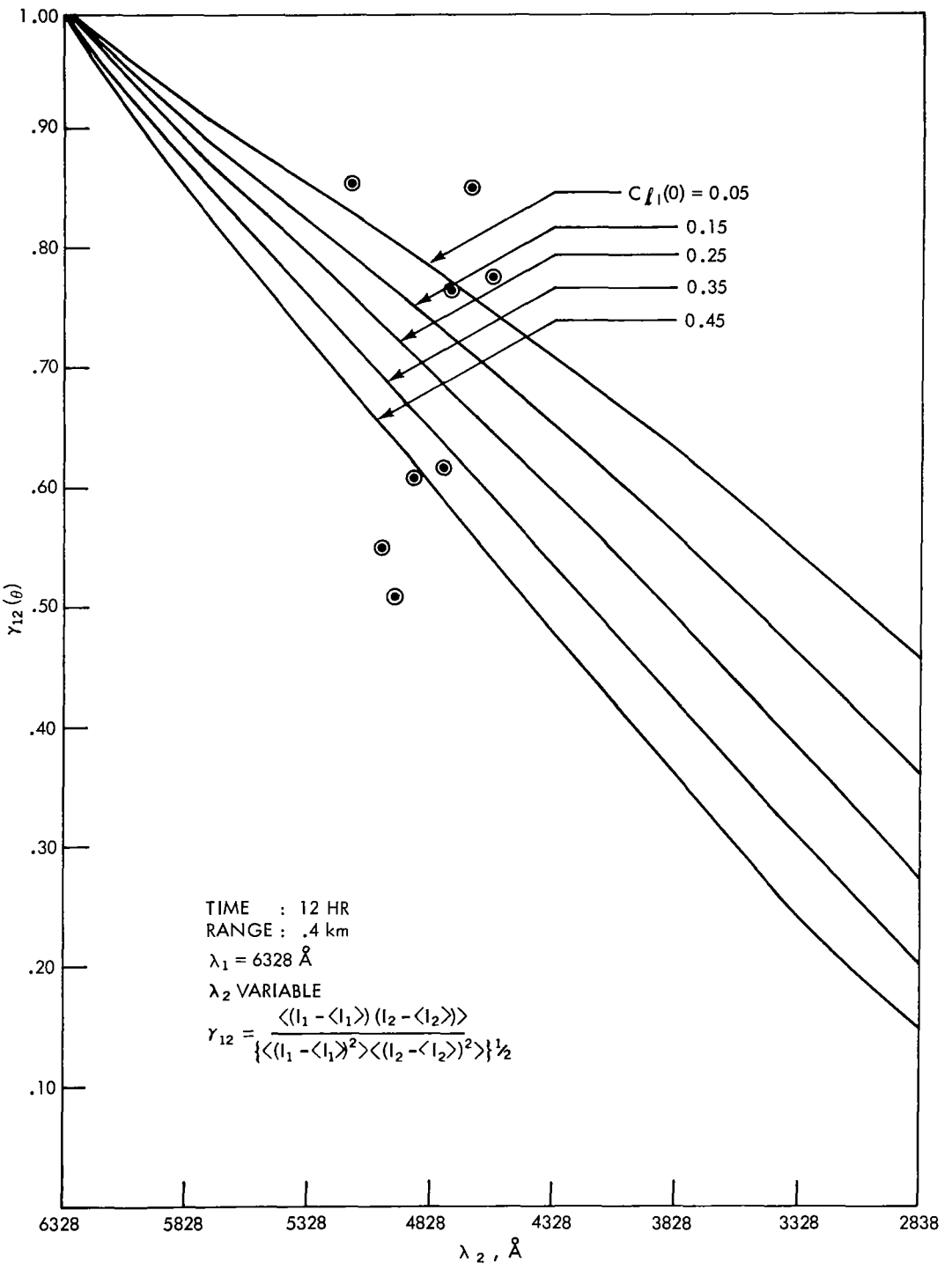

Figure 38. Experimental results, spectral correlation—run # 3, digital data reduction.

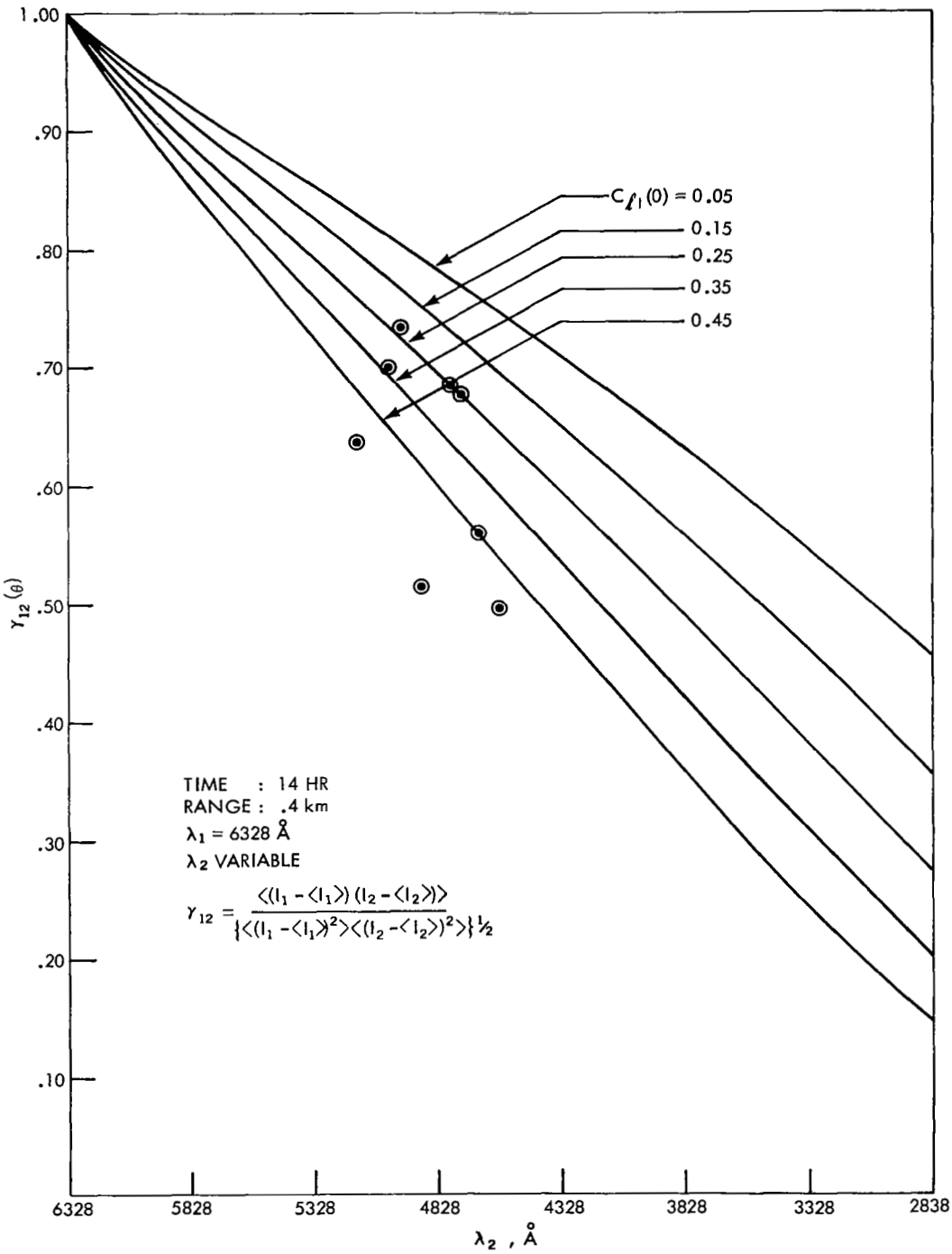

Figure 39. Experimental results, spectral correlation—run # 4, digital data reduction.

typical set of measurements (i.e., a data run at each of the 8 argon laser wavelengths) took about 30 minutes to complete. After each data point, the optical alignment between transmitted and received beams was checked. Both photomultiplier detectors were checked at each wavelength to make certain that no cross-talk existed.

The values for γ_{12} exhibit a very large scatter, although the large nighttime correlations of Figs. 34 and 35 are absent. The 4727 Å data point of Fig. 36 and the 4965 Å measurement of Figs. 37 and 41 were lost during the data analysis procedure owing to operator mishaps.

The measurements taken over the full 1.17-km path are shown in Figs. 40–42. As in the short-range measurements the data scatter is so large that it masks any decrease of correlation with wavelength, if indeed there really is any over the span inspected (i.e., 5145 Å to 4579 Å). It is interesting to note that an order of magnitude change in the refractive index structure constant C_n^2 would theoretically be sufficient to move a data value from the $C_\ell(0) = 0.05$ curve to a point somewhat below the $C_\ell(0) = 0.45$ curve. In this light, the results obtained in Figs. 34–42 should not be too surprising.

The average values of the short- and long-range data are plotted in Figs. 43 and 44, respectively. The time-dependent correlation coefficient $\gamma_{12}(\theta)$ defined as

$$\gamma_{12}(\tau, \theta) = \frac{\left\langle \left\{ I_1(\bar{X}, t+\tau) - \left\langle I_1(X, t+\tau) \right\rangle \right\} \left\{ I_2(X, t) - \left\langle I_2(X, t) \right\rangle \right\} \right\rangle}{\left[\left\langle \left\{ I_1(X, t+\tau) - I_1(X, t+\tau) \right\}^2 \right\rangle \left\langle \left\{ I_2(X, t) - \left\langle I_2(X, t) \right\rangle \right\}^2 \right\rangle \right]^{1/2}}, \quad (124)$$

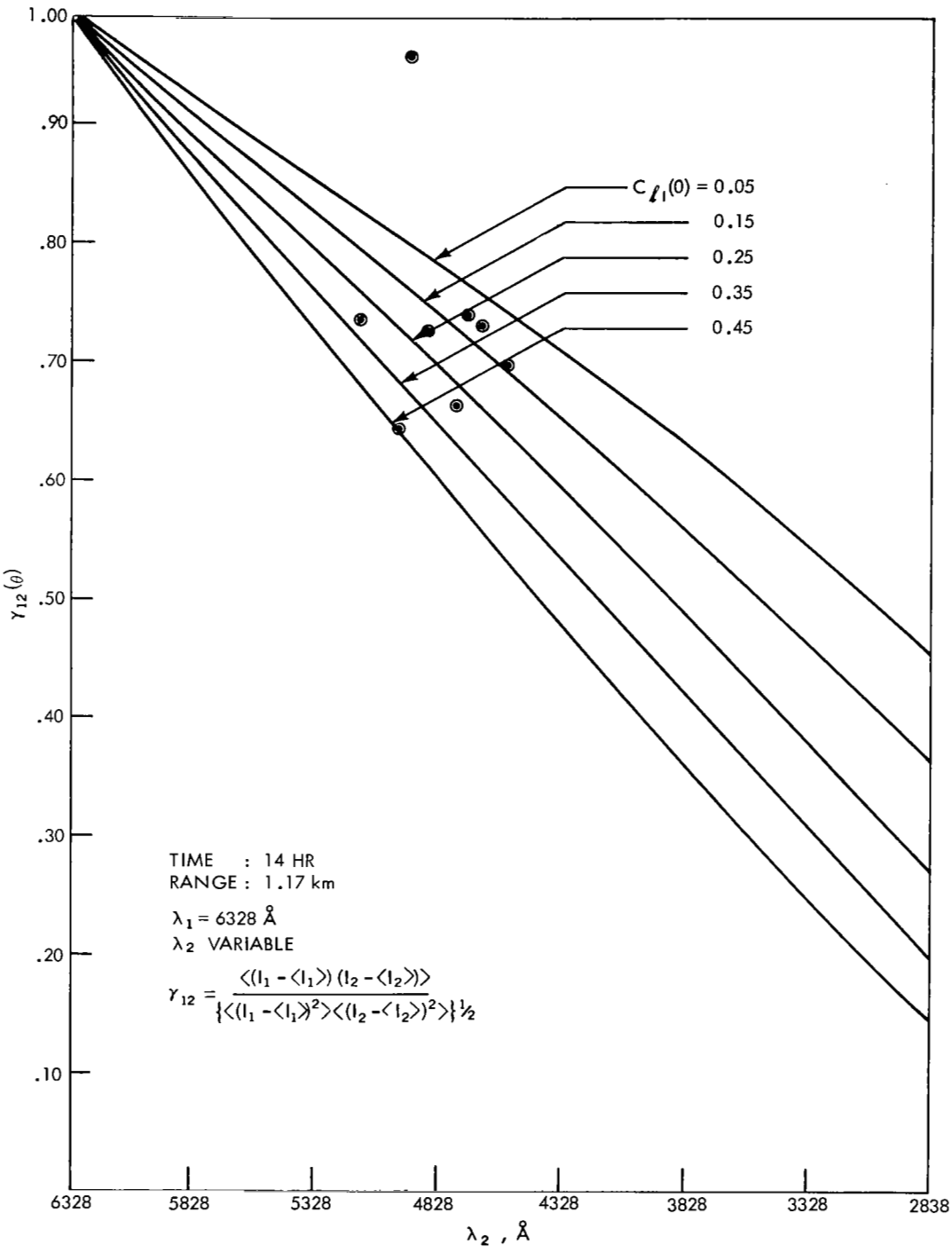

Figure 40. Experimental results, spectral correlation—run # 5, digital data reduction.

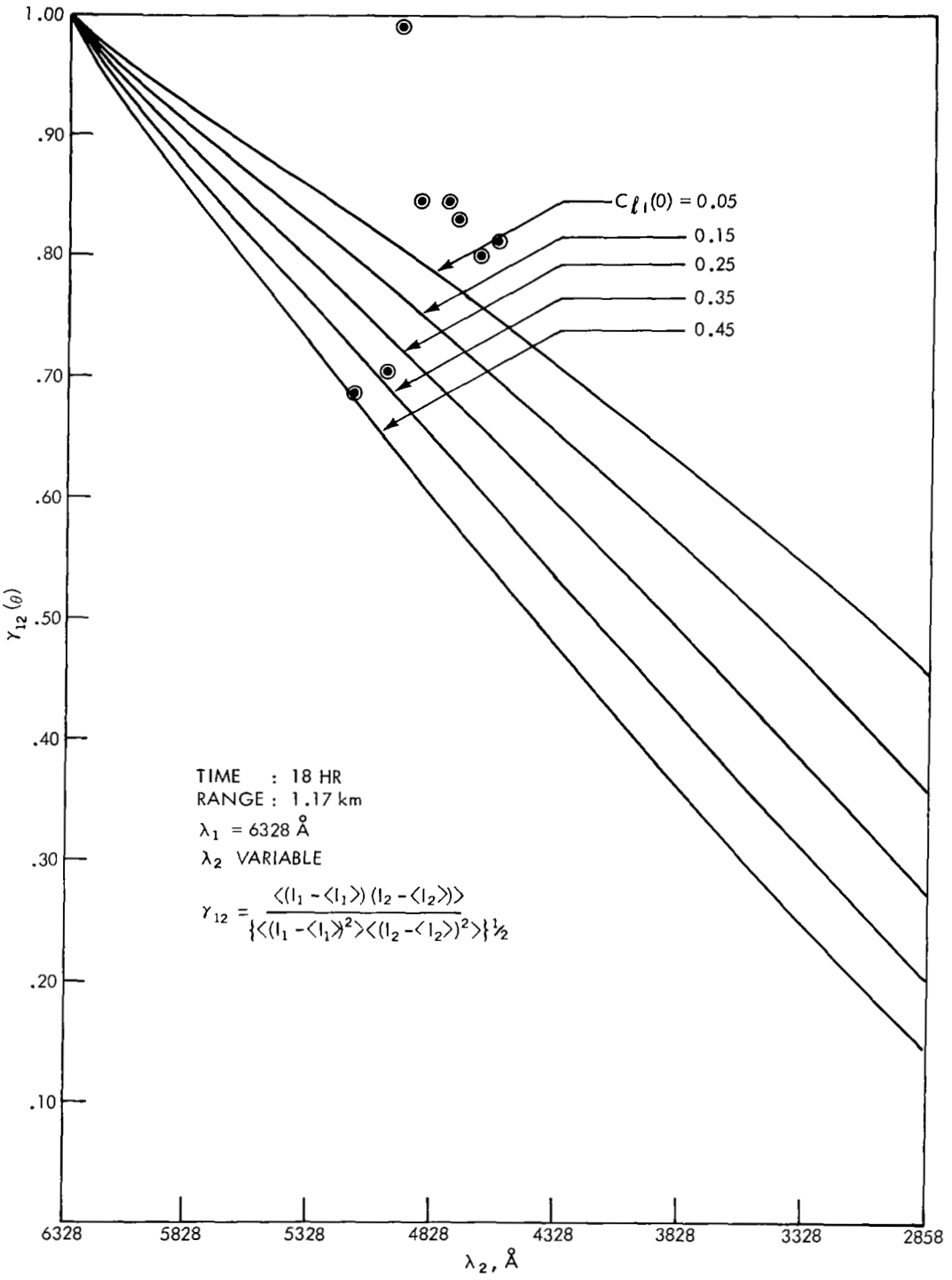

Figure 41. Experimental results, spectral correlation—run # 6, digital data reduction.

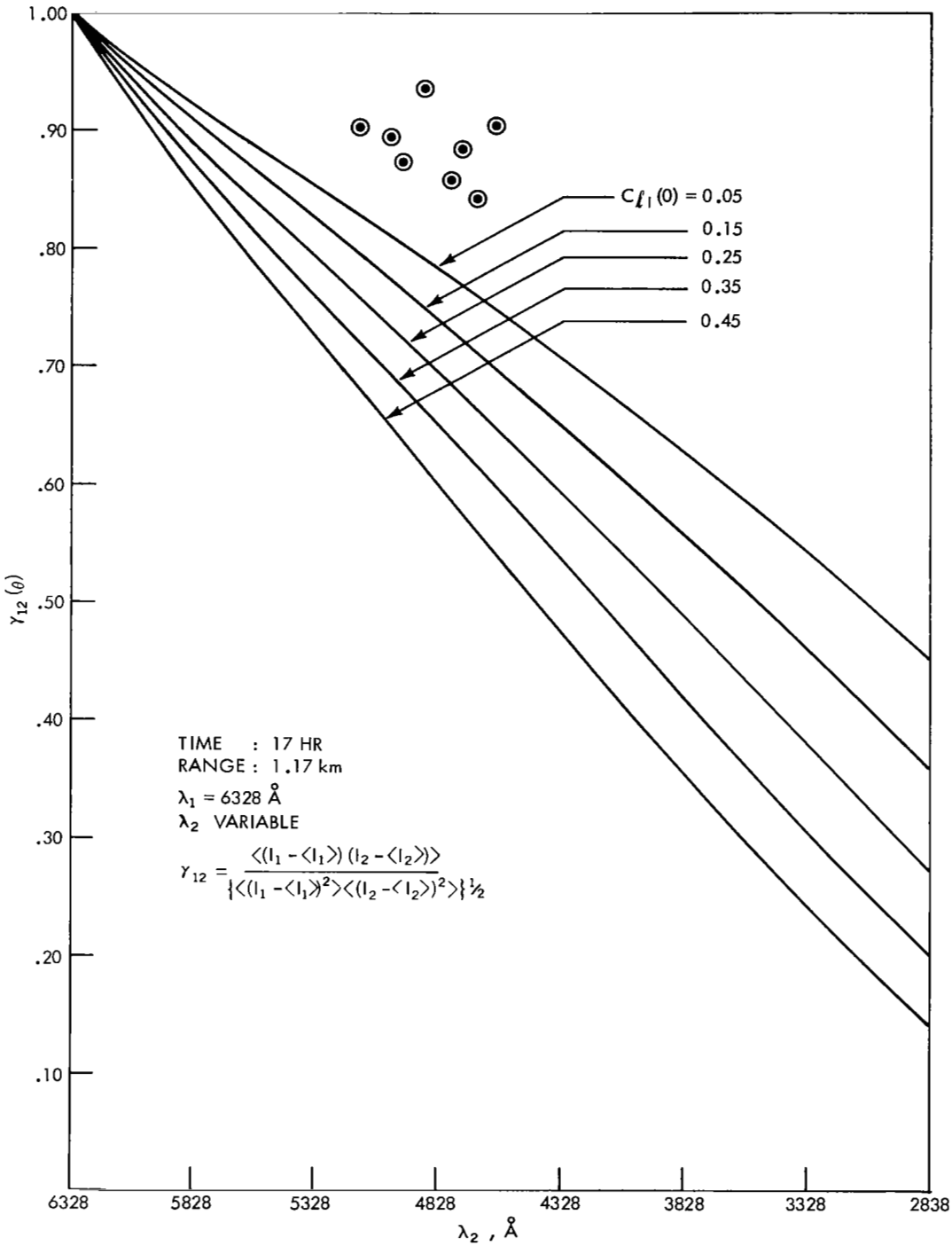

Figure 42. Experimental results, spectral correlation—run # 7, digital data reduction.

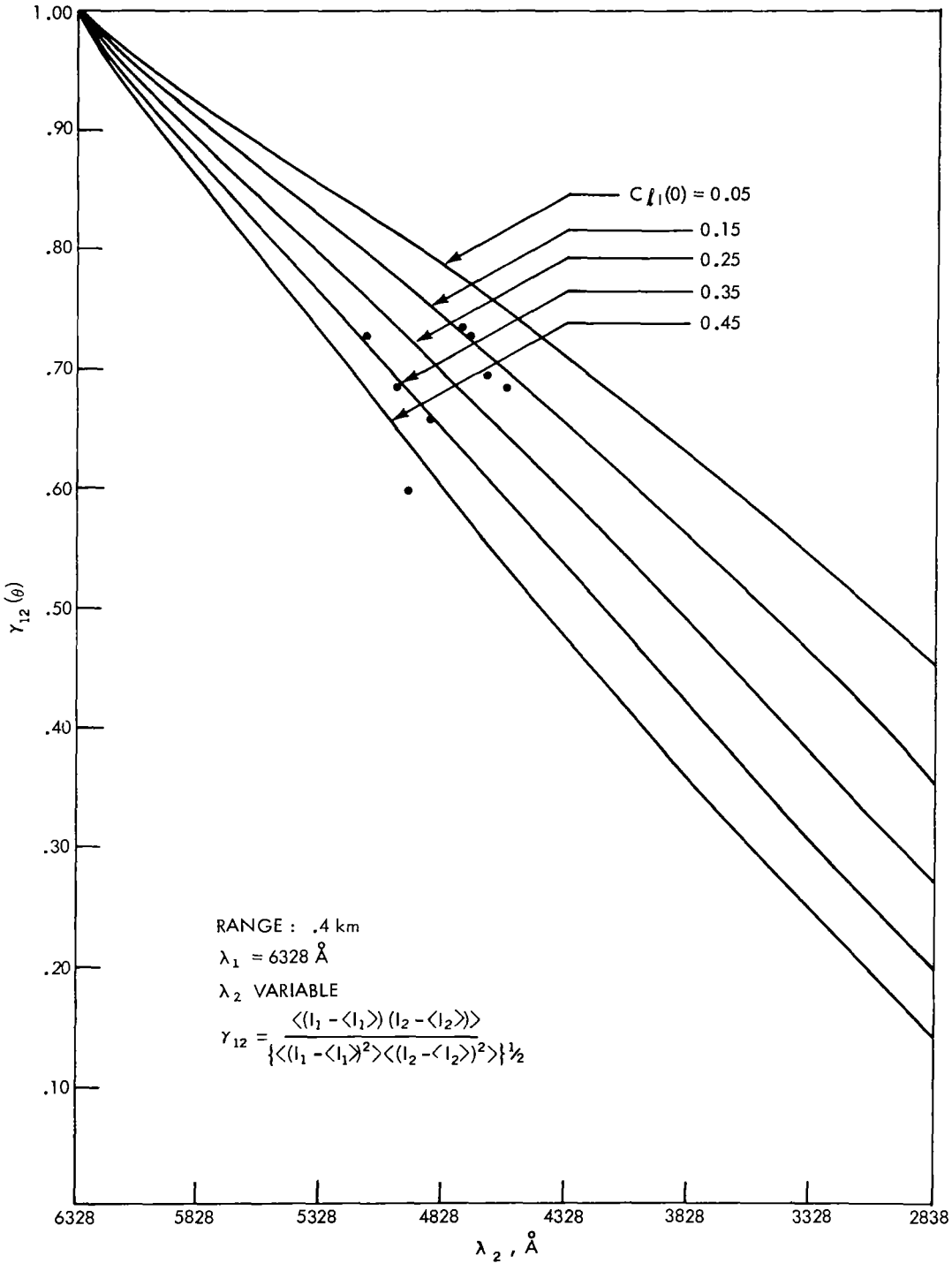

Figure 43. Mean experimental results, 0.4-km range.

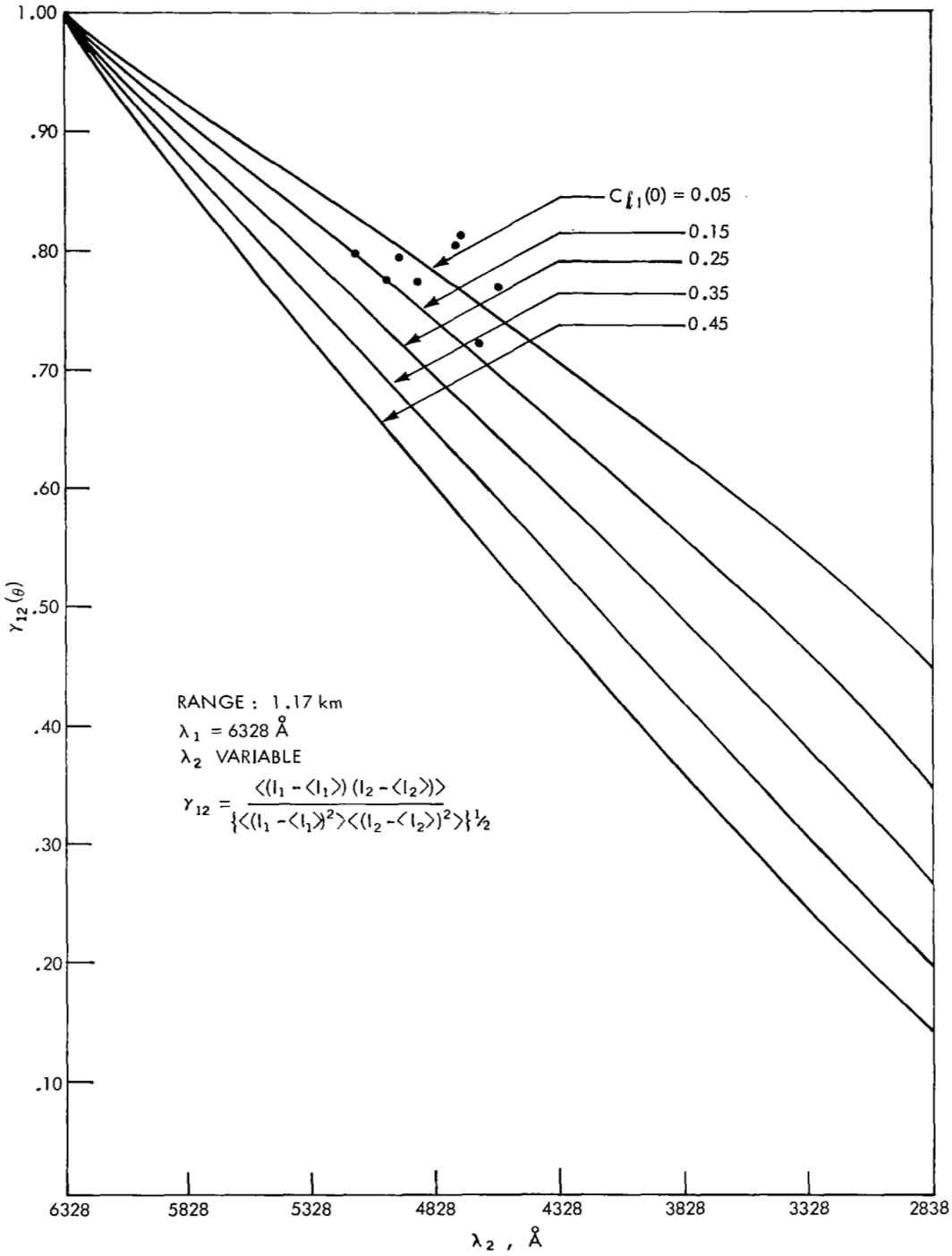

Figure 44. Mean experimental results, 1.17-km range.

was also evaluated for each data point in Figs. 36-42. In all cases $\gamma_{12}(\theta, \tau)$ was maximum for $\tau = 0$. We summarize spectral correlation as follows:

(1) The spectral correlation coefficient of log amplitude has been transformed to the irradiance domain in order to facilitate experiment-theory comparisons.

(2) Measurement of spectral correlation coefficients over 0.4- and 1.17-km horizontal paths has not shown any decrease in correlation in the wavelength range 5145 Å to 4579 Å.

(3) A typical value for the spectral correlation coefficient between 6328 Å and 5000 Å over a 1.17-km horizontal path is about 0.7.

2.5 Mean-Square Error and Chi-Square Testing of Irradiance Probability Density Functions

The form of the density function which describes the amplitude fluctuations of an optical wave has recently been questioned on both theoretical[65,101] and experimental[101,102] grounds. Previously, owing to work in the Soviet Union[2] and the United States,[70,103] the log-normal distribution had been accepted as accurately describing amplitude statistics. Recent discussions in the literature, however, have reflected a dissatisfaction with this result and have indicated that the Rayleigh or Rice distribution may be more accurate. In this section, the log-normal, Rayleigh, and Rice distributions are discussed and are compared with experimental data obtained with visible (0.488 μ) and infrared (10.6 μ) sources. The comparison between data and each of the three model distributions is carried out first through a mean-square error criterion (which emphasizes the modal region of the distribution) and secondly through a chi-square test (which

emphasizes the tails of the distribution). Each of the three distributions is discussed below so as to establish its basis in optical propagation theory.

a. Log-Normal Distribution. Following Tatarski (Ref. 2, Chap. 7), we consider a field E which is composed of an unscattered component

$$E_0 = A_0 \exp\left[jS_0\right]$$

and scattered components

$$E_k = A_k \exp\left[jS_k\right],$$

where the index k ranges over a large number of independent contributors. Therefore,

$$\frac{E}{E_0} = 1 + \sum_k \frac{E_k}{E_0}$$

and, for small fluctuations,

$$ln\,\frac{E}{E_0} = ln\left\{1 + \sum_k \frac{E_k}{E_0}\right\} \doteq \sum_k \frac{E_k}{E_0} . \qquad (125)$$

Considering the real part of Eq. 125, we have

$$ln\,\frac{A}{A_0} = \sum_k \frac{A_k}{A_0} \cos\left(S_k - S_0\right) . \qquad (126)$$

The left-hand side of Eq. 126 is the random variable log amplitude and, as the number of independent contributors (i.e., the range of k) becomes large, the Central Limit Theorem[104] dictates that the amplitude statistics become log-normal.*

Assuming Gaussian behavior for log amplitude, define its variance and mean as σ_ℓ^2 and μ_ℓ, respectively, and note the following relationships:

$$\text{(a)} \quad ln \frac{A}{A_0} = \frac{1}{2} ln \frac{I}{I_0} ,$$

$$\text{(b)} \quad \mu_\ell = - \sigma_\ell^2 , \tag{127}$$

and

$$\text{(c)} \quad \sigma_\ell^2 = \frac{1}{4} \ell n \left\{ \frac{\sigma_I^2}{I_0^2} + 1 \right\} .$$

Eqs. 127b and 127c follow from Eqs. 103 and 104, with σ_I^2 and I_0 being the variance and mean of irradiance, respectively.

Substituting Eqs. 127 into the Gaussian probability density function for log amplitude and transforming to irradiance quantities, we find the irradiance density g(I) to be

$$g(I) = \frac{1}{I\left(8\pi \sigma_\ell^2\right)^{1/2}} \exp\left[- \frac{1}{8\sigma_\ell^2} \left\{ ln \frac{I}{I_0} + 2\sigma_\ell^2 \right\}^2 \right] . \tag{128}$$

---

*Note that the imaginary part of Eq. 125 is

$$S - S_0 = \sum_k \frac{A_k}{A_0} \sin\left(S_k - S_0\right),$$

which implies a Gaussian behavior for the phase fluctuations when the range of k is large.

It is now clear that for log-normal-amplitude fluctuations the irradiance density can be evaluated by measuring the first two irradiance moments, solving for σ_ℓ^2 through Eq. 127c, and substituting the result into Eq. 128.

b. Rayleigh and Rice Distributions.[105] In this case the total field is composed of a coherent component A_0 and an incoherent component which is represented as a narrowband Gaussian process. That is,

$$E(t) = \left[A_0 + x(t)\right] \cos \omega_0 t - y(t) \sin \omega_0 t, \tag{129}$$

where x and y are independent Gaussian processes with

$$E[x] = E[y] = 0$$

and variance σ^2. Equation 129 can be rewritten as

$$E(t) = r \cos\left(\omega_0 t + \phi(t)\right), \tag{130}$$

where

$$r = \sqrt{\left(A_0 + x\right)^2 + y^2}$$

and

$$\phi = \tan^{-1}\left(\frac{y}{A_0 + x}\right).$$

The probability density for r is called the Rice distribution and is written[105]

$$Ri(r) = \frac{r}{\sigma^2} \exp\left[-\frac{\left(r^2 + A_0^2\right)}{2\sigma^2}\right] I_0\left(\frac{r A_0}{\sigma^2}\right), \tag{131}$$

where I_0 is the modified Bessel function of order zero. In the limiting case, as nearly all the energy is scattered, A_0 approaches zero and the probability density for r approaches the Rayleigh density Ra(r) written as

$$Ra(r) = \frac{r}{\sigma^2} \exp\left[-\frac{r^2}{2\sigma^2}\right] . \tag{132}$$

Using deWolf's[65] results, when the field amplitude is distributed according to Eq. 131, we can write the irradiance density Ri'(r) as

$$Ri'(r) = \frac{1}{I_0 - I_d} \exp\left[\frac{-(I + I_d)}{I_0 - I_d}\right] I_0\left[\frac{2\sqrt{I\, I_d}}{I_0 - I_d}\right], \tag{133}$$

where

$$I_0 = E[I]$$

and

$$I_d = I_0 \sqrt{2 - \frac{E[I^2]}{I_0^2}} .$$

When the specular component becomes vanishingly small, $I_d \to 0$ and the irradiance density becomes

$$Ra'(I) = \frac{1}{I_0} \exp\left[\frac{-I}{I_0}\right] . \tag{134}$$

The irradiance densities specified by Eqs. 133 and 134 will be respectively called the modified Rice and the modified Rayleigh in the remainder of this discussion.

As before, it should be clear that if the amplitude field is assumed Rice- or Rayleigh-distributed the corresponding irradiance density can be easily generated by measuring the first two moments of the irradiance fluctuations and substituting into Eq. 133 or Eq. 134.

In summary, the approach used here is to measure the first two moments of the experimental data, and using these numbers generate the three model distributions which would have been required in order to produce such experimental data. The three distributions are then tested to evaluate their compatibility with the measured density function.

c. Probability Density Tests. Let the model log-normal, Rayleigh, and Rice distributions which are synthesized from the data be called g(I), Ra' (I), and Ri' (I), respectively. Then the mean-square error (MSE) of the fit is

$$\frac{1}{N}\sum_{i=1}^{N}\left\{d(I_i) - g(I_i)\right\}^2 \equiv MSE_{LN},$$

$$\frac{1}{N}\sum_{i=1}^{N}\left\{d(I_i) - Ra'(I_i)\right\}^2 \equiv MSE_{Ra'}, \qquad (135)$$

and

$$\frac{1}{N}\sum_{i=1}^{N}\left\{d(I_i) - Ri'(I)\right\}^2 \equiv MSE_{Ri'},$$

where $d(I_i)$ is the experimentally measured density for the ith amplitude class and N is the total number of classes into which the fluctuating irradiance signal is partitioned. Clearly this test is not effective for evaluating the fit on the tails

of the distribution, since the quantity inside the bracket (Eq. 135) is always small in that region.

In order to test the tails of the distributions, the chi-square goodness-of-fit parameter is employed. The defining equations are

$$\chi^2_{LN} \equiv N\Delta I \sum_{i=1}^{N} \frac{\left\{d(I_i) - g(I_i)\right\}^2}{g(I_i)} ,$$

$$\chi^2_{Ra'} \equiv N\Delta I \sum_{i=1}^{N} \frac{\left\{d(I_i) - Ra'(I_i)\right\}^2}{Ra'(I_i)} , \tag{136}$$

and

$$\chi^2_{Ri'} \equiv N\Delta I \sum_{i=1}^{N} \frac{\left\{d(I_i) - Ri'(I_i)\right\}^2}{Ri'(I_i)} ,$$

where ΔI is the width of the amplitude class (assumed constant).

The tails of the distribution are emphasized by normalizing inside the summation by the model density. If the synthesized density is from the same family as the raw data, then it is well known[104,106] that, as the sample size becomes large, χ^2 takes on a chi-square density with N-1-S degrees of freedom, where S is the number of parameters of the model density which were estimated from the data sample. In this case, for any α the A can be evaluated which satisfies

$$P\left[\chi^2_{N-1-S} > A\right] = \alpha .$$

If we define the null hypothesis H_0, that the target population had a density belonging to the same family as the model distribution, then H_0 is rejected if χ^2_{N-1-S}

is greater than A and is accepted if H_0 is less than A. The rejection of H_0 when it is actually true is called a Type I error and has probability α. The accepting of H_0 when it is actually false is called a Type II error, but nothing definite can be concluded about its probability unless a particular form is assigned to the target density.

d. Experimental Analysis. Two types of experimental measurement will be analyzed in what follows. The only difference is in the type of optical source utilized. We first discuss the results obtained with a CO_2 laser radiating at 10.6μ and follow with the results obtained with an argon laser operating at 0.488μ.

The 10.6μ signal analysis is based on the same raw data that were used in Section 2.2 for log-amplitude variance analysis. However, it was apparent from the statistical analysis in Section 2.2 that longer time records would be required for density function estimation. A 40-second record was the maximum practical length for computerized processing. The amount of data available was seriously reduced because of frequent shifts in the laser output power. All the data were inspected on a chart recorder, and only those 40-second increments which were free from transmitter power fluctuations were analyzed. The detected irradiance signal (described in Section 2.2) was sampled at a 1-millisecond rate by an analog-to-digital converter and fed into a computer. The computer divided the amplitude range spanned by the signal into 200 evenly spaced classes. The probability density function d(I) and the first two moments were computed. These moments were then substituted into Eqs. 128, 133, and 134 in order to generate g(I), Ri'(I), and Ra'(I). The mean-square error calculation was then carried

by means of Eq. 135, and the chi-square calculation was performed by means of Eq. 136. The results are shown in Table XI.

TABLE XI

Mean-Square Error and Chi-Square Test Results of Weak-Scintillation Data ($\lambda = 10.6\,\mu$)

Data Record	Duration (sec)	Mean-Square Error			Chi-Square		
		MSE_{LN}	$MSE_{Ra'}$	$MSE_{Ri'}$	χ^2_{LN}	$\chi_{Ra'}$	$\chi_{Ri'}$
#1	40	0.247×10^{-1}	0.319×10^{1}	0.211×10^{-1}	0.243×10^{3}	0.252×10^{5}	0.139×10^{3}
#2	40	0.175×10^{-1}	0.260×10^{1}	0.250×10^{-1}	0.192×10^{3}	0.230×10^{5}	0.228×10^{3}
#3	40	0.899×10^{-1}	0.111×10^{2}	0.957×10^{-1}	0.179×10^{3}	0.252×10^{5}	0.182×10^{3}
#4	40	0.218	0.168×10^{2}	0.278	0.231×10^{3}	0.259×10^{5}	0.291×10^{3}
#5	40	0.184	0.903×10^{1}	0.127	0.866×10^{3}	0.255×10^{5}	0.341×10^{3}

In all cases the modified Rayleigh is a poor fit to the data. The log-normal and modified Rice appear nearly equally matched to the data from both a mean-square-error and a chi-square criterion. In Table XII, ratios of mean-square error and chi-square are shown for each record. Also shown is the measured scintillation statistic σ_I/I_0 for the experimental data. The average value of the mean-square error ratio is 1.01 and the average value of the chi-square ratio is 1.38.

The three model densities and the experimentally measured density for record #1 are shown in Fig. 45. Extra points are plotted near the mode where the data scatter is greatest. In places, the modified Rice is so close to the log-normal that they cannot be visually separated on a graph of this type. Table XIII is a portion of the computer printout for Record #2. Columns 6-8 are the

TABLE XII

Mean-Square Error and Chi-Square Ratio for Weak-Scintillation Data

Data Record	$(MSE_{LN}/MSE_{Ri'})$	$(\chi^2_{LN}/\chi^2_{Ri})$	σ_I/I_0
#1	1.17	1.75	0.119
#2	0.70	0.84	0.126
#3	0.94	0.98	0.086
#4	0.78	0.79	0.086
#5	1.45	2.54	0.095

cumulative distributions for the data, log-normal, and Rice densities. Columns 9 and 10 list the contributions to χ^2_{LN} and $\chi^2_{Ri'}$ from each of the 200 classes.

It is apparent that, under mild fluctuation conditions ($\sigma_I/I_0 \simeq 0.1$), the log-normal and Rice densities are very similar and are equally suitable for describing amplitude fluctuations.

The visible data were obtained over the 1.17-km path with the argon laser ($\lambda = 0.488\,\mu$) described earlier. The detector had a 1.0-mm aperture and produced a signal which was recorded on magnetic tape through an FM module. The signal level was biased so as to maximize the tape-recorder dynamic range (as described in Section 2.4a). The bias was subtracted from the data during the computer analysis. Essentially the same analysis was performed on these data as that just described for the CO_2 data. However, the interpretation of the results is more complicated, owing to problems caused by dynamic range limitation in the instrumentation. The fundamental problem is this: the signal which is analyzed by the computer is actually the sum of a noise signal (tape recorder noise, photomultiplier noise, etc.) and the desired irradiance signal. Considering

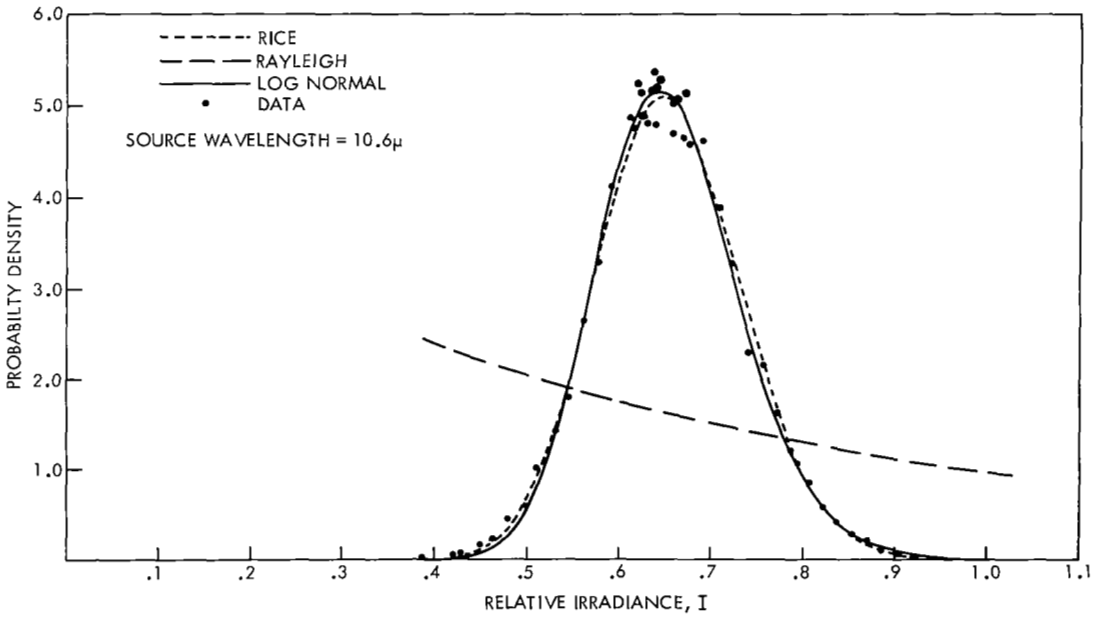

Figure 45. Synthesized log-normal and modified Rayleigh and Rice distributions for weak irradiance fluctuations. The normalized RMS irradiance fading $\left(\sigma_I / I_0\right)$ is 0.119.

Table XIII. Computer Results for Record #2 of the Weak-Scintillation Data

Computer results for record # 2 of the weak scintillation data.

1.	2.	3.	4.	5.	6.	7.	8.	9.	10.
I_i	$d(I_i)$	$g(I_i)$	$Rd(I_i)$	$Ri'(I_i)$	$\sum_i d(I_i)\,\Delta I$	$\sum_i g(I_i)\,\Delta I$	$\sum_i Ri'(I_i)\,\Delta I$	$\frac{N\Delta I\{d(I_i)-g(I_i)\}^2}{g(I_i)}$	$\frac{N\Delta I\{d(I_i)-Ri'(I_i)\}^2}{Ri'(I_i)}$
0.400E CC	0.734E-02	0.277E-02	0.230E 01	0.118E-01	0.250E-04	0.943E-05	0.402E-04	0.514E CC	0.123E 00
0.413E CC	0.724E-02	0.359E-02	0.229E 01	0.141E-01	0.500E-04	0.216E-04	0.857E-04	0.268E CC	0.233E 00
0.426E CC	0.0	0.453E-02	0.228E 01	0.168E-01	0.500E-04	0.373E-04	0.146E-03	0.314E CC	0.116E 01
0.439E CC	0.734E-02	0.560E-02	0.227E 01	0.200E-01	0.750E-04	0.574E-04	0.217E-03	0.248E-01	0.563E 00
0.452E CC	0.145E-01	0.736E-02	0.225E 01	0.237E-01	0.125E-03	0.828E-04	0.299E-03	0.474E CC	0.247E 00
0.465E CC	0.217E-01	0.929E-02	0.224E 01	0.279E-01	0.200E-03	0.115E-03	0.395E-03	0.115E 01	0.562E-01
0.478E CC	0.289E-01	0.114E-01	0.223E 01	0.328E-01	0.300E-03	0.155E-03	0.509E-03	0.178E 01	0.315E-01
0.491E CC	0.434E-01	0.145E-01	0.222E 01	0.384E-01	0.450E-03	0.208E-03	0.641E-03	0.398E 01	0.443E-01
0.504E CC	0.651E-01	0.180E-01	0.221E 01	0.449E-01	0.675E-03	0.287E-03	0.797E-03	0.854E 01	0.629E 00
0.517E CC	0.796E-01	0.222E-01	0.220E 01	0.523E-01	0.950E-03	0.344E-03	0.977E-03	0.103E 02	0.987E 00
0.530E CC	0.724E-02	0.271E-01	0.219E 01	0.607E-01	0.975E-03	0.438E-03	0.119E-02	0.101E 01	0.325E 01
0.543E CC	0.217E-01	0.331E-01	0.218E 01	0.702E-01	0.100E-02	0.555E-03	0.143E-02	0.276E CC	0.232E 01
0.556E CC	0.101E CC	0.401E-01	0.217E 01	0.810E-01	0.140E-02	0.695E-03	0.171E-02	0.646E 01	0.351E 00
0.569E CC	0.796E-01	0.483E-01	0.215E 01	0.932E-01	0.168E-02	0.867E-03	0.203E-02	0.140E 01	0.137E 00
0.582E CC	0.116E CC	0.580E-01	0.214E 01	0.107E 00	0.208E-02	0.106E-02	0.240E-02	0.398E 01	0.517E-01
0.595E CC	0.144E CC	0.692E-01	0.213E 01	0.122E 00	0.253E-02	0.130E-02	0.282E-02	0.372E 01	0.370E-01
0.608E CC	0.116E CC	0.822E-01	0.212E 01	0.139E 00	0.293E-02	0.158E-02	0.330E-02	0.948E CC	0.274E 00
0.621E CC	0.101E CC	0.972E-01	0.211E 01	0.158E 00	0.328E-02	0.192E-02	0.385E-02	0.132E 01	0.142E 01
0.634E CC	0.145E CC	0.114E 00	0.210E 01	0.179E 00	0.378E-02	0.231E-02	0.447E-02	0.588E CC	0.464E 00
0.647E CC	0.145E CC	0.134E 00	0.209E 01	0.203E 00	0.428E-02	0.277E-02	0.517E-02	0.646E 01	0.115E 01
0.660E CC	0.289E CC	0.156E 00	0.208E 01	0.229E 00	0.528E-02	0.331E-02	0.595E-02	0.787E 01	0.111E 01
0.673E CC	0.188E CC	0.181E 00	0.207E 01	0.257E 00	0.593E-02	0.394E-02	0.685E-02	0.165E 01	0.128E 01
0.686E CC	0.217E CC	0.208E 00	0.206E 01	0.288E 00	0.668E-02	0.466E-02	0.785E-02	0.196E 01	0.121E 01
0.699E CC	0.364E CC	0.241E 00	0.205E 01	0.322E 00	0.773E-02	0.555E-02	0.896E-02	0.114E 01	0.722E-01
0.712E CC	0.358E CC	0.276E 00	0.204E 01	0.359E 00	0.895E-02	0.645E-02	0.102E-01	0.154E 01	0.458E-02
0.725E CC	0.361E CC	0.315E 00	0.203E 01	0.400E 00	0.103E-01	0.754E-02	0.116E-01	0.126E 01	0.139E-01
0.738E CC	0.433E CC	0.358E 00	0.202E 01	0.443E 00	0.118E-01	0.877E-02	0.131E-01	0.731E CC	0.880E-01
0.751E CC	0.441E CC	0.406E 00	0.201E 01	0.491E 00	0.133E-01	0.102E-01	0.148E-01	0.224E CC	0.342E 00
0.764E CC	0.407E CC	0.457E 00	0.200E 01	0.542E 00	0.149E-01	0.118E-01	0.167E-01	0.256E-01	0.646E 00
0.777E CC	0.361E CC	0.514E CC	0.199E 01	0.596E 00	0.170E-01	0.136E-01	0.187E-01	0.111E 01	0.221E-02
0.513E CC	0.702E CC	0.575E CC	0.198E 01	0.655E 00	0.194E-01	0.155E-01	0.210E-01	0.153E 01	0.236E 00
0.516E CC	0.657E CC	0.642E 00	0.197E 01	0.717E 00	0.214E-01	0.177E-01	0.235E-01	0.422E CC	0.184E 01
0.520E CC	0.687E CC	0.713E 00	0.196E 01	0.784E 00	0.236E-01	0.202E-01	0.262E-01	0.561E CC	0.190E 01
0.523E CC	0.753E CC	0.789E 00	0.195E 01	0.854E 00	0.262E-01	0.229E-01	0.291E-01	0.115E CC	0.836E 00
0.527E CC	0.935E CC	0.871E 00	0.194E 01	0.929E 00	0.291E-01	0.259E-01	0.323E-01	0.810E-01	0.596E 00
0.530E CC	0.964E CC	0.958E 00	0.193E 01	0.101E 01	0.324E-01	0.292E-01	0.356E-01	0.755E-02	0.245E 00
0.534E CC	0.938E CC	0.105E 01	0.192E 01	0.109E 01	0.353E-01	0.329E-01	0.396E-01	0.313E 01	0.424E 01
0.537E CC	0.163E 01	0.115E 01	0.191E 01	0.118E 01	0.386E-01	0.368E-01	0.437E-01	0.868E CC	0.132E 01
0.540E CC	0.127E 01	0.125E 01	0.190E 01	0.127E 01	0.432E-01	0.412E-01	0.481E-01	0.152E-01	0.382E-03
0.544E CC	0.138E 01	0.136E 01	0.189E 01	0.136E 01	0.467E-01	0.458E-01	0.528E-01	0.577E 01	0.598E 01
0.547E CC	0.123E 01	0.147E 01	0.198E 01	0.146E 01	0.510E-01	0.509E-01	0.578E-01	0.268E 01	0.255E 01
0.551E CC	0.134E 01	0.159E 01	0.187E 01	0.157E 01	0.568E-01	0.564E-01	0.638E-01	0.166E 01	0.136E 01
0.554E CC	0.179E 01	0.170E 01	0.186E 01	0.167E 01	0.619E-01	0.623E-01	0.695E-01	0.276E CC	0.561E 00

Table XIII. (Continued)

0.6566E CC	0.1664E C1	0.1643E C1	0.1856E 01	0.1785E 01	0.6844E-01	0.6866E-C1	0.7516E-C1	0.1058E CC	0.3588E 00
0.6611E CC	0.1785E C1	0.1766E C1	0.1846E 01	0.1895E 01	0.7466E-01	0.7546E-C1	0.8176E-C1	0.1056E C1	0.4586E 00
0.6665E CC	0.1922E C1	0.1902E C1	0.1836E 01	0.2016E 01	0.8226E-01	0.8266E-C1	0.8866E-C1	0.6076E CC	0.1586E 01
0.6664E CC	0.2096E C1	0.2082E C1	0.1826E 01	0.2126E 01	0.9026E-01	0.9026E-C1	0.9606E-C1	0.1436E CC	0.8626E 00
0.6712E CC	0.2316E C1	0.2296E C1	0.1816E 01	0.2246E 01	0.9816E-01	0.9846E-C1	0.1046E CC	0.5666E-C1	0.1296E 00
0.6756E CC	0.2386E C1	0.2366E C1	0.1806E 01	0.2366E 01	0.1066E 00	0.1076E CC	0.1126E CC	0.3296E CC	0.8016E-02
0.6784E CC	0.2586E C1	0.2566E C1	0.1796E 01	0.2496E 01	0.1156E 00	0.1166E CC	0.1206E CC	0.1376E CC	0.1276E 00
0.6821E CC	0.2816E C1	0.2796E C1	0.1786E 01	0.2616E 01	0.1246E 00	0.1266E CC	0.1296E CC	0.6316E CC	0.7486E-03
0.6855E CC	0.2936E C1	0.2916E C1	0.1776E 01	0.2736E 01	0.1346E 00	0.1366E CC	0.1396E CC	0.2056E-C1	0.5806E 00
0.6896E CC	0.3166E C1	0.3146E C1	0.1766E 01	0.2866E 01	0.1456E 00	0.1466E CC	0.1496E CC	0.3546E CC	0.2246E 01
0.6932E CC	0.3316E C1	0.3296E C1	0.1756E 01	0.2986E 01	0.1566E 00	0.1576E CC	0.1596E CC	0.1316E-C1	0.6436E 00
0.6966E CC	0.3376E C1	0.3356E C1	0.1756E 01	0.3106E 01	0.1686E 00	0.1686E CC	0.1706E CC	0.9366E-C1	0.1606E 01
0.6996E CC	0.3536E C1	0.3446E C1	0.1746E 01	0.3226E 01	0.1796E 00	0.1806E CC	0.1816E CC	0.2256E CC	0.2316E 00
0.6603E CC	0.3776E C1	0.3756E C1	0.1736E 01	0.3346E 01	0.1926E 00	0.1936E CC	0.1956E CC	0.9576E CC	0.4006E 01
0.6606E CC	0.3956E C1	0.3936E C1	0.1726E 01	0.3466E 01	0.2056E 00	0.2056E CC	0.2046E CC	0.3676E CC	0.1436E 00
0.6610C CC	0.4086E C1	0.3986E C1	0.1716E 01	0.3586E 01	0.2196E 00	0.2196E CC	0.2176E CC	0.4056E C1	0.9506E 01
0.6613E CC	0.4216E C1	0.4126E C1	0.1706E 01	0.3696E 01	0.2326E 00	0.2326E CC	0.2306E CC	0.6026E CC	0.5856E-02
0.6616E CC	0.4376E C1	0.4036E C1	0.1706E 01	0.3796E 01	0.2456E 00	0.2466E CC	0.2436E CC	0.1076E C1	0.5326E-02
0.6620E CC	0.4386E C1	0.4176E C1	0.1696E 01	0.3906E 01	0.2606E 00	0.2606E CC	0.2566E CC	0.1036E C1	0.4096E 01
0.6623E CC	0.4496E C1	0.4236E C1	0.1696E 01	0.4006E 01	0.2756E 00	0.2756E CC	0.2706E CC	0.3706E-C2	0.1046E 01
0.6627E CC	0.4576E C1	0.4326E 01	0.1676E 01	0.4096E 01	0.2916E 00	0.2856E CC	0.2846E CC	0.1076E C1	0.3966E 01
0.6630E CC	0.4576E C1	0.4406E 01	0.1666E 01	0.4186E 01	0.3076E 00	0.3056E CC	0.2996E CC	0.4496E CC	0.2516E 01
0.6634E CC	0.4766E C1	0.4476E 01	0.1656E 01	0.4266E 01	0.3226E 00	0.3226E CC	0.3136E CC	0.1816E CC	0.1766E 00
0.6637E CC	0.4786E C1	0.4546E 01	0.1646E 01	0.4346E 01	0.3376E 00	0.3366E CC	0.3286E CC	0.4676E CC	0.1276E-01
0.6641E CC	0.4716E C1	0.4696E 01	0.1646E 01	0.4406E 01	0.3536E 00	0.3526E CC	0.3436E CC	0.1936E CC	0.1486E 01
0.6644E CC	0.4906E C1	0.4656E 01	0.1636E 01	0.4476E 01	0.3706E 00	0.3686E CC	0.3596E CC	0.5336E 00	0.2886E 01
0.6648E CC	0.4576E C1	0.4696E 01	0.1626E 01	0.4526E 01	0.3866E 00	0.3846E CC	0.3746E CC	0.2036E 00	0.4026E-01
0.6651E CC	0.4606E C1	0.4736E C1	0.1616E 01	0.4576E 01	0.4026E 00	0.4016E CC	0.3906E CC	0.2466E 00	0.9356E-02
0.6654E CC	0.4746E C1	0.4766E C1	0.1606E 01	0.4616E 01	0.4166E 00	0.4176E CC	0.4066E CC	0.1606E-C2	0.2506E 00
0.6658E CC	0.4786E C1	0.4776E 01	0.1606E 01	0.4646E 01	0.4346E 00	0.4336E CC	0.4226E CC	0.1106E-C2	0.2596E 00
0.6661E CC	0.4446E C1	0.4786E 01	0.1596E 01	0.4676E 01	0.4506E 00	0.4506E CC	0.4386E CC	0.1276E C1	0.5356E 00
0.6665E CC	0.5126E C1	0.4786E 01	0.1586E 01	0.4696E 01	0.4686E 00	0.4666E CC	0.4556E CC	0.1676E C1	0.2726E 01
0.6668E CC	0.4236E C1	0.4776E 01	0.1576E 01	0.4706E 01	0.4826E 00	0.4836E CC	0.4716E CC	0.4146E C1	0.3176E 01
0.6672E CC	0.4666E C1	0.4756E 01	0.1566E 01	0.4706E 01	0.4986E 00	0.4996E CC	0.4876E CC	0.1646E CC	0.3596E-01
0.6676E CC	0.4756E C1	0.4736E C1	0.1556E 01	0.4696E 01	0.5156E 00	0.5166E CC	0.5036E CC	0.5366E-C2	0.4366E-01
0.6679E CC	0.4476E C1	0.4706E C1	0.1556E 01	0.4686E 01	0.5306E 00	0.5326E CC	0.5196E CC	0.7886E CC	0.6736E 00
0.6682E CC	0.4416E C1	0.4666E C1	0.1546E 01	0.4666E 01	0.5456E 00	0.5486E CC	0.5356E CC	0.6776E CC	0.8846E 00
0.6686E CC	0.4786E C1	0.4616E C1	0.1536E 01	0.4636E 01	0.5626E 00	0.5646E CC	0.5516E CC	0.4066E CC	0.3216E 00
0.6689E CC	0.4766E C1	0.4566E C1	0.1526E 01	0.4596E 01	0.5786E 00	0.5806E CC	0.5676E CC	0.2676E CC	0.1586E 00
0.6692E CC	0.4236E C1	0.4506E 01	0.1526E 01	0.4556E 01	0.5936E 00	0.5956E CC	0.5816E CC	0.1156E C1	0.1616E 01
0.6696E CC	0.4366E C1	0.4436E C1	0.1516E 01	0.4506E 01	0.6086E 00	0.6116E CC	0.5956E CC	0.7666E-C1	0.2946E 00
0.6699E CC	0.3736E C1	0.4366E C1	0.1506E 01	0.4456E 01	0.6216E 00	0.6266E CC	0.6146E CC	0.6436E C1	0.8046E 01
0.7036E CC	0.4186E C1	0.4296E C1	0.1496E 01	0.4386E 01	0.6356E 00	0.6406E CC	0.6256E CC	0.3236E CC	0.8926E 00
0.7066E CC	0.4026E C1	0.4216E C1	0.1496E 01	0.4326E 01	0.6496E 00	0.6556E CC	0.6446E CC	0.6376E 01
0.7105E CC	0.4256E C1	0.4126E C1	0.1486E 01	0.4246E 01	0.6646E 00	0.6656E CC	0.6556E CC	0.4796E CC	0.3516E-01
0.7135E CC	0.3936E C1	0.4036E 01	0.1476E 01	0.4176E 01	0.6776E 00	0.6836E CC	0.6736E CC	0.1846E CC	0.9236E 00
0.7176E CC	0.3816E C1	0.3946E 01	0.1466E 01	0.4086E 01	0.6906E 00	0.6976E CC	0.6876E CC	0.3156E CC	0.1286E 01
0.7206E CC	0.3656E C1	0.3846E C1	0.1466E 01	0.4006E 01	0.7036E 00	0.7106E CC	0.6946E CC	0.2016E 01
0.7246E CC	0.3576E C1	0.3756E C1	0.1456E 01	0.3906E 01	0.7156E 00	0.7236E CC	0.7146E CC	0.5676E CC	0.2006E 01
0.7276E CC	0.3666E C1	0.3656E 01	0.1446E 01	0.3816E 01	0.7296E CC	0.7366E CC	0.7286E CC	0.5126E CC	0.5806E-01
0.7306E CC	0.3556E C1	0.3546E C1	0.1436E 01	0.3716E 01	0.7416E 00	0.7486E CC	0.7406E CC	0.4346E-C1	0.2786E 00
0.7346E CC	0.3626E C1	0.3446E C1	0.1436E 01	0.3616E 01	0.7546E 00	0.7606E CC	0.7556E CC	0.4126E CC	0.1676E-02
0.7376E CC	0.3166E C1	0.3336E C1	0.1426E 01	0.3516E 01	0.7656E 00	0.7716E CC	0.7656E CC	0.4126E CC	0.1566E 01

Table XIII. (Continued)

0.741E 00	0.370E 01	0.323E 01	0.141E 01	0.340E 01	0.775E 00	0.782E 00	0.777E 00	0.113E 01	0.333E 01
0.744E 00	0.366E 01	0.312E 01	0.140E 01	0.330E 01	0.785E 00	0.793E 00	0.788E 00	0.335E 00	0.188E 01
0.748E 00	0.341E 01	0.301E 01	0.140E 01	0.319E 01	0.796E 00	0.803E 00	0.799E 00	0.380E 00	0.468E-01
0.751E 00	0.318E 01	0.291E 01	0.139E 01	0.308E 01	0.807E 00	0.814E 00	0.810E 00	0.176E 01	0.216E 00
0.755E 00	0.295E 01	0.280E 01	0.138E 01	0.297E 01	0.817E 00	0.823E 00	0.820E 00	0.530E 00	0.147E-01
0.758E 00	0.303E 01	0.269E 01	0.138E 01	0.286E 01	0.828E 00	0.832E 00	0.830E 00	0.259E 01	0.713E 00
0.762E 00	0.256E 01	0.259E 01	0.137E 01	0.275E 01	0.837E 00	0.841E 00	0.839E 00	0.192E-01	0.906E 00
0.765E 00	0.255E 01	0.249E 01	0.136E 01	0.264E 01	0.845E 00	0.850E 00	0.849E 00	0.134E 00	0.206E 00
0.769E 00	0.239E 01	0.238E 01	0.136E 01	0.254E 01	0.854E 00	0.858E 00	0.857E 00	0.670E-03	0.597E 00
0.772E 00	0.234E 01	0.228E 01	0.135E 01	0.243E 01	0.862E 00	0.866E 00	0.866E 00	0.115E 00	0.205E 00
0.775E 00	0.224E 01	0.218E 01	0.134E 01	0.232E 01	0.870E 00	0.874E 00	0.874E 00	0.109E 00	0.192E 00
0.779E 00	0.234E 01	0.209E 01	0.133E 01	0.222E 01	0.878E 00	0.881E 00	0.881E 00	0.218E 01	0.473E 00
0.782E 00	0.235E 01	0.199E 01	0.133E 01	0.212E 01	0.886E 00	0.888E 00	0.889E 00	0.444E 01	0.176E 01
0.786E 00	0.196E 01	0.190E 01	0.132E 01	0.202E 01	0.893E 00	0.894E 00	0.896E 00	0.127E 00	0.115E 00
0.789E 00	0.198E 01	0.181E 01	0.131E 01	0.192E 01	0.899E 00	0.901E 00	0.902E 00	0.102E 01	0.104E 00
0.793E 00	0.174E 01	0.173E 01	0.131E 01	0.183E 01	0.905E 00	0.907E 00	0.909E 00	0.540E-02	0.303E 00
0.796E 00	0.191E 01	0.164E 01	0.130E 01	0.173E 01	0.912E 00	0.912E 00	0.915E 00	0.120E 01	0.225E 00
0.800E 00	0.161E 01	0.156E 01	0.129E 01	0.164E 01	0.917E 00	0.918E 00	0.920E 00	0.135E 00	0.383E-01
0.803E 00	0.170E 01	0.148E 01	0.129E 01	0.156E 01	0.923E 00	0.923E 00	0.926E 00	0.229E 01	0.924E 00
0.806E 00	0.125E 01	0.140E 01	0.128E 01	0.147E 01	0.927E 00	0.928E 00	0.931E 00	0.112E 01	0.226E 01
0.810E 00	0.146E 01	0.133E 01	0.128E 01	0.139E 01	0.932E 00	0.932E 00	0.936E 00	0.921E 00	0.256E 00
0.813E 00	0.151E 01	0.126E 01	0.127E 01	0.131E 01	0.938E 00	0.937E 00	0.940E 00	0.357E 01	0.214E 01
0.817E 00	0.122E 01	0.119E 01	0.126E 01	0.124E 01	0.942E 00	0.941E 00	0.944E 00	0.414E-01	0.219E-01
0.820E 00	0.114E 01	0.112E 01	0.126E 01	0.116E 01	0.946E 00	0.945E 00	0.948E 00	0.249E-01	0.206E-01
0.824E 00	0.124E 01	0.106E 01	0.125E 01	0.109E 01	0.950E 00	0.948E 00	0.952E 00	0.205E 01	0.134E 01
0.827E 00	0.977E 00	0.100E 01	0.124E 01	0.103E 01	0.954E 00	0.952E 00	0.956E 00	0.360E-01	0.158E 00
0.831E 00	0.105E 01	0.942E 00	0.124E 01	0.961E 00	0.957E 00	0.955E 00	0.959E 00	0.845E 00	0.561E 00
0.834E 00	0.663E 00	0.887E 00	0.123E 01	0.900E 00	0.960E 00	0.958E 00	0.962E 00	0.118E-02	0.222E-01
0.838E 00	0.911E 00	0.834E 00	0.122E 01	0.842E 00	0.963E 00	0.961E 00	0.965E 00	0.461E-01	0.794E-01
0.841E 00	0.883E 00	0.784E 00	0.122E 01	0.786E 00	0.966E 00	0.964E 00	0.968E 00	0.844E 00	0.819E 00
0.844E 00	0.760E 00	0.735E 00	0.121E 01	0.734E 00	0.969E 00	0.966E 00	0.970E 00	0.530E-01	0.648E-01
0.848E 00	0.702E 00	0.691E 00	0.121E 01	0.684E 00	0.971E 00	0.968E 00	0.973E 00	0.128E-01	0.340E-01
0.851E 00	0.738E 00	0.647E 00	0.120E 01	0.636E 00	0.974E 00	0.971E 00	0.975E 00	0.877E 00	0.112E 01
0.855E 00	0.637E 00	0.607E 00	0.119E 01	0.592E 00	0.976E 00	0.973E 00	0.977E 00	0.104E 00	0.238E 00
0.858E 00	0.593E 00	0.568E 00	0.119E 01	0.550E 00	0.978E 00	0.975E 00	0.979E 00	0.801E-01	0.241E 00
0.862E 00	0.521E 00	0.531E 00	0.118E 01	0.510E 00	0.980E 00	0.977E 00	0.981E 00	0.130E-01	0.175E-01
0.865E 00	0.475E 00	0.496E 00	0.118E 01	0.472E 00	0.981E 00	0.978E 00	0.982E 00	0.466E-01	0.397E-02
0.868E 00	0.444E 00	0.464E 00	0.117E 01	0.437E 00	0.983E 00	0.980E 00	0.984E 00	0.726E-01	0.281E-02
0.872E 00	0.470E 00	0.433E 00	0.116E 01	0.404E 00	0.984E 00	0.981E 00	0.985E 00	0.229E 00	0.747E 00
0.876E 00	0.492E 00	0.403E 00	0.116E 01	0.373E 00	0.986E 00	0.983E 00	0.986E 00	0.135E 01	0.261E 01
0.879E 00	0.366E 00	0.376E 00	0.115E 01	0.344E 00	0.987E 00	0.984E 00	0.988E 00	0.215E 01	0.118E 01
0.882E 00	0.311E 00	0.350E 00	0.115E 01	0.317E 00	0.988E 00	0.985E 00	0.989E 00	0.256E 00	0.837E-02
0.886E 00	0.276E 00	0.326E 00	0.114E 01	0.292E 00	0.989E 00	0.986E 00	0.990E 00	0.543E 00	0.168E 01
0.889E 00	0.223E 00	0.303E 00	0.113E 01	0.269E 00	0.990E 00	0.987E 00	0.991E 00	0.116E 01	0.352E 00
0.893E 00	0.186E 00	0.281E 00	0.113E 01	0.247E 00	0.991E 00	0.988E 00	0.992E 00	0.214E 01	0.958E 00
0.896E 00	0.154E 00	0.261E 00	0.112E 01	0.226E 00	0.991E 00	0.989E 00	0.992E 00	0.276E 01	0.137E 01
0.900E 00	0.246E 00	0.243E 00	0.112E 01	0.207E 00	0.992E 00	0.990E 00	0.993E 00	0.344E-02	0.499E 00
0.903E 00	0.166E 00	0.225E 00	0.111E 01	0.190E 00	0.993E 00	0.991E 00	0.994E 00	0.416E 00	0.105E-02
0.907E 00	0.217E 00	0.209E 00	0.111E 01	0.174E 00	0.994E 00	0.992E 00	0.994E 00	0.245E-01	0.752E 00
0.910E 00	0.161E 00	0.193E 00	0.110E 01	0.159E 00	0.994E 00	0.992E 00	0.995E 00	0.633E-01	0.217E 00
0.914E 00	0.941E-01	0.179E 00	0.109E 01	0.145E 00	0.995E 00	0.993E 00	0.995E 00	0.277E 01	0.122E 01
0.917E 00	0.866E-01	0.165E 00	0.109E 01	0.132E 00	0.996E 00	0.994E 00	0.996E 00	0.256E 01	0.107E 01
0.920E 00	0.123E 00	0.153E 00	0.108E 01	0.120E 00	0.995E 00	0.994E 00	0.996E 00	0.403E 00	0.461E-02

Table XIII. (Concluded)

0.9224	00	0.1146	00	0.1416	00	0.1086	01	0.1096	00	0.9966	00	0.9966	00	0.9976	00	0.3176	00	0.2656-01
0.9276	00	0.5466-01		0.1306	00	0.1076	01	0.9946-01		0.9966	00	0.9966	00	0.9976	00	0.1016	01	0.1096	00
0.9316	00	0.1016	00	0.1206	00	0.1076	01	0.9026-01		0.9966	00	0.9966	00	0.9976	00	0.2066	00	0.9456-01
0.9346	00	0.7966-01		0.1116	00	0.1066	01	0.8186-01		0.9976	00	0.9966	00	0.9976	00	0.6146	00	0.4076-02
0.9366	00	0.6756-01		0.1026	00	0.1066	01	0.7416-01		0.9976	00	0.9966	00	0.9966	00	0.1336	01	0.2456 00
0.9416	00	0.5616-01		0.9436-01		0.1056	01	0.6716-01		0.9976	00	0.9966	00	0.9966	00	0.6236	00	0.3526-02
0.9446	00	0.4766-01		0.8686-01		0.1066	01	0.6076-01		0.9976	00	0.9976	00	0.9986	00	0.1666	00	0.1566 00
0.9486	00	0.4016-01		0.7996-01		0.1046	01	0.5486-01		0.9986	00	0.9976	00	0.9986	00	0.1886	00	0.1356 00
0.9526	00	0.3376-01		0.7356-01		0.1036	01	0.4956-01		0.9986	00	0.9976	00	0.9996	00	0.2266	00	0.9946-01
0.9566	00	0.2846-01		0.6756-01		0.1036	01	0.4466-01		0.9986	00	0.9986	00	0.9996	00	0.1496	00	0.1906 01
0.9606	00	0.2406-01		0.6206-01		0.1026	01	0.4026-01		0.9986	00	0.9986	00	0.9996	00	0.1226	01	0.2176 00
0.9646	00	0.2026-01		0.5706-01		0.1026	01	0.3616-01		0.9986	00	0.9986	00	0.9996	00	0.1036-02		0.9046 00
0.9686	00	0.1696-01		0.5236-01		0.1016	01	0.3266-01		0.9996	00	0.9986	00	0.9996	00	0.3526-02		0.7026 00
0.9726	00	0.1426-01		0.4806-01		0.1016	01	0.2926-01		0.9996	00	0.9986	00	0.9996	00	0.2976-01		0.4806 00
0.9766	00	0.1206-01		0.4406-01		0.1006	01	0.2626-01		0.9996	00	0.9986	00	0.9996	00	0.3556	00	0.2016-01
0.9796	00	0.1046-01		0.4036-01		0.9996	00	0.2356-01		0.9996	00	0.9996	00	0.9996	00	0.1146	01	0.2386 00
0.9796	00	0.7366-02		0.3696-01		0.9946	00	0.2106-01		0.9996	00	0.9996	00	0.9996	00	0.3416	01	0.1136 02
0.9836	00	0.3176-01		0.3386-01		0.9896	00	0.1886-01		0.9996	00	0.9996	00	0.9996	00	0.2986	00	0.3106-01
0.9866	00	0.3256-01		0.3106-01		0.9846	00	0.1686-01		0.9996	00	0.9996	00	0.1006	01	0.8716-02		0.6056 00
0.9901	00	0.2176-01		0.2836-01		0.9796	00	0.1506-01		0.9996	00	0.9996	00	0.1006	01	0.1056	00	0.2066 00
0.9936	00	0.1456-01		0.2606-01		0.9746	00	0.1346-01		0.9996	00	0.9996	00	0.1006	01	0.3466	00	0.6006-02
0.9966	00	0.7246-02		0.2366-01		0.9696	00	0.1196-01		0.9996	00	0.9996	00	0.1006	01	0.7656	00	0.1286 00
0.1006	01	0.7246-02		0.2166-01		0.9646	00	0.1066-01		0.9996	00	0.9996	00	0.1006	01	0.6556	00	0.7506-01
0.1009	01	0.2896-01		0.1976-01		0.9596	00	0.9466-02		0.1006	01	0.9996	00	0.1006	01	0.3006	00	0.2776 01
0.1013	01	0.2		0.1806-01		0.9546	00	0.8416-02		0.1006	01	0.9996	00	0.1006	01	0.1246	01	0.5816 00
0.1016	01	0.7246-02		0.1646-01		0.9496	00	0.7476-02		0.1006	01	0.9996	00	0.1006	01	0.3546	00	0.5056-03
0.1019	01	0.2176-01		0.1496-01		0.9446	00	0.6636-02		0.1006	01	0.1006	01	0.1006	01	0.2116	00	0.2376 01
0.1023	01	0.7246-02		0.1356-01		0.9406	00	0.5896-02		0.1006	01	0.1006	01	0.1006	01	0.2076	00	0.2186-01
0.1026	01	0.7246-02		0.1246-01		0.9356	00	0.5216-02		0.1006	01	0.1006	01	0.1006	01	0.1496	00	0.5476-01
0.1029	01	0.2176-01		0.1136-01		0.9306	00	0.4616-02		0.1006	01	0.1006	01	0.1006	01	0.6626	00	0.4396 01
0.1033	01	0.7		0.1036-01		0.9256	00	0.4076-02		0.1006	01	0.1006	01	0.1006	01	0.7116	00	0.2816 00
0.1036	01	0.2176-01		0.9366-02		0.9216	00	0.3606-02		0.1006	01	0.1006	01	0.1006	01	0.1136	01	0.6306 01
0.1039	01	0.0		0.8516-02		0.9166	00	0.3186-02		0.1006	01	0.1006	01	0.1006	01	0.5686	00	0.2206 00
0.1043	01	0.7246-02		0.7746-02		0.9116	00	0.2806-02		0.1006	01	0.1006	01	0.1006	01	0.2246-02		0.4856 00
0.1046	01	0.0		0.7036-02		0.9076	00	0.2476-02		0.1006	01	0.1006	01	0.1006	01	0.4666	00	0.1716 00
0.1049	01	0.0		0.6396-02		0.9026	00	0.2176-02		0.1006	01	0.1006	01	0.1006	01	0.4416	00	0.1506 00
0.1053	01	0.7246-02		0.5806-02		0.8976	00	0.1916-02		0.1006	01	0.1006	01	0.1006	01	0.2466-01		0.1026 01
0.1056	01	0.0		0.5276-02		0.8936	00	0.1686-02		0.1006	01	0.1006	01	0.1006	01	0.3646	00	0.1166 00
0.1066	01	0.0		0.4786-02		0.8886	00	0.1486-02		0.1006	01	0.1006	01	0.1006	01	0.3336	00	0.1026 00
0.1066	01	0.0		0.4336-02		0.8846	00	0.1306-02		0.1006	01	0.1006	01	0.1006	01	0.2956	00	0.8556-01
0.1066	01	0.0		0.3916-02		0.8796	00	0.1146-02		0.1006	01	0.1006	01	0.1006	01	0.2716	00	0.7856-01
0.1076	01	0.0		0.3566-02		0.8756	00	0.9956-03		0.1006	01	0.1006	01	0.1006	01	0.2466	00	0.6876-01
0.1076	01	0.0		0.3236-02		0.8716	00	0.8716-03		0.1006	01	0.1006	01	0.1006	01	0.2236	00	0.6026-01
0.1076	01	0.0		0.2926-02		0.8666	00	0.7616-03		0.1006	01	0.1006	01	0.1006	01	0.2026	00	0.5266-01
0.1086	01	0.0		0.2656-02		0.8626	00	0.6656-03		0.1006	01	0.1006	01	0.1006	01	0.1836	00	0.4606-01
0.1086	01	0.0		0.2406-02		0.8576	00	0.5816-03		0.1006	01	0.1006	01	0.1006	01	0.1656	00	0.4016-01
0.1086	01	0.0		0.2176-02		0.8536	00	0.5076-03		0.1006	01	0.1006	01	0.1006	01	0.1506	00	0.3506-01
0.1096	01	0.0		0.1956-02		0.8496	00	0.4426-03		0.1006	01	0.1006	01	0.1006	01	0.1356	00	0.3056-01
0.1096	01	0.0		0.1776-02		0.8446	00	0.3866-03		0.1006	01	0.1006	01	0.1006	01	0.1226	00	0.2666-01
0.1096	01	0.0		0.1606-02		0.8406	00	0.3356-03		0.1006	01	0.1006	01	0.1006	01	0.1116	00	0.2316-01
0.1106	01	0.1456-01		0.1456-02		0.8366	00	0.2916-03		0.1006	01	0.1006	01	0.1006	01	0.8106	01	0.4776 02

the noise and irradiance signals independent, we conclude that the probability density of the composite signal is a convolution of the individual densities associated with the noise and irradiance signals. When the irradiance fluctuations are strong, there is a significant amount of time when the irradiance value is near zero. When the noise is summed with these near-zero values, the resultant frequently takes on negative values. In order to compensate for these physically impossible "negative irradiance" values, the $d(I_i)$, $i = 1, 2, \ldots 200$, as printed out by the computer, was shifted so that $d(I_1)$ was assigned to the first positive class, $d(I_2)$ was assigned to the second positive class, etc.

An additional problem area was that the tape recorder noise was not a constant but depended on the signal level being recorded. A calibration sequence consisting of a plus, zero, and minus DC voltage was recorded on the magnetic tape just prior to each data run. During data analysis, the variance associated with each of these levels was analyzed so as to evaluate the tape-recorder noise at each record level. In this experiment the negative calibration was very near the zero irradiance level for the system, and therefore it was this noise level which was important. For chi-square calculations, it was noted that the first few classes of the irradiance density (which were seriously contaminated by the noise) were dominating the chi-square value for each of the three model densities. For this reason, the first two or three classes (depending on the measured noise) were omitted from the chi-square calculation in all cases.

The results of 23 data runs of 20-seconds length are shown in Table XIV. The standard deviation divided by the mean irradiance is also listed for each record. Note that when σ_I/I_0 is greater than 1, it is not possible to generate

TABLE XIV

Mean-Square Error and Chi-Square Test Results for Strong-Scintillation Data ($\lambda = 0.488\mu$)

Data Record	MSE_{LN}	$MSE_{Ra'}$	$MSE_{Ri'}$	χ^2_{LN}	$\chi^2_{Ra'}$	$\chi^2_{Ri'}$	σ_I I_0
#1	0.304×10^{-2}	0.249	0.178	275	3,134	3,090	0.885
2	0.413×10^{-2}	0.273	0.161	286	3,053	3,080	0.843
3	0.152×10^{-1}	0.401	0.295	389	3,470	4,180	0.885
4	0.116×10^{-1}	0.358	0.269	413	3,753	10,810	0.892
5	0.286×10^{-1}	0.552	0.333	461	4,064	195,000	0.833
6	0.263×10^{-1}	0.829	0.416	460	4,415	8,900	0.800
7	0.240×10^{-1}	0.648	0.362	461	4,743	17,300	0.823
8	0.160×10^{-1}	0.527	0.276	410	4,480	625,000	0.812
9	0.369×10^{-1}	0.439	0.420	645	4,800	6,840	0.970
10	0.266×10^{-1}	0.389	-	454	3,870	-	1.005
11	0.851×10^{-2}	0.554	0.257	273	3,265	2,710	0.806
12	0.113×10^{-1}	0.697	0.238	310	5,917	13,100	0.732
13	0.440×10^{-2}	0.447	0.158	313	4,368	4,118	0.762
14	0.400×10^{-2}	0.426	0.191	280	4,037	5,222	0.79
15	0.220×10^{-1}	0.378	0.310	601	4,150	5,775	0.915
16	0.209×10^{-1}	0.322	-	518	3,427	-	1.01
17	0.203×10^{-1}	0.440	0.273	566	4,837	9,000	0.838
18	0.740×10^{-2}	0.378	0.227	309	3,785	15,540	0.840
19	0.220×10^{-1}	0.360	0.319	527	3,647	4,810	0.940
20	0.105×10^{-1}	0.354	0.307	297	2,843	4,830	0.935
21	0.190×10^{-1}	0.394	0.342	434	3,303	5,450	0.932
22	0.118×10^{-1}	0.416	0.279	306	3,009	5,254	0.865
23	0.128×10^{-1}	0.710	0.369	287	3,514	2,100	0.815

a Rice density using deWolf's results (see Eq. 133). The results show that in all cases the log-normal density is a better fit to the data from both a mean-square-error and chi-square criterion. Fig. 46 plots the ratio of mean-square errors for the modified Rayleigh and log-normal distributions versus strength of the irradiance fluctuations (σ_I/I_0). The ratio decreases substantially as the fluctuations grow stronger, but there is still an order-of-magnitude difference for very strong fluctuations. Fig. 47 plots the MSE ratio for the modified Rice and log-normal distributions and shows the inadequacy of the former. The value of the log-normal MSE is shown in Fig. 48, and no clear trend is evident. Corresponding plots for the three chi-square values are shown in Figs. 49-51. These graphs also show clearly that the log-normal distribution is a much better fit to the data than the other models used. The three synthesized densities and the data of data record 5 (Table XIV) in Fig. 52. Every class value of the data is plotted up to $I = 0.2$, and above this value only every fifth class is shown (for clarity purposes). A typical computer printout (data record #3) is shown in Table XV. The column headings are identical with those of Table XIII except for 8. and 10., which now pertain to the modified Rayleigh density. The first two classes were omitted from the chi-square calculation, owing to the noise problem discussed previously.

Neither the CO_2 data nor the argon data have been discussed up to this point from the standpoint of hypothesis testing. In Table XVI are listed the percentage points of the chi-square distribution for 200 degrees of freedom.* So it should be

*The A values for 198 or 199 degrees of freedom are not significantly different from those listed in Table XVI.

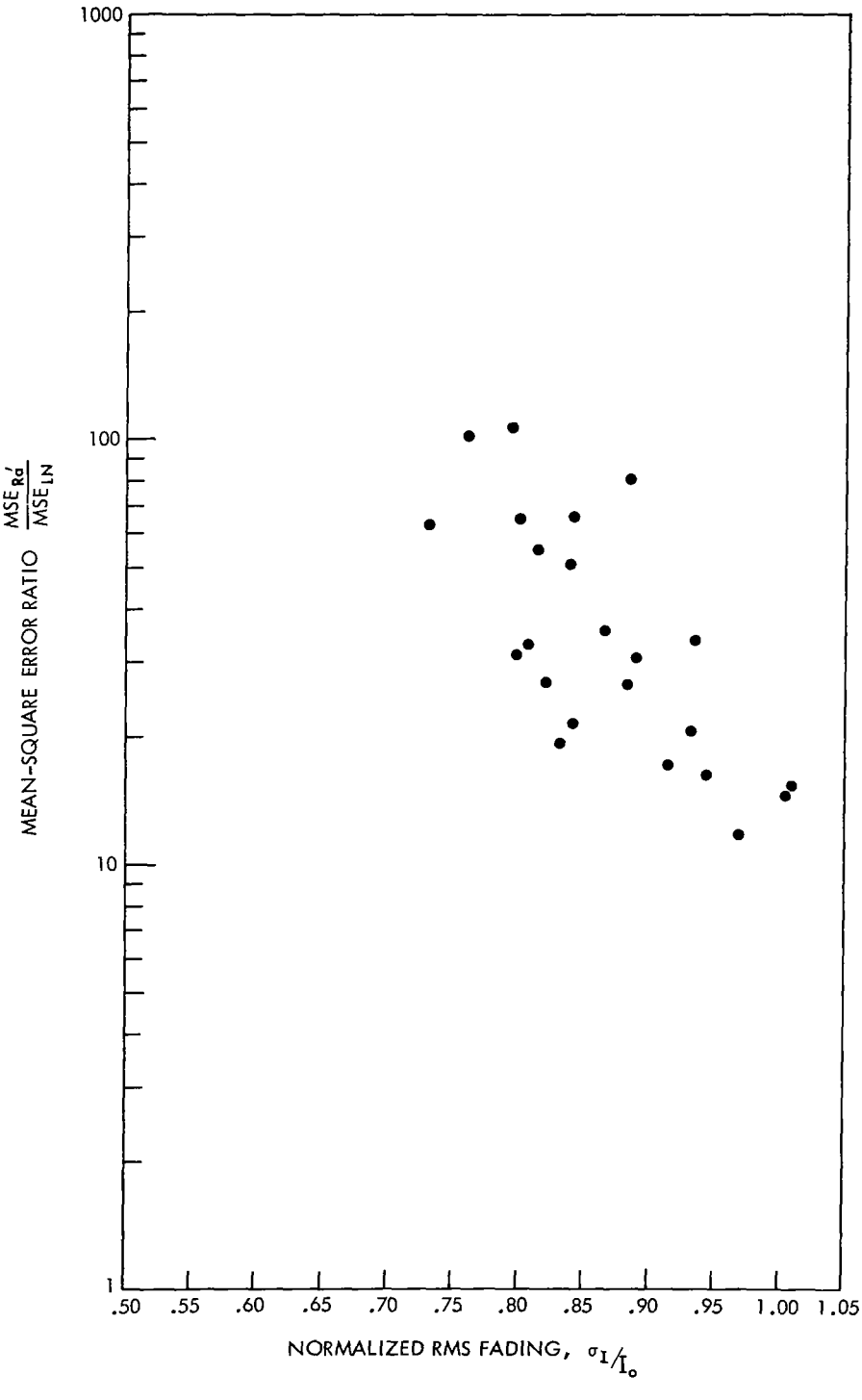

Figure 46. Mean-square error ratio for the modified Rayleigh and log-normal distributions as a function of RMS fading, σ_I / I_0.

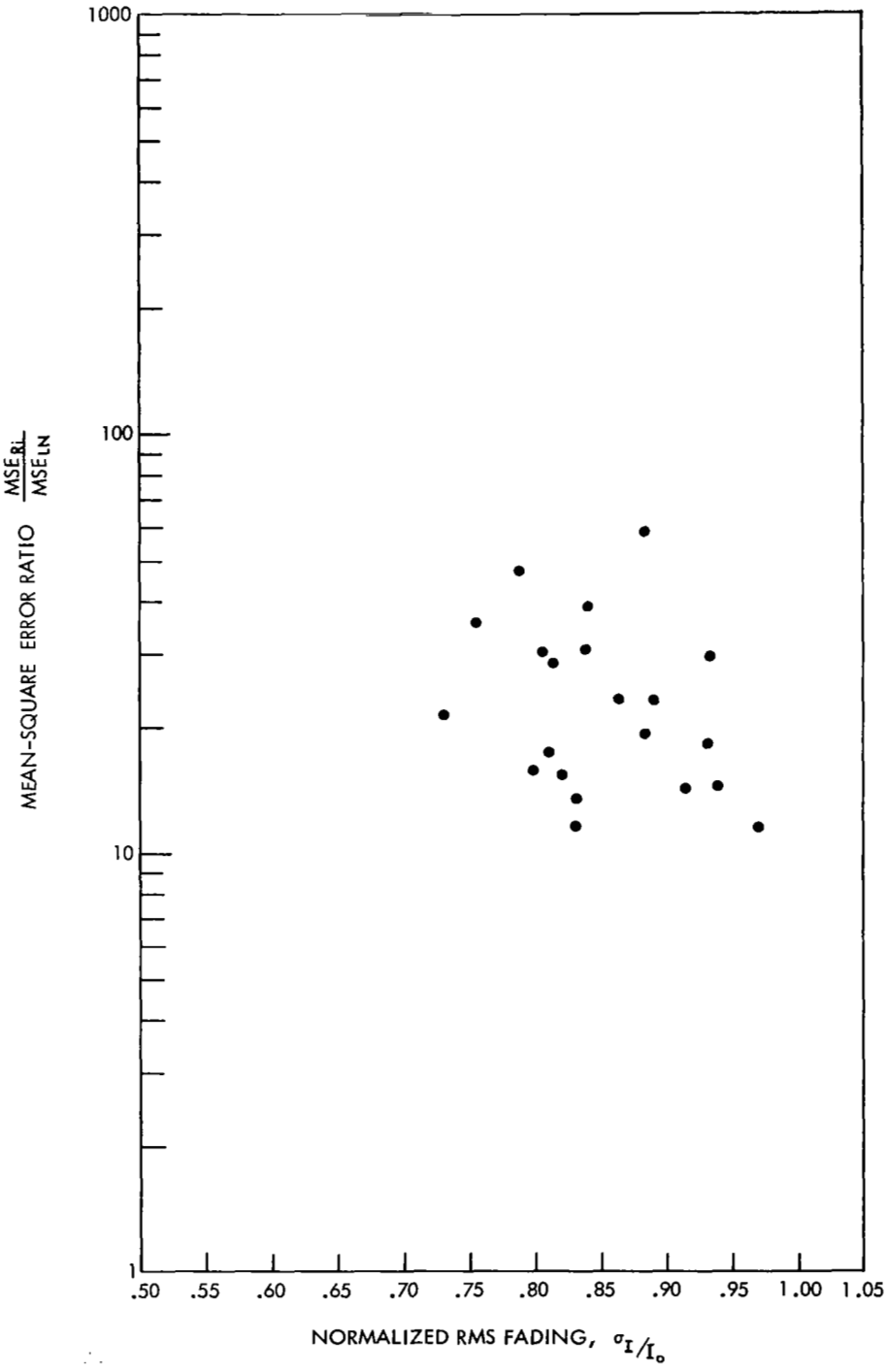

Figure 47. Mean-square error ratio for the modified Rice and log-normal distributions as a function of RMS fading, σ_I/I_0.

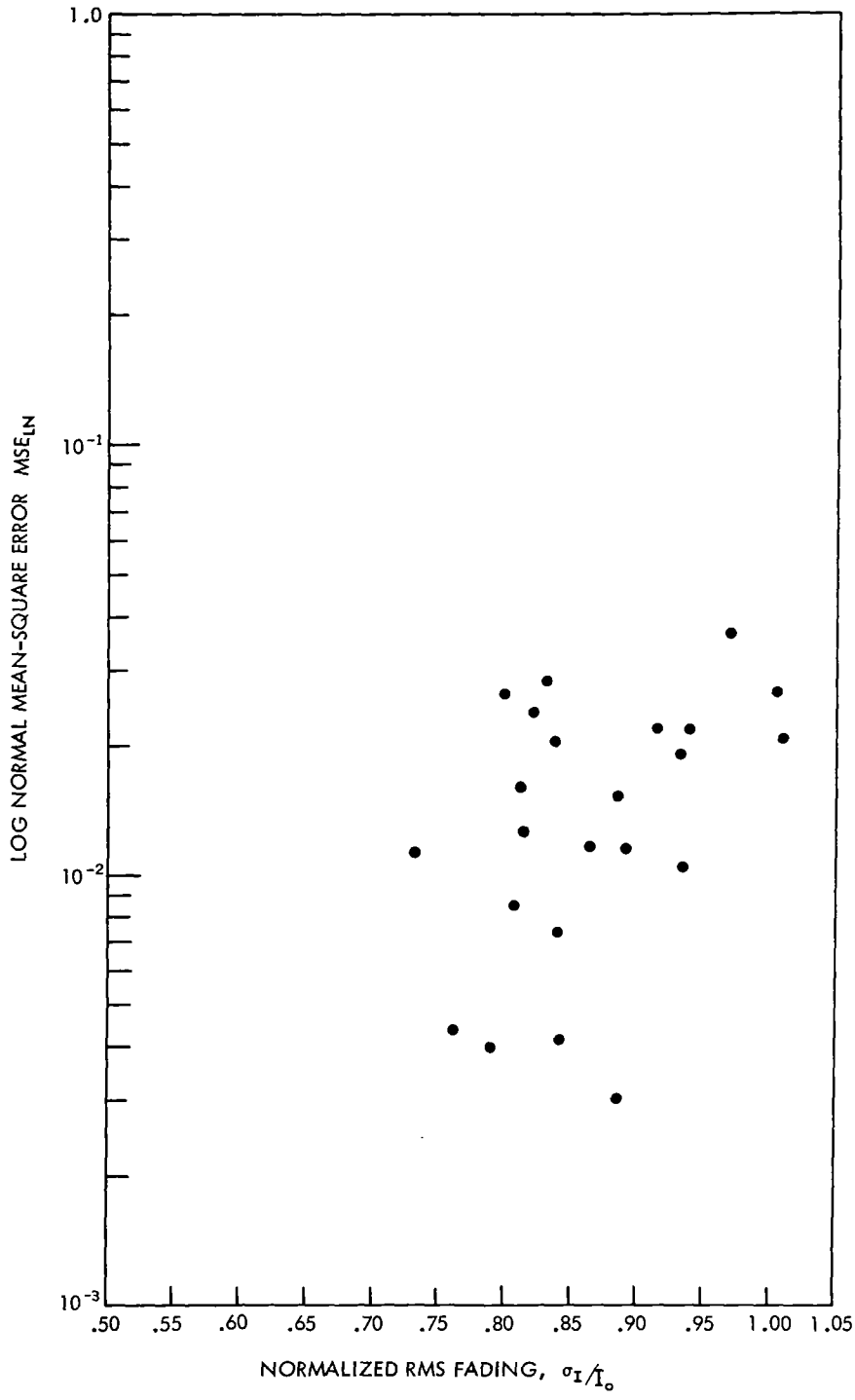

Figure 48. Mean-square error of the log-normal distribution as a function of RMS fading, σ_I/I_0.

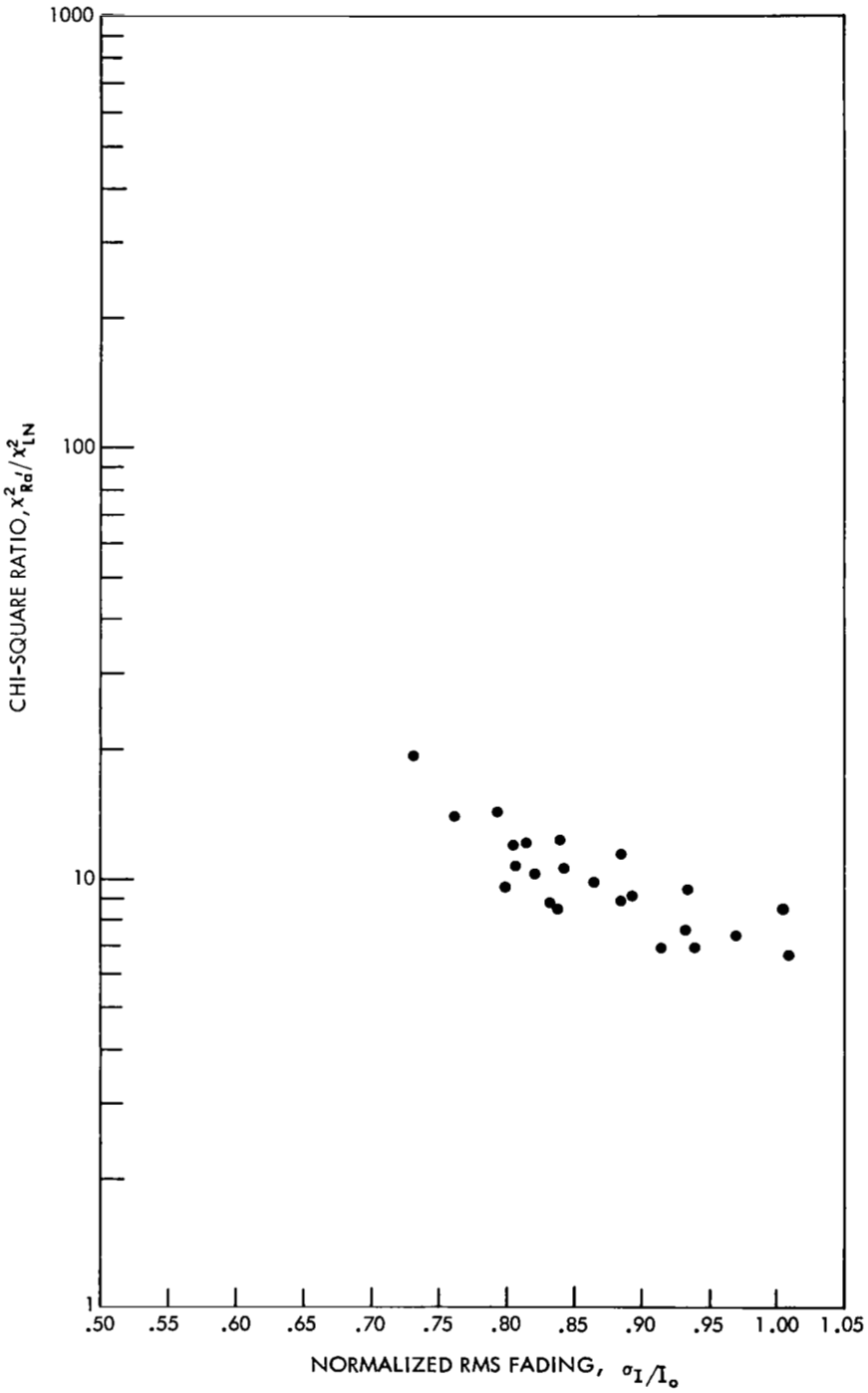

Figure 49. Chi-square ratio for the modified Rayleigh and log-normal distributions as a function of RMS fading, σ_I/I_0.

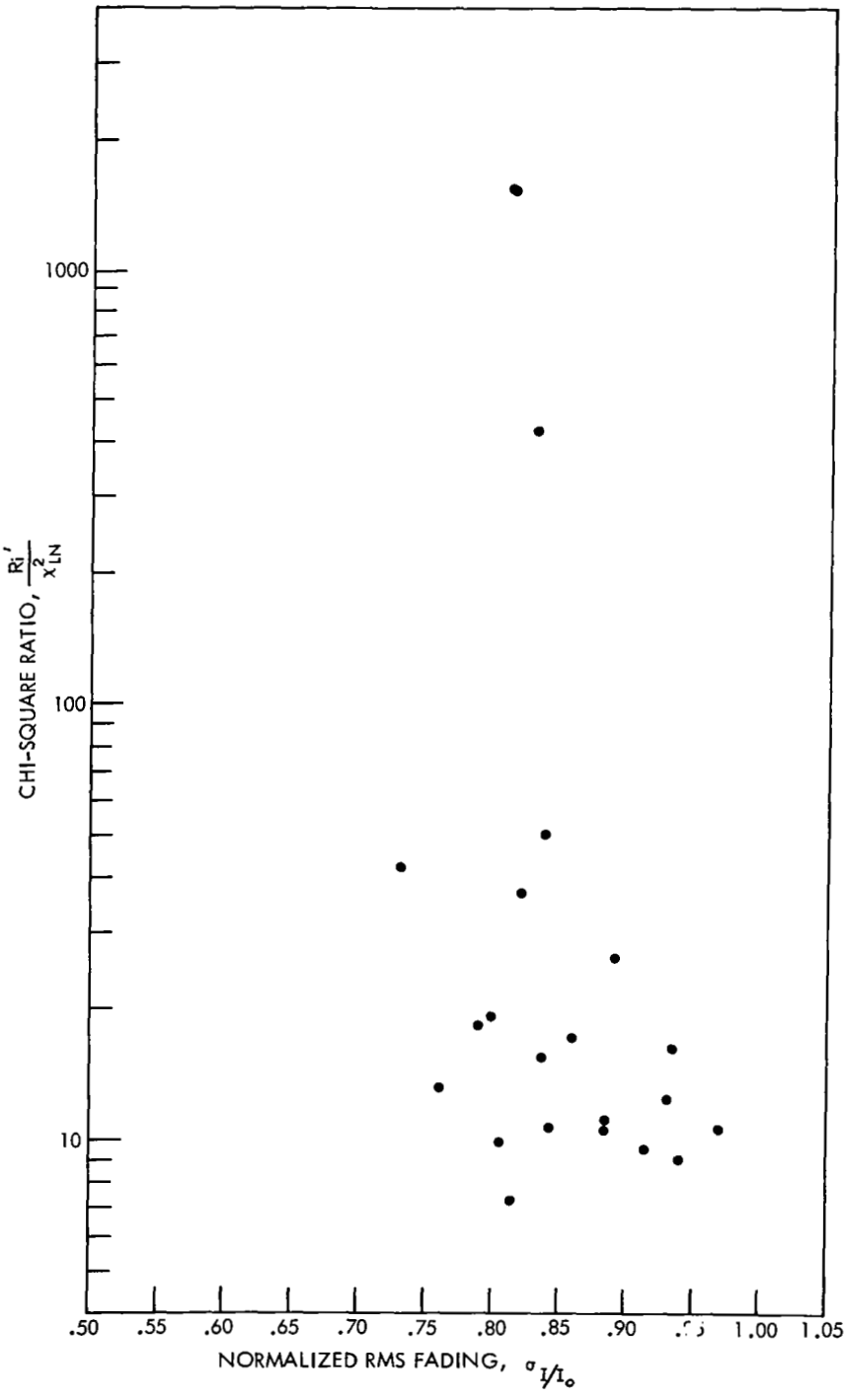

Figure 50. Chi-square ratio for the modified Rice and log-normal distributions as a function of RMS fading, σ_I/I_0.

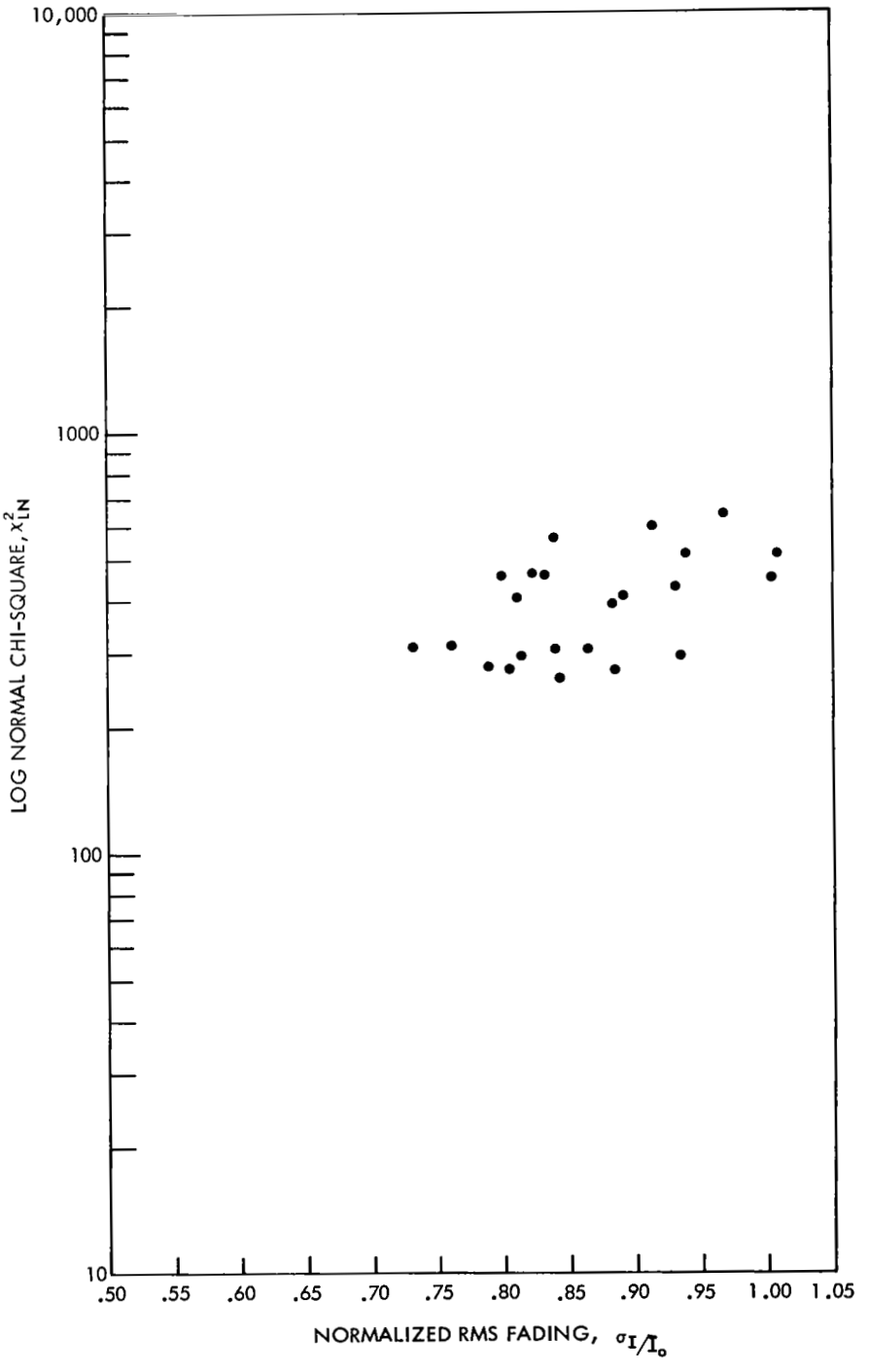

Figure 51. Chi-square value for the log-normal distribution as a function of RMS fading, σ_I/I_0.

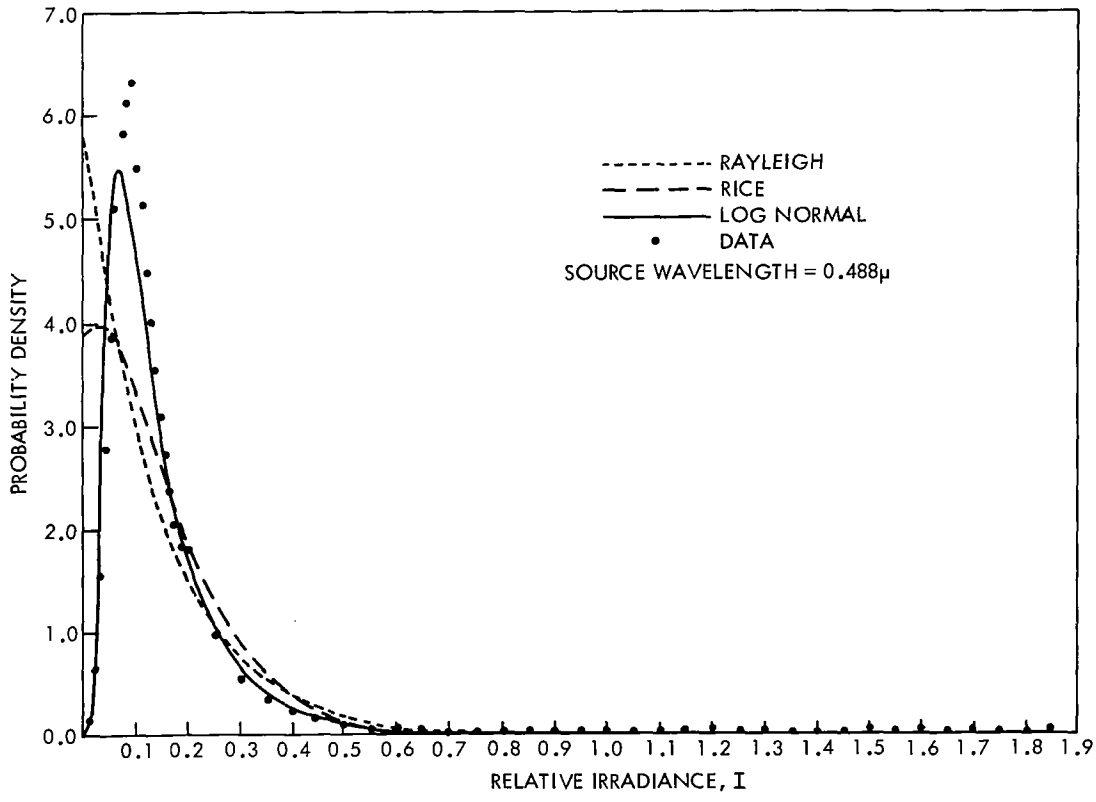

Figure 52. Synthesized log-normal, modified Rayleigh, and modified Rice distributions for strong irradiance fluctuations. The normalized RMS irradiance fading (σ_I/I_0) is 0.833.

Table XV. Computer Results for Record #3 of the Strong-Scintillation Data

Mean-square error and chi-square test results for strong scintillation data ($\lambda = 0.488\mu$).

1. I_i	2. $d(I_i)$	3. $g(I_i)$	4. $Rd(I_i)$	5. $Ri'(I_i)$	6. $\sum_i d(I_i)\,\Delta I$	7. $\sum_i g(I_i)\,\Delta I$	8. $\sum_i Ri'(I_i)\,\Delta I$	9. $\frac{N\Delta I\{d(I_i)-g(I_i)\}^2}{g(I_i)}$	10. $\frac{N\Delta I\{d(I_i)-Ri'(I_i)\}^2}{Ri'(I_i)}$
0.586E-02	0.854E-01	0.941E-02	0.483E 01	0.384E 01	0.100E-02	0.110E-03	0.565E-01	0.144E 03	0.109E 04
0.176E-01	0.465E 00	0.540E 00	0.455E 01	0.377E 01	0.645E-02	0.644E-02	0.110E 00	0.243E 01	0.860E 03
0.293E-01	0.120E 01	0.174E 01	0.430E 01	0.369E 01	0.205E-01	0.268E-01	0.160E 00	0.399E 02	0.524E 03
0.410E-01	0.219E 01	0.294E 01	0.405E 01	0.361E 01	0.461E-01	0.612E-01	0.208E 00	0.449E 02	0.201E 03
0.527E-01	0.337E 01	0.382E 01	0.382E 01	0.351E 01	0.856E-01	0.106E 00	0.252E 00	0.121E 02	0.125E 02
0.644E-01	0.437E 01	0.435E 01	0.361E 01	0.340E 01	0.137E 00	0.157E 00	0.295E 00	0.249E-01	0.379E 02
0.761E-01	0.518E 01	0.460E 01	0.340E 01	0.329E 01	0.197E 00	0.211E 00	0.335E 00	0.169E 02	0.216E 03
0.878E-01	0.533E 01	0.464E 01	0.321E 01	0.318E 01	0.260E 00	0.265E 00	0.372E 00	0.238E 02	0.327E 03
0.995E-01	0.536E 01	0.454E 01	0.303E 01	0.306E 01	0.323E 00	0.318E 00	0.408E 00	0.342E 02	0.419E 03
0.111E 00	0.470E 01	0.436E 01	0.286E 01	0.294E 01	0.378E 00	0.369E 00	0.441E 00	0.629E 01	0.278E 03
0.123E 00	0.425E 01	0.412E 01	0.270E 01	0.282E 01	0.427E 00	0.418E 00	0.473E 00	0.967E 00	0.210E 03
0.135E 00	0.415E 01	0.386E 01	0.255E 01	0.270E 01	0.476E 00	0.463E 00	0.503E 00	0.513E 01	0.237E 03
0.146E 00	0.351E 01	0.359E 01	0.240E 01	0.259E 01	0.517E 00	0.505E 00	0.531E 00	0.358E 00	0.121E 03
0.158E 00	0.340E 01	0.332E 01	0.227E 01	0.247E 01	0.557E 00	0.544E 00	0.557E 00	0.453E 00	0.133E 03
0.170E 00	0.325E 01	0.306E 01	0.214E 01	0.235E 01	0.595E 00	0.580E 00	0.582E 00	0.267E 01	0.135E 03
0.182E 00	0.275E 01	0.281E 01	0.202E 01	0.224E 01	0.627E 00	0.612E 00	0.606E 00	0.274E 00	0.632E 02
0.193E 00	0.262E 01	0.258E 01	0.190E 01	0.213E 01	0.658E 00	0.643E 00	0.628E 00	0.129E 00	0.629E 02
0.205E 00	0.226E 01	0.236E 01	0.180E 01	0.203E 01	0.684E 00	0.670E 00	0.649E 00	0.111E 01	0.281E 02
0.217E 00	0.209E 01	0.217E 01	0.169E 01	0.192E 01	0.709E 00	0.696E 00	0.669E 00	0.808E 00	0.206E 02
0.228E 00	0.177E 01	0.198E 01	0.160E 01	0.182E 01	0.729E 00	0.719E 00	0.688E 00	0.527E 01	0.445E 01
0.240E 00	0.170E 01	0.182E 01	0.151E 01	0.173E 01	0.749E 00	0.740E 00	0.705E 00	0.162E 01	0.599E 01
0.252E 00	0.152E 01	0.166E 01	0.142E 01	0.163E 01	0.767E 00	0.760E 00	0.722E 00	0.305E 01	0.144E 01
0.263E 00	0.136E 01	0.152E 01	0.134E 01	0.154E 01	0.783E 00	0.778E 00	0.738E 00	0.400E 01	0.718E-01
0.275E 00	0.141E 01	0.140E 01	0.127E 01	0.146E 01	0.800E 00	0.794E 00	0.753E 00	0.496E-01	0.402E 01
0.287E 00	0.128E 01	0.128E 01	0.119E 01	0.138E 01	0.815E 00	0.809E 00	0.767E 00	0.909E-04	0.147E 01
0.299E 00	0.111E 01	0.117E 01	0.113E 01	0.130E 01	0.828E 00	0.823E 00	0.780E 00	0.831E 00	0.581E-01
0.310E 00	0.944E 00	0.108E 01	0.106E 01	0.122E 01	0.839E 00	0.835E 00	0.792E 00	0.396E 01	0.315E 01
0.322E 00	0.857E 00	0.991E 00	0.100E 01	0.115E 01	0.849E 00	0.847E 00	0.804E 00	0.211E 01	0.264E 01
0.334E 00	0.777E 00	0.912E 00	0.946E 00	0.108E 01	0.858E 00	0.858E 00	0.815E 00	0.464E 01	0.709E 01
0.345E 00	0.777E 00	0.839E 00	0.893E 00	0.102E 01	0.867E 00	0.867E 00	0.825E 00	0.106E 01	0.352E 01
0.357E 00	0.769E 00	0.773E 00	0.843E 00	0.957E 00	0.876E 00	0.876E 00	0.835E 00	0.490E-02	0.152E 01
0.369E 00	0.628E 00	0.712E 00	0.795E 00	0.899E 00	0.884E 00	0.885E 00	0.845E 00	0.235E 01	0.823E 01
0.381E 00	0.538E 00	0.657E 00	0.750E 00	0.844E 00	0.890E 00	0.893E 00	0.853E 00	0.505E 01	0.140E 02
0.392E 00	0.564E 00	0.607E 00	0.708E 00	0.792E 00	0.897E 00	0.900E 00	0.862E 00	0.715E 00	0.685E 01
0.404E 00	0.521E 00	0.561E 00	0.668E 00	0.742E 00	0.903E 00	0.906E 00	0.870E 00	0.658E 00	0.754E 01
0.416E 00	0.504E 00	0.519E 00	0.630E 00	0.696E 00	0.909E 00	0.912E 00	0.877E 00	0.966E-01	0.590E 01
0.427E 00	0.423E 00	0.480E 00	0.594E 00	0.652E 00	0.914E 00	0.918E 00	0.884E 00	0.160E 01	0.116E 02
0.439E 00	0.517E 00	0.445E 00	0.561E 00	0.610E 00	0.920E 00	0.923E 00	0.890E 00	0.274E 01	0.806E 00
0.451E 00	0.380E 00	0.412E 00	0.529E 00	0.571E 00	0.924E 00	0.928E 00	0.897E 00	0.586E 00	0.982E 01
0.463E 00	0.427E 00	0.382E 00	0.499E 00	0.534E 00	0.929E 00	0.932E 00	0.902E 00	0.122E 01	0.243E 01
0.474E 00	0.372E 00	0.355E 00	0.471E 00	0.499E 00	0.933E 00	0.937E 00	0.908E 00	0.178E 00	0.491E 01
0.486E 00	0.342E 00	0.330E 00	0.444E 00	0.466E 00	0.937E 00	0.940E 00	0.913E 00	0.968E-01	0.555E 01
0.498E 00	0.260E 00	0.307E 00	0.419E 00	0.436E 00	0.941E 00	0.944E 00	0.918E 00	0.164E 01	0.141E 02

Table XV. (Continued)

0.509E 00	0.325E 00	0.286E 00	0.395E 00	0.407E 00	0.944E 00	0.947E 00	0.923E 00	0.125E 01	0.298E 01
0.521E 00	0.239E 00	0.266E 00	0.373E 00	0.380E 00	0.947E 00	0.950E 00	0.927E 00	0.632E 00	0.113E 02
0.533E 00	0.243E 00	0.248E 00	0.352E 00	0.354E 00	0.950E 00	0.953E 00	0.931E 00	0.185E-01	0.784E 01
0.545E 00	0.239E 00	0.231E 00	0.332E 00	0.331E 00	0.953E 00	0.956E 00	0.935E 00	0.650E-01	0.609E 01
0.556E 00	0.196E 00	0.216E 00	0.313E 00	0.308E 00	0.955E 00	0.959E 00	0.939E 00	0.403E 00	0.102E 02
0.568E 00	0.222E 00	0.201E 00	0.296E 00	0.287E 00	0.958E 00	0.961E 00	0.942E 00	0.494E 00	0.429E 01
0.580E 00	0.218E 00	0.188E 00	0.279E 00	0.268E 00	0.960E 00	0.963E 00	0.946E 00	0.109E 01	0.314E 01
0.591E 00	0.179E 00	0.176E 00	0.263E 00	0.249E 00	0.962E 00	0.965E 00	0.949E 00	0.146E-01	0.625E 01
0.603E 00	0.120E 00	0.165E 00	0.248E 00	0.232E 00	0.964E 00	0.967E 00	0.951E 00	0.290E 01	0.156E 02
0.615E 00	0.111E 00	0.154E 00	0.234E 00	0.216E 00	0.965E 00	0.969E 00	0.954E 00	0.283E 01	0.152E 02
0.627E 00	0.154E 00	0.144E 00	0.221E 00	0.201E 00	0.967E 00	0.971E 00	0.957E 00	0.138E 00	0.479E 01
0.638E 00	0.149E 00	0.135E 00	0.208E 00	0.187E 00	0.969E 00	0.972E 00	0.959E 00	0.339E 00	0.391E 01
0.650E 00	0.141E 00	0.127E 00	0.197E 00	0.174E 00	0.970E 00	0.974E 00	0.962E 00	0.354E 00	0.371E 01
0.662E 00	0.158E 00	0.119E 00	0.186E 00	0.162E 00	0.972E 00	0.975E 00	0.964E 00	0.295E 01	0.960E 00
0.673E 00	0.137E 00	0.112E 00	0.175E 00	0.150E 00	0.974E 00	0.976E 00	0.966E 00	0.127E 01	0.198E 01
0.685E 00	0.111E 00	0.105E 00	0.165E 00	0.140E 00	0.975E 00	0.978E 00	0.968E 00	0.747E-01	0.416E 01
0.697E 00	0.811E-01	0.989E-01	0.156E 00	0.130E 00	0.976E 00	0.979E 00	0.970E 00	0.750E 00	0.839E 01
0.708E 00	0.107E 00	0.931E-01	0.147E 00	0.120E 00	0.977E 00	0.980E 00	0.971E 00	0.472E 00	0.259E 01
0.720E 00	0.120E 00	0.876E-01	0.139E 00	0.112E 00	0.979E 00	0.981E 00	0.973E 00	0.273E 01	0.620E 00
0.732E 00	0.598E-01	0.825E-01	0.131E 00	0.104E 00	0.979E 00	0.982E 00	0.974E 00	0.146E 01	0.905E 01
0.744E 00	0.683E-01	0.777E-01	0.123E 00	0.964E-01	0.980E 00	0.983E 00	0.976E 00	0.265E 00	0.577E 01
0.755E 00	0.726E-01	0.732E-01	0.117E 00	0.894E-01	0.981E 00	0.984E 00	0.977E 00	0.136E-02	0.388E 01
0.767E 00	0.115E 00	0.691E-01	0.110E 00	0.829E-01	0.982E 00	0.984E 00	0.979E 00	0.724E 01	0.614E-01
0.779E 00	0.726E-01	0.652E-01	0.104E 00	0.769E-01	0.983E 00	0.985E 00	0.980E 00	0.198E 00	0.219E 01
0.790E 00	0.512E-01	0.615E-01	0.979E-01	0.713E-01	0.984E 00	0.986E 00	0.981E 00	0.403E 00	0.520E 01
0.802E 00	0.555E-01	0.581E-01	0.923E-01	0.661E-01	0.984E 00	0.987E 00	0.982E 00	0.271E-01	0.344E 01
0.814E 00	0.598E-01	0.549E-01	0.871E-01	0.613E-01	0.985E 00	0.987E 00	0.983E 00	0.102E 00	0.201E 01
0.826E 00	0.769E-01	0.519E-01	0.822E-01	0.568E-01	0.986E 00	0.988E 00	0.984E 00	0.281E 01	0.805E-01
0.837E 00	0.384E-01	0.491E-01	0.775E-01	0.526E-01	0.986E 00	0.988E 00	0.985E 00	0.541E 00	0.462E 01
0.849E 00	0.214E-01	0.464E-01	0.732E-01	0.487E-01	0.987E 00	0.989E 00	0.986E 00	0.317E 01	0.859E 01
0.861E 00	0.512E-01	0.440E-01	0.690E-01	0.451E-01	0.987E 00	0.990E 00	0.987E 00	0.283E 00	0.107E 01
0.872E 00	0.342E-01	0.416E-01	0.651E-01	0.417E-01	0.988E 00	0.990E 00	0.987E 00	0.313E 00	0.345E 01
0.884E 00	0.512E-01	0.394E-01	0.614E-01	0.386E-01	0.988E 00	0.990E 00	0.988E 00	0.829E 00	0.396E 00
0.896E 00	0.512E-01	0.374E-01	0.580E-01	0.358E-01	0.989E 00	0.991E 00	0.989E 00	0.121E 01	0.182E 00
0.908E 00	0.342E-01	0.354E-01	0.547E-01	0.331E-01	0.989E 00	0.991E 00	0.989E 00	0.107E-01	0.180E 01
0.919E 00	0.598E-01	0.336E-01	0.516E-01	0.306E-01	0.990E 00	0.992E 00	0.990E 00	0.478E 01	0.304E 00
0.931E 00	0.512E-01	0.319E-01	0.487E-01	0.283E-01	0.991E 00	0.992E 00	0.990E 00	0.275E 01	0.317E-01
0.943E 00	0.470E-01	0.303E-01	0.459E-01	0.262E-01	0.991E 00	0.992E 00	0.991E 00	0.216E 01	0.559E-02
0.954E 00	0.342E-01	0.287E-01	0.433E-01	0.242E-01	0.992E 00	0.993E 00	0.992E 00	0.239E 00	0.454E 00
0.966E 00	0.299E-01	0.273E-01	0.409E-01	0.224E-01	0.992E 00	0.993E 00	0.992E 00	0.575E-01	0.692E 00
0.978E 00	0.342E-01	0.259E-01	0.386E-01	0.207E-01	0.992E 00	0.993E 00	0.992E 00	0.610E 00	0.118E 00
0.990E 00	0.214E-01	0.247E-01	0.364E-01	0.191E-01	0.993E 00	0.994E 00	0.993E 00	0.104E 00	0.146E 01
0.100E 01	0.128E-01	0.235E-01	0.343E-01	0.177E-01	0.993E 00	0.994E 00	0.993E 00	0.113E 01	0.316E 01
0.101E 01	0.214E-01	0.223E-01	0.324E-01	0.163E-01	0.993E 00	0.994E 00	0.994E 00	0.967E-02	0.881E 00
0.102E 01	0.214E-01	0.212E-01	0.306E-01	0.151E-01	0.993E 00	0.994E 00	0.994E 00	0.159E-03	0.650E 00
0.104E 01	0.171E-01	0.202E-01	0.288E-01	0.139E-01	0.993E 00	0.995E 00	0.994E 00	0.114E 00	0.112E 01
0.105E 01	0.299E-01	0.192E-01	0.272E-01	0.129E-01	0.994E 00	0.995E 00	0.995E 00	0.138E 01	0.622E-01
0.106E 01	0.512E-01	0.183E-01	0.257E-01	0.119E-01	0.994E 00	0.995E 00	0.995E 00	0.138E 02	0.597E 01
0.107E 01	0.256E-01	0.175E-01	0.242E-01	0.110E-01	0.995E 00	0.995E 00	0.995E 00	0.891E 00	0.191E-01
0.108E 01	0.384E-01	0.167E-01	0.228E-01	0.101E-01	0.995E 00	0.996E 00	0.996E 00	0.667E 01	0.249E 01
0.109E 01	0.854E-02	0.159E-01	0.216E-01	0.934E-02	0.995E 00	0.996E 00	0.996E 00	0.794E 00	0.184E 01
0.111E 01	0.214E-01	0.151E-01	0.203E-01	0.861E-02	0.995E 00	0.996E 00	0.996E 00	0.596E 00	0.119E-01
0.112E 01	0.171E-01	0.144E-01	0.192E-01	0.795E-02	0.996E 00	0.996E 00	0.996E 00	0.113E 00	0.541E-01

Table XV. (Continued)

0.113E 01	0.171E-01	0.138E-01	0.181E-01	0.733E-02	0.996E 00	0.996E 00	0.996E 00	0.184E 00	0.135E-01
0.114E 01	0.171E-01	0.132E-01	0.171E-01	0.676E-02	0.996E 00	0.996E 00	0.997E 00	0.273E 00	0.517E-07
0.115E 01	0.854E-02	0.126E-01	0.161E-01	0.624E-02	0.996E 00	0.997E 00	0.997E 00	0.302E 00	0.834E 00
0.117E 01	0.171E-01	0.120E-01	0.152E-01	0.575E-02	0.996E 00	0.997E 00	0.997E 00	0.503E 00	0.543E-01
0.118E 01	0.214E-01	0.115E-01	0.143E-01	0.530E-02	0.997E 00	0.997E 00	0.997E 00	0.199E 01	0.802E 00
0.119E 01	0.427E-02	0.110E-01	0.135E-01	0.489E-02	0.997E 00	0.997E 00	0.997E 00	0.957E 00	0.148E 01
0.120E 01	0.171E-01	0.105E-01	0.128E-01	0.451E-02	0.997E 00	0.997E 00	0.998E 00	0.974E 00	0.341E 00
0.121E 01	0.427E-02	0.100E-01	0.120E-01	0.415E-02	0.997E 00	0.997E 00	0.998E 00	0.773E 00	0.118E 01
0.122E 01	0.427E-02	0.958E-02	0.114E-01	0.383E-02	0.997E 00	0.997E 00	0.998E 00	0.690E 00	0.104E 01
0.124E 01	0.427E-02	0.917E-02	0.107E-01	0.353E-02	0.997E 00	0.997E 00	0.998E 00	0.613E 00	0.909E 00
0.125E 01	0.854E-02	0.878E-02	0.101E-01	0.325E-02	0.997E 00	0.998E 00	0.998E 00	0.148E-02	0.575E-01
0.126E 01	0.854E-02	0.840E-02	0.954E-02	0.299E-02	0.997E 00	0.998E 00	0.998E 00	0.544E-03	0.247E-01
0.127E 01	0.854E-02	0.804E-02	0.901E-02	0.276E-02	0.997E 00	0.998E 00	0.998E 00	0.719E-02	0.562E-02
0.128E 01	0.854E-02	0.770E-02	0.850E-02	0.254E-02	0.997E 00	0.998E 00	0.998E 00	0.213E-01	0.542E-04
0.129E 01	0.427E-02	0.738E-02	0.802E-02	0.234E-02	0.997E 00	0.998E 00	0.998E 00	0.307E 00	0.410E 00
0.131E 01	0.128E-01	0.707E-02	0.756E-02	0.215E-02	0.998E 00	0.998E 00	0.999E 00	0.109E 01	0.853E 00
0.132E 01	0.854E-02	0.678E-02	0.714E-02	0.198E-02	0.998E 00	0.998E 00	0.999E 00	0.107E 00	0.648E-01
0.133E 01	0.0	0.650E-02	0.673E-02	0.183E-02	0.998E 00	0.998E 00	0.999E 00	0.152E 01	0.158E 01
0.134E 01	0.171E-01	0.623E-02	0.635E-02	0.168E-02	0.998E 00	0.998E 00	0.999E 00	0.443E 01	0.425E 01
0.135E 01	0.214E-01	0.598E-02	0.599E-02	0.155E-02	0.998E 00	0.998E 00	0.999E 00	0.927E 01	0.922E 01
0.136E 01	0.427E-02	0.573E-02	0.565E-02	0.142E-02	0.998E 00	0.998E 00	0.999E 00	0.874E-01	0.793E-01
0.138E 01	0.214E-01	0.550E-02	0.533E-02	0.131E-02	0.998E 00	0.998E 00	0.999E 00	0.107E 02	0.113E 02
0.139E 01	0.427E-02	0.528E-02	0.503E-02	0.120E-02	0.998E 00	0.998E 00	0.999E 00	0.452E-01	0.270E-01
0.140E 01	0.427E-02	0.507E-02	0.475E-02	0.111E-02	0.999E 00	0.999E 00	0.999E 00	0.295E-01	0.113E-01
0.141E 01	0.427E-02	0.487E-02	0.448E-02	0.102E-02	0.999E 00	0.999E 00	0.999E 00	0.171E-01	0.229E-02
0.142E 01	0.0	0.467E-02	0.423E-02	0.938E-03	0.999E 00	0.999E 00	0.999E 00	0.109E 01	0.990E 00
0.143E 01	0.854E-02	0.449E-02	0.399E-02	0.863E-03	0.999E 00	0.999E 00	0.999E 00	0.856E 00	0.122E 01
0.145E 01	0.854E-02	0.431E-02	0.376E-02	0.793E-03	0.999E 00	0.999E 00	0.999E 00	0.970E 00	0.142E 01
0.146E 01	0.427E-02	0.415E-02	0.355E-02	0.730E-03	0.999E 00	0.999E 00	0.999E 00	0.872E-03	0.343E-01
0.147E 01	0.128E-01	0.399E-02	0.335E-02	0.671E-03	0.999E 00	0.999E 00	0.999E 00	0.458E 01	0.626E 01
0.148E 01	0.854E-02	0.383E-02	0.316E-02	0.617E-03	0.999E 00	0.999E 00	0.999E 00	0.136E 01	0.215E 01
0.149E 01	0.427E-02	0.368E-02	0.298E-02	0.567E-03	0.999E 00	0.999E 00	0.999E 00	0.218E-01	0.131E 00
0.150E 01	0.427E-02	0.354E-02	0.281E-02	0.521E-03	0.999E 00	0.999E 00	0.999E 00	0.349E-01	0.177E 00
0.152E 01	0.854E-02	0.341E-02	0.265E-02	0.479E-03	0.999E 00	0.999E 00	0.999E 00	0.181E 01	0.306E 01
0.153E 01	0.854E-02	0.328E-02	0.250E-02	0.440E-03	0.999E 00	0.999E 00	0.100E 01	0.198E 01	0.341E 01
0.154E 01	0.0	0.316E-02	0.236E-02	0.405E-03	0.999E 00	0.999E 00	0.100E 01	0.739E 00	0.553E 00
0.155E 01	0.427E-02	0.304E-02	0.223E-02	0.372E-03	0.999E 00	0.999E 00	0.100E 01	0.117E 00	0.438E 00
0.156E 01	0.0	0.293E-02	0.210E-02	0.342E-03	0.999E 00	0.999E 00	0.100E 01	0.685E 00	0.492E 00
0.158E 01	0.427E-02	0.282E-02	0.198E-02	0.314E-03	0.999E 00	0.999E 00	0.100E 01	0.176E 00	0.617E 00
0.159E 01	0.0	0.271E-02	0.187E-02	0.288E-03	0.999E 00	0.999E 00	0.100E 01	0.635E 00	0.438E 00
0.160E 01	0.427E-02	0.261E-02	0.177E-02	0.265E-03	0.100E 01	0.999E 00	0.100E 01	0.246E 00	0.832E 00
0.161E 01	0.0	0.252E-02	0.167E-02	0.243E-03	0.100E 01	0.999E 00	0.100E 01	0.590E 00	0.590E 00
0.162E 01	0.0	0.243E-02	0.157E-02	0.223E-03	0.100E 01	0.999E 00	0.100E 01	0.568E 00	0.368E 00
0.163E 01	0.0	0.234E-02	0.148E-02	0.205E-03	0.100E 01	0.999E 00	0.100E 01	0.548E 00	0.347E 00
0.165E 01	0.427E-02	0.225E-02	0.140E-02	0.188E-03	0.100E 01	0.999E 00	0.100E 01	0.423E 00	0.138E 01
0.166E 01	0.0	0.217E-02	0.132E-02	0.173E-03	0.100E 01	0.999E 00	0.100E 01	0.509E 00	0.309E 00
0.167E 01	0.0	0.210E-02	0.125E-02	0.159E-03	0.100E 01	0.999E 00	0.100E 01	0.491E 00	0.292E 00
0.168E 01	0.0	0.202E-02	0.118E-02	0.146E-03	0.100E 01	0.999E 00	0.100E 01	0.473E 00	0.275E 00
0.169E 01	0.0	0.195E-02	0.111E-02	0.134E-03	0.100E 01	0.999E 00	0.100E 01	0.456E 00	0.260E 00
0.170E 01	0.0	0.188E-02	0.105E-02	0.123E-03	0.100E 01	0.999E 00	0.100E 01	0.440E 00	0.245E 00
0.172E 01	0.854E-02	0.181E-02	0.987E-03	0.113E-03	0.100E 01	0.999E 00	0.100E 01	0.584E 01	0.135E 02
0.173E 01	0.0	0.175E-02	0.931E-03	0.103E-03	0.100E 01	0.100E 01	0.100E 01	0.410E 00	0.218E 00
0.174E 01	0.427E-02	0.169E-02	0.878E-03	0.950E-04	0.100E 01	0.100E 01	0.100E 01	0.923E 00	0.307E 01

Table XV. (Concluded)

0.175E 01	0.0	0.163E-02	0.829E-03	0.871E-04	0.100E 01	0.100E 01	0.100E 01	0.382E 00	0.194E 00
0.176E 01	0.0	0.158E-02	0.782E-03	0.800E-04	0.100E 01	0.100E 01	0.100E 01	0.369E 00	0.183E 00
0.177E 01	0.427E-02	0.152E-02	0.738E-03	0.734E-04	0.100E 01	0.100E 01	0.100E 01	0.116E 01	0.396E 01
0.179E 01	0.427E-02	0.147E-02	0.696E-03	0.673E-04	0.100E 01	0.100E 01	0.100E 01	0.125E 01	0.430E 01
0.180E 01	0.0	0.142E-02	0.657E-03	0.617E-04	0.100E 01	0.100E 01	0.100E 01	0.332E 00	0.154E 00
0.181E 01	0.0	0.137E-02	0.620E-03	0.566E-04	0.100E 01	0.100E 01	0.100E 01	0.321E 00	0.145E 00
0.182E 01	0.0	0.133E-02	0.585E-03	0.520E-04	0.100E 01	0.100E 01	0.100E 01	0.310E 00	0.137E 00
0.183E 01	0.0	0.128E-02	0.551E-03	0.476E-04	0.100E 01	0.100E 01	0.100E 01	0.300E 00	0.129E 00
0.184E 01	0.0	0.124E-02	0.520E-03	0.437E-04	0.100E 01	0.100E 01	0.100E 01	0.290E 00	0.122E 00
0.186E 01	0.0	0.120E-02	0.491E-03	0.401E-04	0.100E 01	0.100E 01	0.100E 01	0.280E 00	0.115E 00
0.187E 01	0.0	0.116E-02	0.463E-03	0.367E-04	0.100E 01	0.100E 01	0.100E 01	0.271E 00	0.108E 00
0.188E 01	0.0	0.112E-02	0.437E-03	0.337E-04	0.100E 01	0.100E 01	0.100E 01	0.262E 00	0.102E 00
0.189E 01	0.0	0.108E-02	0.412E-03	0.309E-04	0.100E 01	0.100E 01	0.100E 01	0.253E 00	0.966E-01
0.190E 01	0.0	0.105E-02	0.389E-03	0.283E-04	0.100E 01	0.100E 01	0.100E 01	0.245E 00	0.911E-01
0.191E 01	0.0	0.101E-02	0.367E-03	0.260E-04	0.100E 01	0.100E 01	0.100E 01	0.237E 00	0.859E-01
0.193E 01	0.0	0.979E-03	0.346E-03	0.238E-04	0.100E 01	0.100E 01	0.100E 01	0.229E 00	0.811E-01
0.194E 01	0.427E-02	0.948E-03	0.327E-03	0.218E-04	0.100E 01	0.100E 01	0.100E 01	0.273E 01	0.112E 02
0.195E 01	0.427E-02	0.917E-03	0.308E-03	0.200E-04	0.100E 01	0.100E 01	0.100E 01	0.287E 01	0.119E 02
0.196E 01	0.0	0.888E-03	0.291E-03	0.183E-04	0.100E 01	0.100E 01	0.100E 01	0.208E 00	0.681E-01
0.197E 01	0.0	0.859E-03	0.274E-03	0.168E-04	0.100E 01	0.100E 01	0.100E 01	0.201E 00	0.643E-01
0.198E 01	0.0	0.832E-03	0.259E-03	0.154E-04	0.100E 01	0.100E 01	0.100E 01	0.195E 00	0.606E-01
0.200E 01	0.0	0.806E-03	0.244E-03	0.141E-04	0.100E 01	0.100E 01	0.100E 01	0.189E 00	0.572E-01
0.201E 01	0.427E-02	0.780E-03	0.230E-03	0.129E-04	0.100E 01	0.100E 01	0.100E 01	0.366E 01	0.166E 02
0.202E 01	0.0	0.756E-03	0.217E-03	0.118E-04	0.100E 01	0.100E 01	0.100E 01	0.177E 00	0.509E-01
0.203E 01	0.0	0.732E-03	0.205E-03	0.108E-04	0.100E 01	0.100E 01	0.100E 01	0.171E 00	0.480E-01
0.204E 01	0.0	0.709E-03	0.193E-03	0.994E-05	0.100E 01	0.100E 01	0.100E 01	0.166E 00	0.453E-01
0.206E 01	0.0	0.687E-03	0.183E-03	0.910E-05	0.100E 01	0.100E 01	0.100E 01	0.161E 00	0.428E-01
0.207E 01	0.0	0.666E-03	0.172E-03	0.834E-05	0.100E 01	0.100E 01	0.100E 01	0.156E 00	0.403E-01
0.208E 01	0.0	0.645E-03	0.162E-03	0.764E-05	0.100E 01	0.100E 01	0.100E 01	0.151E 00	0.381E-01
0.209E 01	0.0	0.625E-03	0.153E-03	0.700E-05	0.100E 01	0.100E 01	0.100E 01	0.146E 00	0.359E-01
0.210E 01	0.0	0.606E-03	0.145E-03	0.641E-05	0.100E 01	0.100E 01	0.100E 01	0.142E 00	0.339E-01
0.211E 01	0.0	0.588E-03	0.136E-03	0.587E-05	0.100E 01	0.100E 01	0.100E 01	0.138E 00	0.320E-01
0.213E 01	0.0	0.570E-03	0.129E-03	0.537E-05	0.100E 01	0.100E 01	0.100E 01	0.133E 00	0.302E-01
0.214E 01	0.0	0.553E-03	0.121E-03	0.492E-05	0.100E 01	0.100E 01	0.100E 01	0.129E 00	0.285E-01
0.215E 01	0.0	0.536E-03	0.115E-03	0.451E-05	0.100E 01	0.100E 01	0.100E 01	0.126E 00	0.268E-01
0.216E 01	0.0	0.520E-03	0.108E-03	0.413E-05	0.100E 01	0.100E 01	0.100E 01	0.122E 00	0.253E-01
0.217E 01	0.0	0.504E-03	0.102E-03	0.378E-05	0.100E 01	0.100E 01	0.100E 01	0.118E 00	0.239E-01
0.218E 01	0.0	0.489E-03	0.963E-04	0.346E-05	0.100E 01	0.100E 01	0.100E 01	0.115E 00	0.225E-01
0.220E 01	0.0	0.475E-03	0.908E-04	0.317E-05	0.100E 01	0.100E 01	0.100E 01	0.111E 00	0.213E-01
0.221E 01	0.0	0.461E-03	0.857E-04	0.290E-05	0.100E 01	0.100E 01	0.100E 01	0.108E 00	0.201E-01
0.222E 01	0.0	0.447E-03	0.808E-04	0.265E-05	0.100E 01	0.100E 01	0.100E 01	0.105E 00	0.189E-01
0.223E 01	0.0	0.434E-03	0.763E-04	0.243E-05	0.100E 01	0.100E 01	0.100E 01	0.102E 00	0.179E-01
0.224E 01	0.0	0.421E-03	0.720E-04	0.222E-05	0.100E 01	0.100E 01	0.100E 01	0.986E-01	0.169E-01
0.225E 01	0.0	0.409E-03	0.679E-04	0.203E-05	0.100E 01	0.100E 01	0.100E 01	0.958E-01	0.159E-01
0.227E 01	0.0	0.397E-03	0.641E-04	0.186E-05	0.100E 01	0.100E 01	0.100E 01	0.930E-01	0.150E-01
0.228E 01	0.0	0.385E-03	0.604E-04	0.170E-05	0.100E 01	0.100E 01	0.100E 01	0.903E-01	0.142E-01
0.229E 01	0.0	0.374E-03	0.570E-04	0.156E-05	0.100E 01	0.100E 01	0.100E 01	0.877E-01	0.134E-01
0.230E 01	0.0	0.364E-03	0.538E-04	0.143E-05	0.100E 01	0.100E 01	0.100E 01	0.851E-01	0.126E-01
0.231E 01	0.0	0.353E-03	0.508E-04	0.130E-05	0.100E 01	0.100E 01	0.100E 01	0.827E-01	0.119E-01
0.232E 01	0.0	0.343E-03	0.479E-04	0.119E-05	0.100E 01	0.100E 01	0.100E 01	0.803E-01	0.112E-01

TABLE XVI

Percentage Points of the Chi-Square Distribution

With 200 Degrees of Freedom

$P[\chi^2_{200} > A] = \alpha$	
α	A
0.20	217
0.10	226
0.05	234
0.025	241
0.01	249
0.005	255
0.001	267

clear that for every data record tabulated in this section, the hypothesis that the data sample came from a log-normal, Rayleigh, or Rice distribution can be tested at any level of significance (i.e., any α value). However, it is doubtful that this is a very useful approach in this experiment since in each data record a large number of classes had zero observations. One of the generally accepted rules for applying hypothesis testing to the chi-square goodness-of-fit parameter is that every class of the measured density function contain one or more observations. In this experiment we attempted to comply with this requirement by coding the analysis so that the first class contained the lowest irradiance signal encountered in the data and the last class contained the highest irradiance level in the data. Even so, there were sometimes as many as 80 and often about 50

classes which had zero observations at the end of a 20-second data run. So it is doubtful that hypothesis testing has much utility under these conditions.

This section has shown that the probability density function for irradiance fluctuations has been tested under very weak and strong fluctuation conditions. For weak fluctuations, the log-normal and Rice distributions were found to be equally compatible with the data; for strong fluctuactions, the log-normal distribution appears to fit the data much more accurately than either the Rice or the Rayleigh distribution.

2.6 Summary and Conclusions

This dissertation has reviewed the optical propagation problem from first principles and has presented a listing of available theoretical results for various source types and propagation paths. The Obukohov-Kolmogorov model of turbulence has been emphasized, since it appears to be the most realistic and accurate statistical description.

The results of a group of experiments conducted over 0.4-km and 1.17-km near-ground horizontal ranges have also been presented. The experiments were directed toward measuring parameters which control the quality of a communication channel. Results were compared to Rytov-based propagation theory as developed in the United States and the Soviet Union.

Signal fading characteristics as denoted by the variance of log amplitude were measured simultaneously for visible and infrared beams which had traversed the same path. The results were in excellent agreement with theory and show clearly the reduction in fading which can be obtained with longer-wavelength

signal sources. The valid parameter ranges of Rytov theory are known to be limited by the saturation of the log-amplitude variance. Published results for the saturation level are contradictory. Early experiments indicated saturation at about 0.2, but recent results indicate that the saturation level is closer to 0.6. A possible explanation suggested by our experimental data for this discrepancy has been discussed. Data reduction techniques which assume log-normality for amplitude statistics appear to be very limited in accuracy.

Diversity communication techniques have been investigated through the spatial and spectral irradiance correlation functions. The respective log-amplitude correlation functions were transformed to the irradiance domain so as to permit direct experiment-theory comparisons. The spatial correlation measurements showed good agreement with theory, but an extreme sensitivity to instrumentation accuracy and dynamic range was noted. Judged by these measurements, it appears that the correlation distance for irradiance fluctuations can be accurately evaluated through Rytov theory. The spectral correlation measurements exhibited an unacceptably large scatter and did not show the wavelength dependence predicted by theory. A typical measured correlation for sources at 0.633μ and 0.488μ which had traversed the same path was 0.7. This indicates that spectral diversity techniques in the visible will not be an effective means of overcoming turbulence-induced signal fading. We note, however, that the same measurements indicate that the coherent bandwidth limitation which exists at radio frequencies is not a significant problem at optical frequencies. Therefore, atmospheric turbulence will not impose a limitation on the information bandwidth of an optical carrier from a coherency standpoint.

Analysis of the quality of a communication system (particularly a digital system) requires knowledge of the density function of the amplitude statistics. Data have been obtained, analyzed, and compared to three suggested model densities (log-normal, Rayleigh, and Rice). A mean-square error and a chi-square test have been applied as the criteria of comparison. Under weak fluctuations, the log-normal and Rice distributions were found to be equally well suited to the data; under strong fluctuations, the log-normal distribution was an order of magnitude closer to the data in both the mean-square-error and the chi-square tests.

ACKNOWLEDGMENT

The author wishes to express his gratitude to the management of Goddard Space Flight Center for their support, which has been very generous over a period of several years. In particular, we thank Henry Plotkin, Walter Carrion, and Peter Minott of the Optical Systems Branch for their assistance and encouragement. Jack Bufton has been a co-investigator in much of the experimental work, and his assistance in the computer analysis has been an essential ingredient.

Goddard Space Flight Center
National Aeronautics and Space Administration
Greenbelt, Maryland, August 18, 1970
125-22-08-04-51

REFERENCES

1. Chernov, L., Wave Propagation in a Random Medium McGraw-Hill, New York, 1960.

2. Tatarski, V., Wave Propagation in a Turbulent Medium McGraw-Hill, New York, 1961.

3. Chandrasekhar, S., "A Statistical Basis of the Theory of Stellar Scintillation," Roy. Astron. Soc. Monthly Notices 112: 475 (1952).

4. Ellison, M., The Effects of Scintillation on Telescopic Images Proc. of a Symposium on Astronomical Optics and Related Subjects, Z. Kopal, Ed., Interscience, New York, 1956.

5. Wimbush, W., Optical Astronomical Seeing: A Review Scientific Rept. No. 1, Honolulu, Hawaii, May 1961.

6. Meyer-Arendt, J., and Emmanuel, C. B., Optical Scintillation: A Survey of the Literature Tech. Note 225, Nat. Bur. Std., Boulder, Colorado, Apr. 5, 1965.

7. Born, M., and Wolf, E., Principles of Optics 2nd rev. ed., Pergamon Press, New York, 1964.

8. Silver, S. "Microwave Aperture Antennas and Diffraction Theory," J. Opt. Soc. Am. 52:131 (1962).

9. Wolf, E., and Marchanel, E. W., "Comparison of the Kirchoff and the Rayleigh-Sommerfeld Theories of Diffraction at an Aperture," J. Opt. Soc. Am. 54:587 (1964).

10. Goodman, J. W., Introduction to Fourier Optics McGraw-Hill, San Francisco, 1968.

11. Sommerfeld, A., Optics Lectures on Theoretical Physics Vol. 4, Academic Press Inc., New York, 1954.

12. Sommerfeld, A., "Mathematische Theorie der Diffraction," Math. Ann. 47:317 (1896).

13. Stratton, J. A., Electromagnetic Theory McGraw-Hill, New York, 1941.

14. Kerr, D. E., Propagation of Short Radio Waves McGraw-Hill, New York, 1951.

15. Rayleigh, Lord, Phil. Mag. 41:107, 274, 447 (1871).

16. Rayleigh, Lord, The Scientific Papers of Lord Rayleigh Vols. 1 and 4, Cambridge University Press, New York, 1912.

17. Mie, G., "Beiträge Zur Optik Trüber Medien, Speziell Kolloidaler Metallösurgen," Ann. Physik 25:377 (1908).

18. Van de Hulst, H., Light Scattering by Small Particles John Wiley and Sons, Inc., New York, 1964.

19. Carrier, L. W. Cato, G. A., and Von Essen, K. J., "The Backscatter and Extinction of Visible and Infrared Radiation by Selected Major Cloud Models," Appl. Opt. 6:1209 (1967).

20. Dunbin, W., "Droplet Sampling in Cumulus Clouds," Air Ministry Meteorol. Res. Comm. Publ. 991 (1956).

21. Green, H. L., and Lane, W. R., Particulate Clouds: Dusts, Smokes, and Mists D. Van Nostrand Company, Princeton, New Jersey, 1957.

22. Bauer, E., "The Scattering of Infrared Radiation from Clouds," Appl. Opt. 3:197 (1964).

23. Khrgran, A., Ed., Cloud Physics Available as Office of Technical Services Transl. OTS-63-11141, 1961.

24. Lumley, J. L., and Panofsky, H. A., The Structure of Atmospheric Turbulence Interscience, New York, 1964.

25. Lin, C. C., Statistical Theories of Turbulence Princeton University Press, Princeton, New Jersey, 1961.

26. Krechmer, S. I., "Investigations of Microfluctuations of the Temperature Field in the Atmosphere," Doklady Akad. Nauk SSSR 84:55 (1952).

27. Hufnagel, R. E., Optical Propagation Study Tech. Rep. No. RADC-TR-65-511, Jan. 1966.

28. Handbook of Geophysics U.S. Air Force, ARDC, GRD, MacMillan Company, New York, 1960.

29. Obukhov, A. M., "On the Distribution of Energy in the Spectrum of Turbulent Flow," Doklady Akad. Nauk SSSR 32:19 (1941).

30. Kolmogorov, A. N., "The Local Structure of Turbulence in Incompressible Viscous Fluid for Very Large Reynolds Numbers," Doklady Akad. Nauk SSSR 30:301 (1941). German translation in Sammelband zur Statistichen Theorie der Turbulenz Akademie-Verlag, Berlin, 1958, p. 71.

31. Obukhov, A. M., "Structure of the Temperature Field in a Turbulent Flow," Izvestia Akad. Nauk SSSR Ser. Geograf. Geofiz. 13:58 (1949). German translation in Sammelband zur Statistischen Theorie der Turbulenz Akademie-Verlag, Berlin, 1958, p. 127.

32. Yaglom, A. M., "On The Local Structure of the Temperature Field in a Turbulent Flow," Doklady Akad. Nauk SSSR 69:743 (1949). German translation in Sammelband zur Statistischen Theories der Turbulenz Akademie-Verlag, Berlin, 1948, p. 141.

33. Obukhov, A. M., "Investigations of the Microstructure of the Wind in the Atmosphere Near the Surface," Izvestia Akad. Nauk. SSSR Geofiz. Ser. 3 (1951).

34. Gurvich, A. S., "Frequency Spectra and Distribution Functions of Vertical Wind Components," Izvestia Akad. Nauk. SSSR Geofiz. Ser. 7 (1960).

35. MacCready, P. B. Jr., "Atmospheric Turbulence Measurement and Analysis," J. Meteorol. 10:325 (1953).

36. Pond, S., Stewart, R. W., and Burling, R. W., "Turbulence Spectra in Wind over Waves," J. Atmosph. Sci. 20 (1963).

37. Tatarski, V., Wave Propagation in a Turbulent Medium McGraw-Hill, New York, 1961, pp. 138-140.

38. Lutomirski, R. F., and Yura, H. T., "Modulation Transfer Function and Phase-Structure Function of an Optical Wave in a Turbulent Medium," J. Opt. Soc. Am. 59:999 (1969).

39. Tatarski, V., Wave Propagation in a Turbulent Medium McGraw-Hill, New York, 1961, p. 140.

40. Gebhardt, F. G., "The Log Amplitude Mean Value For Laser Beam Propagation in the Atmosphere, with Applications for Optical Communications," Ohio State University Electro-Science Lab. Tech. Rept. No. 21568, May 1968.

41. Taylor, L. S., "Twinkling Range of Turbulent Layers," J. Opt. Soc. Am. 59:113 (1969).

42. Beckmann, P., "Signal Degeneration in Laser Beams Propagated Through a Turbulent Atmosphere," Radio Sci. J. Res. 69D:4, Apr. 1965.

43. Tatarski, V., Wave Propagation in a Turbulent Medium McGraw-Hill, New York, 1961, p. 93.

44. Kear, D. E., Propagation of Short Radio Waves McGraw-Hill, New York, 1951, p. 53.

45. Strohbehm, J. W., "Line of Sight Propagation through Turbulent Atmosphere," Proc. IEEE 56:1301 (1968).

46. North American Rockwell, Autonetics Div., Final Report, "Optical Propagation Measurements at Emerson Lake - 1968," prepared for Langley Research Center (NASI-7705), 1968.

47. Taylor, L. S., "Validity of Ray-Optics Calculations in a Turbulent Atmosphere," J. Opt. Soc. Am. 58:57 (1968).

48. Taylor, L. S., "Validity of Ray-Optics in a Turbulent Atmosphere," J. Opt. Soc. Am. 58:57 (1968).

49. Strohbehm, J. W., "Comments on Rytov's Method," J. Opt. Soc. Am. 58:139 (1968).

50. Tatarski, V., Wave Propagation in a Turbulent Medium McGraw-Hill, New York, 1961, pp. 155-156.

51. Tatarski, V., Wave Propagation in a Turbulent Medium McGraw-Hill, New York, 1961, p. 139.

52. deWolf, D. A., "Wave Propagation Through Quasi-Optical Irregularities," J. Opt. Soc. Am. 55:812 (1965).

53. Proetheroe, W. M., "Preliminary Report on Stellar Scintillation," Contrib. Perkins Observ. Ser. 2 No. 447 (1955).

54. Pisareva, V. V., "Limits of Applicability of the Method of Smooth Perturbations in the Problem of Radiation Propagation Through a Medium Containing Inhomogeneritics," Soviet Phys. Acoustics 6:87 (1960).

55. Fienberg, Y. L., Propagation of Radiowaves Along the Earth's Surface Academy of Sciences, Moscow, 1961.

56. Tatarski, V. I., Izvestia Vuz Radiofiz. 5:490 (1962).

57. Hufnagel, R. E., and Stanley, N. R., "Modulation Transfer Function Associated with Image Transmission Through Turbulent Media," J. Opt. Soc. Am. 54:52 (1964).

58. Brown, W. P., "Validity of the Rytov Approximation in Optical Propagation Calculation," J. Opt. Soc. Am. 56:1045 (1966).

59. Fried, D. L., "Test of the Rytov Approximation," J. Opt. Soc. Am. 57:268 (1967).

60. Coulman, C. E., "Dependence of Image Quality on Horizontal Range in a Turbulent Atmosphere," J. Opt. Soc. Am. 56:1232 (1966).

61. deWolf, D. A., "Validity of Rytov's Approximation," J. Opt. Soc. Am. 57: 1057 (1967).

62. Heidbreder, G. R., "Multiple Scattering and the Method of Rytov," J. Opt. Soc. Am. 57:1477 (1967).

63. Keller, J. B., "Accuracy and Validity of the Born and Rytov Approximations," J. Opt. Soc. Am. 59: 1003 (1969).

64. Brown, W. P. Jr., "Validity of the Rytov Approximation," J. Opt. Soc. Am. 57: 1539 (1967).

65. deWolf, D. A., "Saturation of Irradiance Fluctuations Due to a Turbulent Atmosphere," J. Opt. Soc. Am. 58: 461 (1968).

66. deWolf, D. A., "Are Strong Irradiance Fluctuations Log Normal or Rayleigh Distributed? " J. Opt. Soc. Am. 59: 1455, 1513 (1969).

67. Fried, D. L., "Propagation of an Infinite Plane Wave in a Randomly Inhomogeneous Medium," J. Opt. Soc. Am. 56: 1669 (1966).

68. Fried, D. L., "Propagation of a Spherical Wave in a Turbulent Medium," J. Opt. Soc. Am. 57: 178, 179 (1967).

69. Kon, A. I., and Tatarski, V. I., "Parameter Fluctuations of a Space-Limited Light Beam in a Turbulent Atmosphere," Soviet Radiophys. 8: 617 (1965).

70. Fried, D. L., and Seidman, J. B., "Laser-Beam Scintillation in the Atmosphere," J. Opt. Soc. Am. 57:181 (1967).

71. Ho, T. L., "Log-Amplitude Fluctuations of Laser Beam in a Turbulent Atmosphere," J. Opt. Soc. Am. 4: 385 (1969).

72. Ishimaru, A., "Fluctuations of a Beam Wave Propagating Through a Locally Homogeneous Medium," Radio Sci. 4: 295 (1969).

73. Gebhardt, F. G., and Collins, S. A., "Log Amplitude Mean Value for Laser Beam Propagation in the Atmosphere," J. Opt. Soc. Am. 59:1139 (1969).

74. Schmeltzer, R. A., "Means, Variances, and Covariances for Laser Beam Propagation Through a Random Medium," Quart. Appl. Math. 24: 339 (1966).

75. Tatarski, V., Wave Propagation in a Turbulent Medium McGraw-Hill, New York, 1961, chapter 8.

76. Fried, D. L., "Propagation of an Infinite Plane Wave in a Randomly by Inhomogeneous Medium," J. Opt. Soc. Am. 56: 1670 (1966).

77. Fried, D. L., "Limiting Resolution Looking Down Through the Atmosphere," J. Opt. Soc. Am. 56: 1380 (1966).

78. Fried, D. L., "Scintillation of a Ground-to-Space Laser Illuminator," J. Opt. Soc. Am. 57: 980 (1967).

79. Kinoshita, Y., Asakura, T., and Suzuki, M., "Fluctuation Distribution of Gaussian Beam Propagating Through a Random Medium," J. Opt. Soc. Am. 58: 798 (1968).

80. Kinoshita, Y., Asakura, T., and Suzuki, M., "Autocorrelation of Gaussian-Beam Fluctuation Caused by a Random Medium," J. Opt. Soc. Am. 58: 1040 (1968).

81. Asakura, T., Kinoshita Y., and Suzuki, M., "Further Correlation Studies of Gaussian-Beam Fluctuations Caused by a Random Medium," J. Opt. Soc. Am. 59:913 (1969).

82. Fitzmaurice, M. W., Bufton, J. B., and Minott, P.O., "Wavelength Dependence of Laser-Beam Scintillation," J. Opt. Soc. Am. 59: 7 (1969).

83. Aitchison, J., and Brown, J. A. C., The Lognormal Distribution Cambridge University Press, Cambridge, 1963.

84. Gracheva, M. E., and Gurvich, A. S., "Strong Fluctuations in the Intensity of Light Propagated Through the Atmosphere Close to the Earth," Radiofizika 8: 511 (1965).

85. Bendat, J. S., and Piersol, A. G., Measurement and Analysis of Random Data John Wiley and Sons, Inc., New York, 1966.

86. Fried, D. L., "Aperture Averaging of Scintillation," J. Opt. Soc. Am. 57: 169 (1967).

87. Gracheva, M. E., Radiofizika 10: 775 (1967).

88. Fitzmaurice, M. W., and Bufton, J. L., "Measurement of Log Amplitude Variance," J. Opt. Soc. Am. 59: 462 (1969).

89. Dietz, P. H., and Wright, N. J., "Saturation of Scintillation Magnitude in Near-Earth Optical Propagation," J. Opt. Soc. Am. 59: 527 (1969).

90. Hufnagel, R. E., comment on "Measurement of Log Amplitude Variance," J. Opt. Soc. Am. 59: 462 (1969).

91. Ochs, G. R., and Lawrence, R. S., "Saturation of Laser-Beam Scintillation under Conditions of Strong Atmospheric Turbulence," J. Opt. Soc. Am. 59: 226 (1969).

92. Dietz, P. H., "Atmospheric Effects on the Beam Propagation of XM-23 Laser Range Finder," BRL Report No. 1871, Sept. 1967.

93. Dietz, P. H., and Wright, N. J., "Saturation of Scintillation Magnitude in Near-Earth Optical Propagation," BRL Report No. 1941, Oct. 1968.

94. Patton, R. B., Jr., and Reedy, M., "Effects of Atmospheric Turbulence on Ground-to-Air Laser Beam Propagation," BRL Report No. 1427, Mar. 1969.

95. Tatarski, V., Wave Propagation in a Turbulent Medium McGraw-Hill, New York, 1961, eq. 7-92 and fig. 7-12.

96. Fried, D. L., "Propagation of a Spherical Wave in a Turbulent Medium," J. Opt. Soc. Am. 57: 177 (1967).

97. Wessely, H. W., "Optical Scintillation Over Horizontal Path," E. H. Pleasset Assoc. Report, Aug. 1968.

98. Ochs, G. R., Bergman, R. R., and Snyder, J. R., "Laser Beam Scintillation over Horizontal Paths from 5.5 to 145 Kilometers," J. Opt. Soc. Am. 59: 231 (1969).

99. North American Rockwell, Autonetics Div., Final Report, "Optical Propagation Measurements at Emerson Lake—1968," prepared for Langley Research Center (NASI-7705S), 1968, p. 112.

100. North American Aviation, Inc., "Optical Effects of Atmospheric Turbulence," Autonetics Division Report No. C7-805/401, Mar. 1967, p. 33.

101. Riley, G. F., and Kuppenheimer, J. D., "Experimental Determination of Probability Distribution for Irradiance Fluctuations of Laser Beam in Turbulent Atmosphere by Photon Counting," Spring Meeting, Opt. Soc. of Am., Apr. 1970.

102. Horning, R. R., "Deviation of Atmospheric Scintillation from the Log-Normal Distribution," Spring Meeting, Opt. Soc. of Am., Apr. 1970.

103. Mitchell, R. L., "Permanence of the Log-Normal Distribution," J. Opt. Soc. Am. 58: 1267 (1968).

104. Mood, A. M., and Graybill, F. A., Introduction to the Theory of Statistics McGraw-Hill, New York, 1963.

105. Papoulis, A., Probability, Random Variables, and Stochastic Processes McGraw-Hill, New York, 1965, p. 498.

106. Williams, C. A. Jr., "On the Choice of the Number and Width of Classes for the Chi-Square Test of Goodness of Fit," Am. Stat. Ass. J. 45:77 (1950).

Appendix A

Determination of the Number of Independent Samples for Processes With Arbitrary Spectral Densities

In this section we consider the problem of finding the number of independent samples N that one obtains in a continuous data run of length T taken from a random process $x(t)$.

First consider the case where x has a one-sided spectral density $G_x(f)$ which is flat-baseband, i.e.,

$$G_x(f) = \frac{K}{B}, \quad \text{for } 0 \leq f \leq B \quad ,$$

and

$$G_x(f) = 0, \text{ for } f > B \quad ; \tag{A1}$$

then, the autocorrelation of x, $R_x(\tau)$ is

$$R_x(\tau) = \int_0^\infty G_x(f) \cos 2\pi f_\tau \, df = K \frac{\sin 2\pi B\tau}{2\pi B\tau} \cdot \tag{A2}$$

So,

$$R_x(0) = E[x^2] = K \tag{A3}$$

and the first zero of $R_x(\tau)$ occurs at $\tau = 1/2B$. Therefore, samples taken at times 1/2B apart are uncorrelated and (for normal processes) independent. In a data run of length T, it is now clear that one can obtain at most $T/1/2B = 2BT$

independent samples. Note also that

$$\frac{1}{T}\int_{-\infty}^{\infty} R_x(\tau)\,d\tau = \frac{1}{T}\int_{-\infty}^{\infty} K\,\frac{\sin 2\pi B\tau}{2\pi B\tau}\,d\tau = \frac{K}{2BT} = \frac{K}{N}. \tag{A4}$$

Now consider the case where $G_x(f)$ is not flat-baseband but, rather, has an arbitrary shape. Then one can evaluate $R_x(\tau)$ through the usual Fourier Transform relation. Then

$$\frac{1}{T}\int_{-\infty}^{\infty} R_x(\tau)\,d\tau = \frac{R_x(0)}{2B_{eq.}T}, \tag{A5}$$

where $B_{eq.}$ is the equivalent rectangular bandwidth of the process. Therefore,

$$B_{eq.} = \frac{R_x(0)}{2\int_{-\infty}^{\infty} R_x(\tau)\,d\tau} = \frac{1}{2\int_{-\infty}^{\infty} \gamma(\tau)\,d\tau}, \tag{A6}$$

where $\gamma(\tau)$ is the normalized correlation coefficient defined for stationary process as

$$\gamma(\tau) = \frac{E\left[x(t)\,x(t+\tau)\right]}{VAR(x)}. \tag{A7}$$

So in this case the number of independent samples N obtained in a record of length T is

$$N = T\Big/\int_{-\infty}^{\infty} \gamma(\tau)\,d\tau. \tag{A8}$$

In practice, two approximate techniques permit a quick evaluation of the above integral. Many physical processes have autocorrelation functions which can be closely approximated by the exponential fit $e^{-\alpha|\tau|}$. In this case

$$N = \frac{\alpha T}{2} . \tag{A9}$$

Alternately one may approximate $\gamma(\tau)$ by a linear fit, i.e.,

$$\begin{aligned} \gamma(\tau) &= 1 - \alpha|\tau| \qquad 0 \leq |\tau| \leq \frac{1}{\alpha} \\ &= 0 , \end{aligned} \tag{A10}$$

elsewhere. In this case,

$$N = \alpha T . \tag{A11}$$

Appendix B

Range and Wavelength Dependence of Log-Amplitude Variance for Arbitrary Turbulent Spectra

Consider a refractive index structure function of the form

$$D_n(x) = \alpha^2 x^p , \tag{B1}$$

where α^2 is an arbitrary constant and p is also a constant in the range $0 < p < 2$. Using Tatarski's[2] results, the one-dimensional spatial spectrum corresponding to Eq. B1 is

$$w(\kappa) = \frac{\Gamma(1+p)}{2\pi} \sin\frac{\pi p}{2} \alpha^2 c^{-(p+1)} \kappa^{-(p+1)} . \tag{B2}$$

For isotropic random fields, the three-dimensional spectrum $\left[\phi(\kappa)\right]$ is related to the one-dimensional spectrum $\left[w(\kappa)\right]$ through

$$\phi(\kappa) = -\frac{1}{2\pi\kappa} \frac{dw(\kappa)}{d\kappa} . \tag{B3}$$

Therefore,

$$\phi(\kappa) = A \kappa^{-(p+3)} , \tag{B4}$$

where

$$A = \frac{\Gamma(1+p)}{(2\pi)^2} \sin\frac{\pi p}{2} \alpha^2 c^{-(p+1)} (p+1) .$$

For the case where the field quantities are homogeneous and isotropic in planes perpendicular to the direction of propagation, the covariance of log amplitude can be written as

$$C_\ell(r) = 2\pi \int_0^\infty J_o(\kappa r) F(\kappa, 0) \kappa \, d\kappa, \tag{B5}$$

where $F(\kappa, 0)$ is the two-dimensional spatial spectrum in the measurement plane. For infinite plane-wave propagation through homogeneous turbulence, Tatarski[2] has shown in his Eq. 7.50 that

$$F(\kappa, 0) = \pi k^2 L \left(1 - \frac{k}{\kappa^2 L} \sin \frac{\kappa^2 L}{k}\right) \phi(\kappa), \tag{B6}$$

where

k is the wave number of the optical carrier,

and

L is the path length through the turbulence.

Substitute Eqs. B4 and B6 into Eq. B5; the log-amplitude covariance becomes

$$C_\ell(r) = 2\pi^2 A k^2 L \int_0^\infty J_o(\kappa r) \left(1 - \frac{k}{\kappa^2 L} \sin \frac{\kappa^2 L}{k}\right) \kappa^{-(p+2)} \, d\kappa, \tag{B7}$$

and the variance is

$$C_\ell(0) = 2\pi^2 A k^2 L \int_0^\infty \left(1 - \frac{k}{\kappa^2 L} \sin \frac{\kappa^2 L}{k}\right) \kappa^{-(p+2)} \, d\kappa \, . \tag{B8}$$

Let

$$\xi = \frac{\kappa^2 L}{k}$$

and

$$d\xi = \frac{2L}{k} \kappa \, d\kappa ,$$

and substitute into Eq. B8. Then

$$C_\ell(0) = 2\pi^2 A k^2 L \int_0^\infty \left(1 - \frac{\sin\xi}{\xi}\right)\left(\frac{k}{2L}\right)\left(\frac{k\xi}{L}\right)^{-(p+3)/2} d\xi$$

$$= \pi^2 A k^{3/2-p/2} L^{3/2+p/2} \int_0^\infty \left(1 - \frac{\sin\xi}{\xi}\right)\xi^{-(p+3)/2} d\xi \quad . \tag{B9}$$

So, for infinite plane-wave propogation, the log-amplitude variance exhibits a $k^{3/2-p/2}$ wave-number dependence and a $L^{3/2+p/2}$ range dependence. For spherical-wave propagation through homogeneous turbulence, the log-amplitude variance equation takes the form

$$C_\ell(0) = 2\pi^2 k^2 L \int_0^\infty \left\{1 - \sqrt{\frac{2\pi k}{\kappa^2 L}}\left[\cos\frac{\kappa^2 L}{4k} C\left(\sqrt{\frac{\kappa^2 L}{2\pi k}}\right) + \sin\frac{\kappa^2 L}{4k} S\left(\sqrt{\frac{\kappa^2 L}{2\pi k}}\right)\right]\right\}\phi(\kappa)\,\kappa\,d\kappa, \tag{B10}$$

where C(x) and S(x) are the Fresnel integrals

$$C(x) = \int_0^x \cos \frac{\pi t^2}{2} \, dt$$

and

$$S(x) = \int_0^x \sin \frac{\pi t^2}{2} \, dt \ .$$

Let

$$\xi = \frac{\kappa^2 L}{2\pi k} \ ,$$

and substitute Eq. B4 into Eq. B10. Then

$$C_\ell(0) \approx k^{(3/2-p/2)} L^{(3/2+p/2)} \int_0^\infty \left\{ 1 - \sqrt{\frac{1}{\xi}} \left[\cos \sqrt{\frac{\pi\xi}{2}} \, C\left(\sqrt{\xi}\right) + \sin \sqrt{\frac{\pi\xi}{2}} \, S\left(\sqrt{\xi}\right) \right] \right\} \xi^{-(p+3)/2} \, d\xi \ . \quad \text{(B11)}$$

So, again, the log-amplitude variance has a wave-number dependence $k^{3/2-p/2}$ and a range dependence $L^{3/2+p/2}$.

Appendix C

Dynamic Range Considerations in the Measurement of Log-Amplitude Variance

One of the major problems confronting the experimenter as he investigates amplitude fluctuations at optical frequencies is the dynamic range of the instrumentation. The amplitude fluctuations are characterized by short periods of very high level (compared to the mean) and somewhat longer periods of low signal level (compared to the mean). Accurate recording and meaningful statistical analysis of this type of phenomena require extended instrumental dynamic range. The problem has recently been looked at analytically for the first time in Ref. 46 In this analysis, it was assumed that the log-amplitude variance σ_ℓ^2 was evaluated through irradiance statistics by means of

$$\sigma_\ell^2 = \frac{1}{4} ln \left(\frac{\sigma_I^2}{I_0^2} \right), \tag{C1}$$

where

$$I_0 = E(I)$$

and

$$\sigma_I^2 = E\left([I - I_0]^2 \right).$$

It was also assumed that the available dynamic range was evenly divided about I_0. That is, if I_H and I_L are the highest and lowest signals that can be handled by the

instrument, then the fluctuating signal is sealed so that

$$\frac{I_H}{I_0} = \frac{I_0}{I_L} .$$

A numerical integration of the right-hand side of Eq. C1 was carried out for various σ_ℓ^2 and dynamic range values. The results are presented in a graph of measured log-amplitude variance $\left(\sigma_{\ell_{meas.}}^2\right)$ versus actual log-amplitude variance $\left(\sigma_\ell^2\right)$ for various dynamic ranges. A typical result is that an

$$\frac{I_H}{I_0} \geq 18$$

is required to measure a relatively weak $\sigma_\ell^2 = 0.2$. This range (18^2) is approximately the state-of-the-art in FM magnetic tape recording.

It appears that that these results may be unduly discouraging. If one is actually measuring σ_ℓ^2 through Eq. 1, then $E(I)$ and $E\left(I^2\right)$ are the only statistics of interest and the available dynamic range would not be alloted equally about I_0; rather, it would be biased so as to accommodate peak signals. In addition, the numerical integration which produced the results did not clip signals which exceeded the allowed range but, rather, set these signals equal to zero. The amount of error introduced by this technique could be substantial. In this appendix, a different analysis is presented which may be more accurate in some cases.

It is assumed that the log-amplitude variance is measured not through Eq. C1 but, rather, by evaluation of the probability density function for the variable log

amplitude (ℓ_i), where

$$\ell_i = \frac{1}{2} \ln \frac{I_i}{I_0} \qquad i = 1, 2, \cdots n \tag{C2}$$

and

$$n = \text{sample size},$$

and by computing moments $E[\ell_i]$, $E\left[(\ell_i - \overline{\ell}_i)^2\right]$ in the usual manner. In this case it is efficient to allot the dynamic range as above, i.e.,

$$\frac{I_H}{I_0} = \frac{I_0}{I_L} \equiv R .$$

Our model for the system is

$$\begin{aligned} \ell_{i_{out}} &= \ell_{i_{in}} \text{ , for } |\ell_{i_{in}}| \leq R , \\ \ell_{i_{out}} &= \frac{1}{2} \ln R \equiv B, \text{ for } \ell_{i_{in}} > R , \\ \text{and} \\ \ell_{i_{out}} &= -\frac{1}{2} \ln R = -B, \text{ for } \ell_{i_{in}} < R . \end{aligned} \tag{C3}$$

The system is shown in terms of irradiance levels in Fig. C1. We assume log amplitude to be normal with mean μ_ℓ and variance σ_ℓ^2. That is, ℓ_i is $n(\mu_\ell, \sigma_\ell^2)$. So, the measured mean-square value of ℓ is

$$E[\ell^2]_{meas.} = \int_{-B}^{B} \ell^2 \, n(\mu_\ell, \sigma_\ell^2) \, d\ell + \int_{-\infty}^{-B} B^2 \, n(\mu_\ell, \sigma_\ell^2) \, d\ell + \int_{B}^{\infty} B^2 \, n(\mu_\ell, \sigma_\ell^2) \, d\ell . \tag{C4}$$

Let

$$y = \ell - \mu_\ell .$$

Then, y is $n(0, \sigma_\ell^2)$, and

$$E[\ell^2]_{meas.} = \int_{-B-\mu_\ell}^{B-\mu_\ell} (y + \mu_\ell)^2 \, n(0, \sigma_\ell^2) \, dy$$

$$+ B^2 \int_{-\infty}^{-B-\mu_\ell} n(0, \sigma_\ell^2) \, dy + B^2 \int_{B-\mu_\ell}^{\infty} n(0, \sigma_\ell^2) \, dy \quad . \tag{C5}$$

Consider the second and third integrals. If we assume $B > |\mu_\ell|$, then we can change the limits with small error so that

$$B^2 \left\{ \int_{-\infty}^{B-\mu_\ell} n(0, \sigma_\ell^2) \, dy + \int_{B-\mu_\ell}^{\infty} n(0, \sigma_\ell^2) \, dy \right\}$$

$$= B^2 \left\{ \int_{-\infty}^{-B} n(0, \sigma_\ell^2) \, dy + \int_{B}^{\infty} n(0, \sigma_\ell^2) \, dy \right\}$$

$$= B^2 \left[1 - 2 \, erf \left(\frac{B}{\sigma_\ell} \right) \right], \tag{C6}$$

where

$$erf(x) \equiv \frac{1}{\sqrt{2\pi}} \int_0^x e^{-t^2/2} \, dt \quad .$$

The first integral in Eq. C5 can be expanded and evaluated by parts.

$$\int_{-B-\mu_\ell}^{B-\mu_\ell} (y + \mu_\ell)^2 \, n(0, \sigma_\ell^2) \, dy = \int_{-B-\mu_\ell}^{B-\mu_\ell} (y^2 + 2\mu_\ell y + \mu_\ell^2) \, n(0, \sigma_\ell^2) \, dy \quad . \tag{C7}$$

The first part is

$$\int_{-B-\mu_\ell}^{B-\mu_\ell} \mu_\ell^2 \, n\left(0, \sigma_\ell^2\right) dy \;=\; \mu_\ell^2 \left\{ P\left(\frac{B-\mu_\ell}{\sigma_\ell}\right) - P\left(\frac{-B-\mu_\ell}{\sigma_\ell}\right) \right\}, \tag{C8}$$

where

$$P(x) \;=\; \frac{1}{\sqrt{2\pi}} \int_{-\infty}^{x} e^{-t^2/2} \, dt \;.$$

The second part is

$$\int_{-B-\mu_\ell}^{B-\mu_\ell} 2\mu_\ell \, y \, n\left(0, \sigma_\ell^2\right) dy \;=\; 2\mu_\ell \left\{ \int_{-B-\mu_\ell}^{B+\mu_\ell} y \, n\left(0, \sigma_\ell^2\right) dy \right\}$$

$$+ \int_{B+\mu_\ell}^{B-\mu_\ell} y \, n\left(0, \sigma_\ell^2\right) dy \;. \tag{C9}$$

The first integrand is odd and therefore vanishes. Therefore,

$$\int_{-B-\mu_\ell}^{B-\mu_\ell} 2\mu_\ell \, y \, n\left(0, \sigma_\ell^2\right) dy \;=\; 2\mu_\ell \int_{B-\mu_\ell}^{B-\mu_\ell} y \, n\left(0, \sigma_\ell^2\right) dy \;\doteq\; -4\mu_\ell^2 \, B \, Z\left(\frac{B}{\sigma_\ell}\right), \tag{C10}$$

where $n\left(0, \sigma_\ell^2\right)$ in the interval $\left(B+\mu_\ell \text{ to } B-\mu_\ell\right)$ has been approximated by its value at the midpoint B, and

$$Z(x) \;\equiv\; \frac{1}{\sqrt{2\pi}} \exp\left[-\frac{x^2}{2}\right] \;.$$

The third part is

$$\int_{-B-\mu_\ell}^{B-\mu_\ell} y^2\, n\left(0,\ \sigma_\ell^2\right)\, dy \ \doteq\ \int_{-B}^{B} y^2\, n\left(0,\ \sigma_\ell^2\right)\, dy \ =\ 2\int_{0}^{B} y^2\, n\left(0,\ \sigma_\ell^2\right)\, dy\,. \qquad \text{(C11)}$$

Let

$$\xi \ =\ \frac{y^2}{2\sigma_\ell^2}\,.$$

Then,

$$\int_{-B-\mu_\ell}^{B-\mu_\ell} y^2\, n\left(0,\ \sigma_\ell^2\right)\, dy \ =\ \frac{2\sigma_\ell^2}{\sqrt{\pi}} \int_{0}^{B^2/2\sigma_\ell^2} \xi^{1/2}\, e^{-\xi}\, d\xi$$

$$=\ \frac{2\sigma_\ell^2}{\sqrt{\pi}}\, \Gamma\left(\frac{3}{2}\right)\, I\left(\frac{B^2}{\sqrt{6}\,\sigma_\ell^2}\ ,\ \frac{1}{2}\right), \qquad \text{(C12)}$$

where $\Gamma(x)$ is the complete Gamma Function

$$\Gamma(x) \ =\ \int_{0}^{\infty} t^{x-1}\, e^{-t}\, dt$$

and $I(u,\ p)$ is the incomplete Gamma Function Ratio

$$I(u,\ p) \ =\ \frac{1}{\Gamma(p+1)} \int_{0}^{u\sqrt{p+1}} t^{p}\, e^{-t}\, dt\ .$$

Simplifying and combining terms, we have

$$E\left[\ell^2\right]_{meas.} = \sigma_\ell^2 \, I\left(\frac{B^2}{\sqrt{6}\,\sigma_\ell^2}, \frac{1}{2}\right) - 4\mu_\ell^2 \, B \, Z\left(\frac{B}{\sigma}\right) + \mu_\ell^2 \left\{p\left(\frac{B-\mu_\ell}{\sigma_\ell}\right) - p\left(\frac{-B-\mu_\ell}{\sigma_\ell}\right)\right\}$$

$$+ B^2\left[1 - 2\,\mathrm{erf}\left(\frac{B}{\sigma_\ell}\right)\right] . \qquad \text{(C13)}$$

Realizing that the dynamic range constraint is much less severe for measuring $E\{\ell\}$, we assume $E[\ell]_{meas.} = \mu_\ell$; then

$$\sigma_{\ell}^2{}_{meas.} = \sigma_\ell^2 \, I\left(\frac{B^2}{\sqrt{6}\,\sigma_\ell^2}, \frac{1}{2}\right) - 4\mu_\ell^2 \, B \, Z\left(\frac{B}{\sigma}\right) + \mu_\ell^2 \left\{p\left(\frac{B-\mu_\ell}{\sigma_\ell}\right) - p\left(\frac{-B-\mu_\ell}{\sigma_\ell}\right) - 1\right\}$$

$$+ B^2\left[1 - 2\,\mathrm{erf}\left(\frac{B}{\sigma_\ell}\right)\right] . \qquad \text{(C14)}$$

The result is now in a form such that various strengths of turbulence (σ_ℓ^2) and dynamic ranges (B) can be put in and the measured strength of turbulence $\left(\sigma_{\ell}^2{}_{meas.}\right)$ evaluated from tables. The calculation of the right-hand side of Eq. C14 requires that one recognize that $\mu_\ell = -\sigma_\ell^2$, which has been shown in Eq. 103 of Section 2.4.

As an example, consider a data analysis system which has a signal-to-noise ratio of 43 db. As an analog system, it has a definite upper limit (I_H) but its lower limit is not defined. However, the noise level of the system may be defined as the smallest signal level which can be accurately analyzed. Thus,

$$43 = 20 \log \frac{I_H}{I_L} = 20 \log \frac{I_H}{I_0}\,\frac{I_0}{I_L} = 40 \log R \, .$$

So,

$$R = 11.9,$$

and

$$B = \frac{1}{2} \ell n \frac{I_H}{I_0} = \frac{1}{2} \ell n R = 1.24 .$$

Eq. C14 can now be evaluated for various σ_ℓ^2 values. The results of this calculation are shown in Fig. C2, where the points represent the actual calculations.

Some caution must be used when evaluating Eq. C14 for small B/σ_ℓ values, since the approximations used in the derivation may lose accuracy. For $B/\sigma_\ell > 2$, the first term in Eq. C14 dominates. Specifically, if

$$\frac{B}{\sigma_\ell} = 2, \text{ then, } \frac{\sigma_{\ell_{meas.}}^2}{\sigma_\ell^2} \doteq .75 ;$$

if

$$\frac{B}{\sigma_\ell} = 2.5, \text{ then, } \frac{\sigma_{\ell_{meas.}}^2}{\sigma_\ell^2} \doteq .95 .$$

Defining the dynamic range (DR) of a device as its signal-to-noise ratio,*

$$DR = 20 \log \left(\frac{I_H}{I_0}\right)\left(\frac{I_0}{I_L}\right) = 20 \log R^2 = 40 \log R,$$
$$B = \frac{1}{2} \ell n R. \qquad \text{(C15)}$$

*With this definition, our dynamic range is numerically twice that used in Ref. 46 with units in dB.

Therefore,

$$DR = 40 \log e^{2B} = 80\, B \log e$$

$$= 34.7\ B\ . \qquad \text{(C15)}$$

Considering two levels of desired accuracy (5%, 25%) in the measurement system, then

$$DR = 86.7\, \sigma_{\ell} \quad (5\%\ \text{Accuracy}) \qquad \text{I}$$

and (C16)

$$DR = 69.4\, \sigma_{\ell} \quad (25\%\ \text{Accuracy}). \qquad \text{II}$$

Fig. C3 plots I and II.

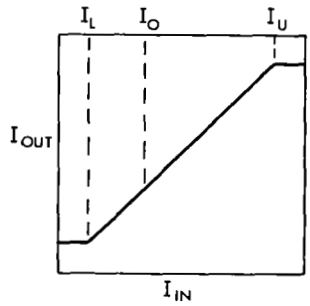

Figure C1

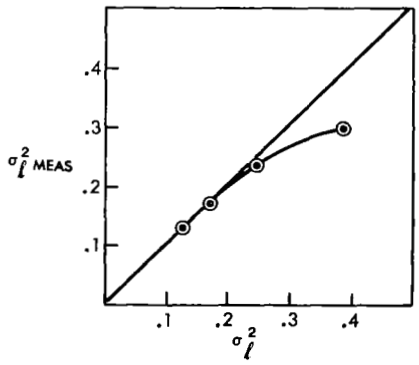

Figure C2

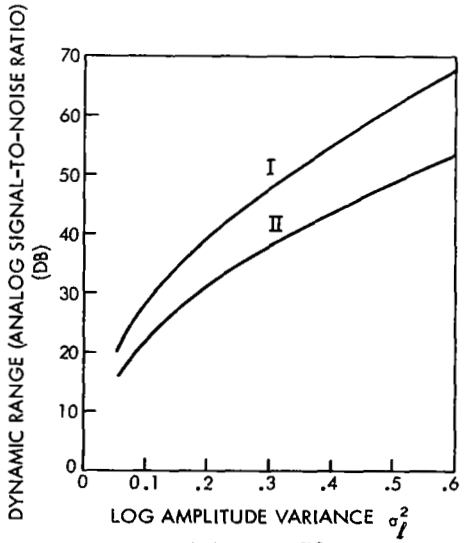

Figure C3

NASA-Langley, 1971 —— 23